

1 **The Arctic Subpolar gyre sTate Estimate (ASTE):**
2 **Description and assessment of a data-constrained,**
3 **dynamically consistent ocean-sea ice estimate**
4 **for 2002–2017**

5 **An T. Nguyen^{1*}, Helen Pillar¹, Victor Ocaña¹, Arash Bigdeli¹, Timothy A.**
6 **Smith¹, Patrick Heimbach^{1,2,3}**

7 ¹Oden Institute for Computational Engineering and Sciences, University of Texas at Austin

8 ²Jackson School of Geosciences, University of Texas at Austin

9 ³Institute for Geophysics, University of Texas at Austin

10 **Key Points:**

- 11 • The 2002–2017 medium-resolution Arctic Subpolar gyre sTate Estimate (ASTE)
12 is constrained to 10⁹ satellite and in situ observations.
- 13 • Strict adherence to conservation laws ensures all sources/sinks can be accounted
14 for, enabling application for meaningful budget analyses.
- 15 • ASTE captures the large-scale dynamics of the Arctic ocean-sea ice system includ-
16 ing variability and trends in heat and freshwater storage.

*Oden Institute for Computational Engineering and Sciences
The University of Texas at Austin
201 East 24th St., POB 4.234, C0200, Austin, TX, 78712, USA

Corresponding author: An T. Nguyen, atnguyen@oden.utexas.edu

Abstract

A description and assessment of the first release of the Arctic Subpolar gyre state Estimate (*ASTER1*), a medium-resolution data-constrained ocean-sea ice model-data synthesis spanning the period 2002–2017 is presented. The fit of the model to an extensive ($O(10^9)$) set of satellite and in situ observations was achieved through adjoint-based nonlinear least-squares optimization. The improvement of the solution compared to an unconstrained simulation is reflected in misfit reductions of 77% for Argo, 50% for satellite sea surface height, 58% for the Fram Strait mooring, 65% for Ice Tethered Profilers, and 83% for sea ice extent. Exact dynamical and kinematic consistency is a key advantage of *ASTER1*, distinguishing the state estimate from existing ocean reanalyses. Through strict adherence to conservation laws, all sources and sinks within *ASTER1* can be accounted for, permitting meaningful analysis of closed budgets, such as contributions of horizontal and vertical convergence to the tendencies of heat and salt. *ASTER1* thus serves as the biggest effort undertaken to date of producing a specialized Arctic ocean-ice estimate over the 21st century. Transports of volume, heat, and freshwater are consistent with published observation-based estimates across important Arctic Mediterranean gateways. Interannual variability and low frequency trends of freshwater and heat content are well represented in the Barents Sea, western Arctic halocline, and east subpolar North Atlantic. Systematic biases remain in *ASTER1*, including a warm bias in the Atlantic Water layer in the Arctic and deficient freshwater inputs from rivers and Greenland discharge.

Plain Language Summary

A 2002–2017 ocean-sea ice product, *ASTER1*, is distributed for use in decadal climate studies in the northern high latitudes. The product is a model-data synthesis, merging approximately a billion satellite and in situ observations with a numerical model. The primary strength of *ASTER1* compared to most existing ocean reanalyses is that strict adherence to the equations describing the fluid flow and conservation laws is built into the product, thus making *ASTER1* free from artificial un-physical sources or sinks and associated “jumps” in the time-evolving state. Furthermore, the product is consistent with most available observations, both used in the synthesis and retained for independent verification. This indicates good large-scale representation of evolving sea-ice, ocean currents and water properties, including year-to-year variability and decadal trends in heat and freshwater storage in the Arctic and subpolar North Atlantic. Some systematic data-model differences remain in the product and highlight where extra data and/or model development will improve the next release. The product and underlying model configuration are freely available to the research community.

1 Introduction

The Arctic region has experienced large changes in recent decades. These include near-surface air temperature warming at twice the global rate (Richter-Menge & Jeffries, 2011), rapid decline in multi-year sea ice (Kwok & Cunningham, 2015), enhanced solar radiation absorption in the Western Arctic upper ocean (Timmermans et al., 2018), increased river and glacial discharge (Bamber et al., 2012, 2018; Proshutinsky et al., 2020), and increased influxes of freshwater from the Pacific (Woodgate, 2018) and heat from the Atlantic (Polyakov et al., 2011). Many of these changes have been suggested to trigger positive feedbacks. Enhanced shortwave absorption (Jackson et al., 2010; Perovich et al., 2011; Timmermans et al., 2018), enhanced air-ice-sea momentum transfer (Rainville & Woodgate, 2009; Martin et al., 2014), shoaling of the Atlantic Water layer (Polyakov et al., 2017, 2020), and enhanced heat flux through the Fram Strait (Q. Wang et al., 2020) have all been identified to both result from and further amplify sea-ice thinning.

66 Some of the recent changes in the observed Arctic Ocean heat content have been
 67 traced back upstream into the North Atlantic (e.g., Årthun & Eldevik, 2016), and linked
 68 to pulsed warming of the Atlantic Water (AW) inflow (Mulwijk et al., 2018). Tracking
 69 these pulses provides a useful estimate of characteristic circulation and residence timescales
 70 within Arctic Ocean’s boundary currents. For example, it is estimated to take $O(1-3 \text{ yr})$
 71 for these heat pulses to be carried by the Norwegian Atlantic Current from the Green-
 72 land Scotland Ridge (GSR) to the Fram Strait (Årthun & Eldevik, 2016). After pass-
 73 ing through the Fram Strait, it is estimated that these pulses remain in the Arctic for
 74 $O(15-25\text{yr})$ exiting via the Fram Strait after following either a complete circumpolar path-
 75 way or a shorter circumnavigation of the Eurasian Basin (Karcher et al., 2011; Polyakov
 76 et al., 2011; Timmermans & Marshall, 2020).

77 Similar characteristic timescales emerge from considering the large-scale redistribu-
 78 tion of freshwater in the Arctic. For example, theoretical arguments suggest multi-
 79 decadal timescales for eddy-driven equilibration between the Beaufort Gyre’s circulation
 80 and freshwater content (Manucharyan et al., 2016). Similar timescales also emerge from
 81 considering geometrical constraints on the dynamics of inter-basin exchange to infer resi-
 82 dence times within the Arctic (Haine et al., 2015).

83 It is clear that investigations of mechanisms setting the time-mean and evolving
 84 state of the Arctic and exchanges with surrounding oceans must be supported by basin-
 85 scale estimates of the ocean-sea ice state. Historically, these observations have been ex-
 86 tremely sparse, and in the absence of observational constraints, realistic simulation of
 87 the Arctic and sub-Arctic ocean-sea ice state has remained challenging. There has been
 88 a notable increase, however, in observational coverage since the 2000s. Increasing avail-
 89 ability of *in situ* observations of sub-surface ocean hydrography and oceanic transports
 90 across Arctic gateways continues to improve our understanding of key processes, includ-
 91 ing interior eddy activity and mixing (Timmermans et al., 2012; Cole et al., 2014; Zhao
 92 et al., 2016; Bebieva & Timmermans, 2016), and the transformation and redistribution
 93 of watermasses (Proshutinsky et al., 2009; Rabe et al., 2014; Pnyushkov et al., 2015; Tim-
 94 mermans & Jayne, 2016; von Appen, Schauer, Hattermann, & Beszczynska-Möller, 2015;
 95 Polyakov et al., 2017; Timmermans et al., 2018). In the upper ocean, satellite altime-
 96 try (Kwok & Morison, 2016), gravimetry (Peralta-Ferriz et al., 2014), and sea ice obser-
 97 vations have allowed a more accurate estimate of Ekman transport (Meneghello et al.,
 98 2018) and inventory of freshwater in the Western Arctic (Proshutinsky et al., 2019, 2020).

99 In parallel with increased observational coverage, great progress has also been made
 100 using theoretical and modeling frameworks to advance our understanding of Arctic Ocean
 101 dynamics, for example, elucidating the importance of eddies in gyre equilibration (as noted
 102 above, Manucharyan & Isachsen, 2019; Meneghello et al., 2017) and vertical heat redis-
 103 tribution (Polyakov et al., 2017). Despite this progress, confident assessment of the lo-
 104 cal time-mean state, interannual variability and identification of robust decadal trends
 105 remains a great challenge (Timmermans & Marshall, 2020) due to multiple factors (Holloway
 106 et al., 2007; Q. Wang et al., 2016b, 2016a; Ilicak et al., 2016; Docquier et al., 2019). The
 107 most important amongst these factors is the lack of direct observations throughout the
 108 full water column, including at the air-ice-ocean interface, in and just below the mixed
 109 layer, along the Atlantic Water (AW) boundary current pathway, and at the shelf-basin
 110 regions that connect the dynamics of this energetic current and the relatively quiescent
 111 Arctic Ocean interior (Timmermans & Marshall, 2020).

112 To fill in these gaps, the community has constructed climatologies (e.g., WOA13
 113 version 2 and WOA18, Locarnini et al., 2018; Zweng et al., 2018) and data-model syn-
 114 theses (Stammer et al., 2016; Uotila et al., 2019; Carton et al., 2019) which are assumed
 115 to have higher fidelity as the repository of incorporated data grows. The improved fit
 116 between the latest climatology and existing observations is far superior to that seen in
 117 older climatologies. For example, in the Western Arctic interior, Ice Tethered Profilers
 118 (ITP) consistently report warmer temperatures (Fig. 1) than provided by both the Po-

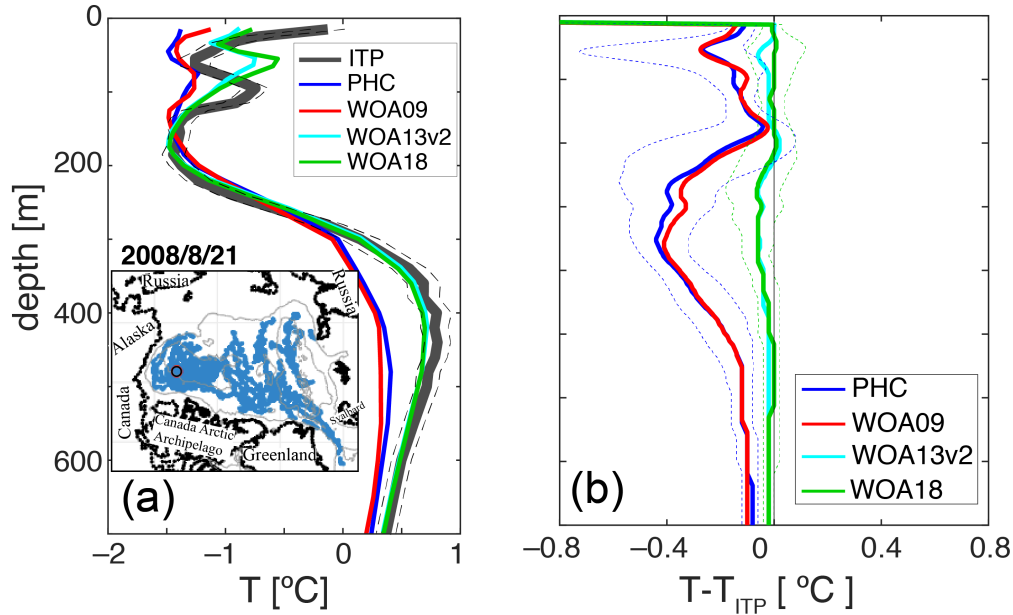


Figure 1. Comparison between ITP-derived temperature and the climatologies from the Polar Hydrography Center (PHC, blue), World Ocean Atlas 2009 (WOA09, red), 2013 version 2 (WOA13v2, cyan), and 2018 (WOA18, green). Panel (a) shows this comparison for a single ITP profile on August 21, 2008 (thick dark gray, with the observational uncertainty shown by the thin dashed black lines). The location of the profile is shown in the inset. Panel (b) shows the 50th percentile difference between all ITP temperature profiles in the Canada Basin and the four climatologies. The dotted lines show the 30th and 70th percentile differences.

119 lar Hydrographic Climatology (PHC, Steele et al., 2001) and the World Ocean Atlas 2009
 120 (WOA09, Locarnini et al., 2010; Antonov et al., 2010), but are in close agreement with
 121 WOA18. Here it is important to note that this close agreement at the time/location of
 122 data acquisition is built into the majority of these climatologies and other existing Arctic
 123 model-data syntheses. These products are constructed using statistical methods such
 124 as optimal interpolation (e.g., PHC, WOA), 3D-Var, or sequential 4D-Var with short as-
 125 similation windows (Stammer et al., 2016; Uotila et al., 2019; Mu et al., 2018; Carton
 126 et al., 2019). The advantage of these methods is that the synthesis ensures a local fit to
 127 available observations (Fig. 1, Carton et al., 2019). Away from observed locations, how-
 128 ever, the interpolator relies on incomplete, unavailable or unobtainable information. Miss-
 129 ing values are, for example, determined via spatial/temporal correlations, potentially de-
 130 rived from regions/times of very different dynamics. By construction, high frequency vari-
 131 ability cannot be fully accounted for and as a result spectral agreement with observa-
 132 tions can be poor (Verdy et al., 2017). Importantly, this type of interpolation – and that
 133 used in 3D-Var or sequential 4D-Var – can introduce artificial sources/sinks (e.g., of mass
 134 and enthalpy, Wunsch & Heimbach, 2013), making the resultant product unsuitable for
 135 robust identification and attribution of change (Stammer et al., 2016).

136 To provide additional support to studies of the Arctic ocean-sea ice system on decadal
 137 time scales we have developed a new model-data synthesis utilizing the non-linear in-
 138 verse modeling framework developed within the consortium for Estimating the Circulation
 139 and Climate of the Ocean (ECCO, Stammer et al., 2002; Wunsch & Heimbach,
 140 2007; Heimbach et al., 2019). The use of the primitive equations as a dynamical inter-
 141 polator distinguishes our effort from purely statistical approaches. The inversion con-

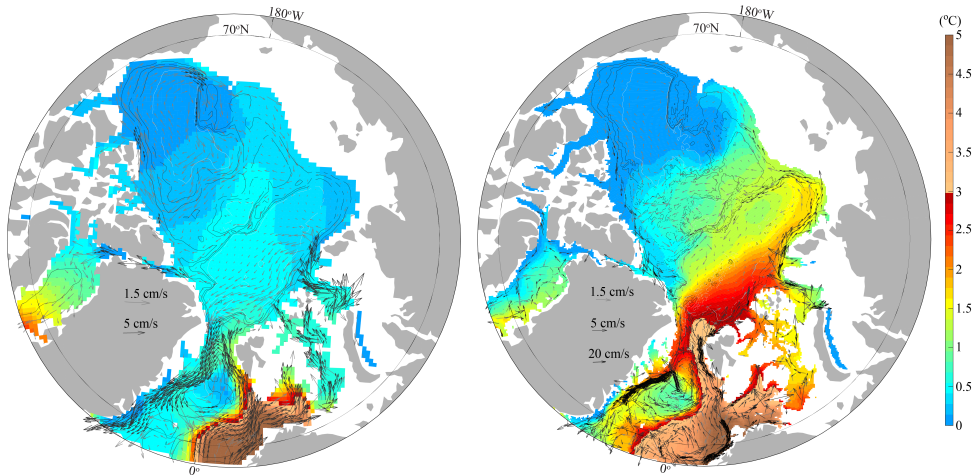


Figure 2. 2002–2015 mean circulation in the Arctic at depth 250 m as represented in ECCOv4r3 (left) and ASTER1 (right). The color scale shows temperature at the same depth from the two solutions. Vector arrows are grouped into speed ranges of [0–1.5] cm/s (light gray), [1.5–10] cm/s (dark gray) and >[10–20] cm/s (black), with the vector length scales provided for 1.5 cm, 5 cm, and 20 cm.

142 consists of an iterative, gradient-based minimization of a least-squares model-data misfit func-
 143 tion. Unlike most reanalysis products that are based on sequential data assimilation, only
 144 independent, uncertain input variables, i.e. initial conditions, surface boundary condi-
 145 tions and model parameters are adjusted. No periodic analysis increments during the
 146 estimation period that would incur artificial sources or sinks are permitted. Through strict
 147 adherence to conservation laws, all sources and sinks within the state estimate can be
 148 accounted for over the full estimation period, permitting meaningful analysis of closed
 149 budgets (Buckley et al., 2014; Piecuch & Ponte, 2012).

150 Our work builds upon extensive prior efforts of the ECCO community to produce
 151 the best kinematically- and dynamically-consistent data-constrained estimates of the ocean
 152 state across the globe and in various regional domains. Among the publicly available ECCO
 153 state estimates is ECCO Version 4 Release 3 (ECCOv4r3, Forget, Campin, et al., 2015;
 154 Fukumori et al., 2018), which has been constrained to satellite and Argo data outside
 155 of the Arctic, ITP data in the Arctic, and other mooring data at important Arctic gate-
 156 ways. The ECCOv4 releases have been widely used, with applications including inves-
 157 tigation of global vertical heat and salt redistribution (Liang et al., 2017; Liu et al., 2019),
 158 heat budgets in the North Atlantic (Buckley et al., 2014, 2015; Piecuch et al., 2017; Foukal
 159 & Lozier, 2018) and the Nordic Seas (Asbjørnsen et al., 2019), high-latitude freshwater
 160 budgets (Tesdal & Haine, 2020), and sea level change (Piecuch & Ponte, 2013).

161 The state-estimation procedure entails reducing the total time- and space-integrated
 162 model-data misfit. Since ECCOv4r3 is a global solution, reduction of the relatively well-
 163 sampled misfit at lower latitudes dominates the production of this solution. As a result,
 164 ECCOv4r3 possesses notable biases in the Arctic (Carton et al., 2019; Tesdal & Haine,
 165 2020), including a strong anticyclonic circumpolar circulation of Atlantic Water (Fig. 2).
 166 Furthermore, the ECCOv4r3 horizontal grid spacing of 40–45 km is well above the Rossby
 167 deformation radius in the Arctic and Nordic Seas (Nurser & Bacon, 2014). This has mo-

168 tivated a dedicated effort to build a higher resolution regional state estimate covering
 169 the 21st century for use in Arctic decadal climate research, culminating in the Arctic Sub-
 170 polar gyre sTate Estimate (ASTE).

171 Here we describe the first release of ASTE (*ASTE_R1*), providing an estimate of
 172 the ocean-sea ice state for the period 2002–2017. We describe the model configuration,
 173 observational constraints and the state estimation machinery (section 2) and present the
 174 model-data misfit reduction (section 3). We then compare our estimates of volume, heat
 175 and freshwater transports through important Arctic gateways with those in the exist-
 176 ing literature as well as present an analysis of *ASTE_R1* heat and freshwater budgets
 177 for the Arctic Ocean, Greenland-Iceland-Norwegian (GIN) Seas and subpolar North At-
 178 lantic (section 4). In section 5 we examine how an improved fit is achieved, identifying
 179 key adjustments of our independent control variables, and review remaining issues in *ASTE_R1*
 180 . In section 6 we summarize key findings and discuss future directions.

181 2 Methodology

182 2.1 Model Description

183 The coupled ocean-sea ice model underlying the estimation framework is an evolved
 184 version of the Massachusetts Institute of Technology general circulation model (MIT-
 185 gcm; Marshall et al., 1997; Adcroft et al., 2018). The model solves the primitive equa-
 186 tions in rescaled z^* coordinates (Adcroft & Campin, 2004) with a full non-linear free sur-
 187 face (Campin et al., 2004). The dynamic-thermodynamic sea ice model is an evolved ver-
 188 sion of Menemenlis et al. (2005); Losch et al. (2010); Heimbach et al. (2010). Eddy-induced
 189 tracer mixing and transports along isopycnal surfaces are parameterized following Redi
 190 (1982); Gent and McWilliams (1990).

191 The model uses a finite-volume discretization in a so-called “latitude-longitude-polar-
 192 cap” grid configuration (LLC grid, Forget, Campin, et al., 2015). The LLC grid is topo-
 193 logically equivalent to a cubed-sphere grid (Adcroft et al., 2004), but reverts to a reg-
 194 ular latitude-longitude grid equatorward of $\sim 57^\circ\text{N}$. The computational cost associated
 195 with solving the non-linear optimization problem for eddy-resolving simulations, which
 196 would need to require resolutions well below 4–15 km for the Arctic Mediterranean (Nurser
 197 & Bacon, 2014), is prohibitively high. As a compromise, ASTE is based on the medium-
 198 resolution LLC-270 grid, providing a nominal grid spacing of $1/3^\circ$, which corresponds
 199 to ~ 22 km in the North Atlantic, ~ 16 km in the Nordic Seas, and ~ 14 km in the high
 200 Arctic interior (Fig 3).

201 The ASTE domain covers the entire Atlantic northward of 32.5°S , the entire Arc-
 202 tic and its surrounding seas (Labrador, Nordic, Barents, Bering north of 47.5°N) and the
 203 Canadian Archipelago. The model has 50 unevenly spaced vertical height levels; thick-
 204 nesses range from 10 m at the surface to 500 m at 5000 m depth. Partial cells (Adcroft
 205 et al., 1997) are used to improve the representation of topography. The domain has bound-
 206 aries at 35°S in the South Atlantic, 48.6°N in the Pacific, and at the Gibraltar Strait.
 207 Rationales for choosing a full Atlantic-Arctic domain for ASTE – rather than limiting
 208 it to the Arctic Mediterranean – are to extend the applicability of the solution to inves-
 209 tigation of latitudinal connectivity between Atlantic and Arctic variability on decadal
 210 timescales, and to displace the imposed open boundary conditions far from the region
 211 of key interest.

212 We prescribe lateral open boundary conditions from the global ECCOv4r3 solu-
 213 tion, which has been shown to be in good agreement with large-scale constraints from
 214 Argo and satellites. The bathymetry is a merged version of W. H. F. Smith and Sandwell
 215 (1997), version 14.1, below 60°N and the international bathymetric chart of the Arctic
 216 Ocean (IBCAO, Jakobsson et al., 2012) above 60°N , blended over a range of ± 100 km
 217 about this latitude. Special attention was paid to remove abrupt jumps over the merged

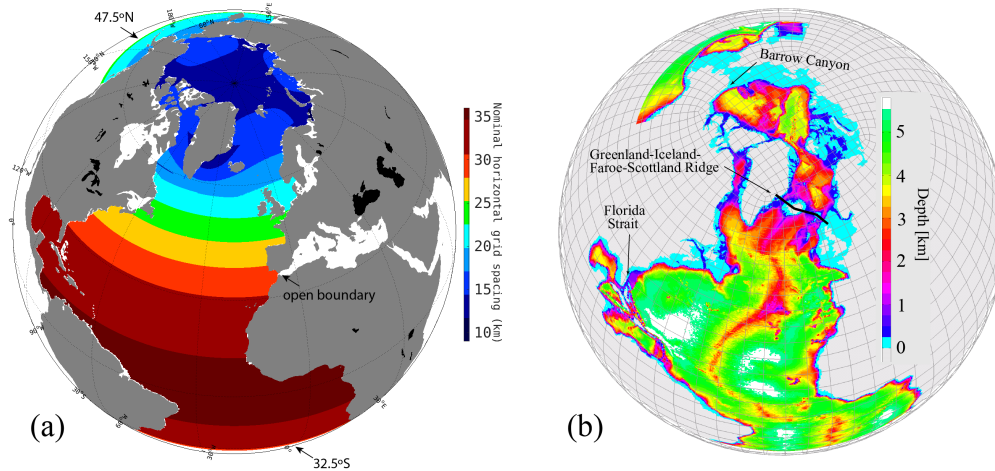


Figure 3. (a) Nominal horizontal grid spacing (km) and (b) the bathymetry in ASTE. The lateral open boundaries of the ASTE domain are at 47.5°N in the North Pacific, 32.5°S in the South Atlantic, and at the Gibraltar Strait. White areas in (a), which include the Hudson Bay, Baltic Sea, White Sea, Gulf of St. Lawrence, and all channels in the Canadian Arctic Archipelago except Nares and Barrow Straits, are masked. Depths of several important channels, including the Barrow Canyon, Greenland-Iceland-Faroe-Scotland Ridge and the Florida Strait, were carefully inspected to ensure transports consistent with published observations.

218 region. Model depths within important canyons (e.g. Barrow) and across important gate-
 219 ways (e.g., Florida Straits, Greenland-Iceland-Faroe-Scotland ridge, Aleutian islands chain,
 220 Gibraltar Strait) were enforced to be consistent with observations in order to realisti-
 221 cally simulate key transports and regional circulations.

222 Atmospheric forcing is applied via bulk formulae (Large & Yeager, 2008) over the
 223 open ocean, with the initial estimate of the atmospheric state variables from JRA-55 (Kobayashi
 224 et al., 2015). We considered taking ERA-Interim (Dee et al., 2011) – employed by EC-
 225 COv4r3 (Forget, Campin, et al., 2015; Fukumori et al., 2018) – as our first guess. How-
 226 ever, this product has a well documented warm bias of up to 2°C in the Arctic (Beesley
 227 et al., 2000; Freville et al., 2014; Jakobson et al., 2012; Lupkes et al., 2010) that causes
 228 excessive sea ice melt. ECCOv4r3 accommodated this warm bias through increased sea
 229 ice and snow wet albedos. Nguyen et al. (2011) showed reasonable modeled sea ice con-
 230 centration and thickness using the Japanese Reanalysis (JRA-25) without the need to
 231 increase sea ice albedos above their observed values. For this reason, the updated three-
 232 hourly, higher-resolution JRA-55 was chosen as the initial surface boundary forcing. Monthly-
 233 mean estuarine fluxes of freshwater are based on the Regional, Electronic, Hydrographic
 234 Data Network for the Arctic Region (R-ArcticNET) dataset (Lammers & Shiklomanov,
 235 2001; A. I. Shiklomanov et al., 2006).

236 As shown in Fig. 2 the ECCOv4r3 solution does not exhibit the anticyclonic cir-
 237 culation of Atlantic water in the Arctic that is inferred from hydrographic observations
 238 (Rudels, 2012). For this reason, we elected to initialize from alternative products. Ta-
 239 ble 1 summarizes our first-guess model input parameters for sea ice, ocean mixing and
 240 momentum dissipation, along with our choice of ocean-sea ice state to initialize the un-
 241 constrained simulation. This run serves as iteration 0 of the optimization and will be re-
 242 ferred to as *it0* for the remainder of the paper. Our selection is informed by existing obser-
 243 vation/model-based estimates. Importantly, sea ice albedos and drag coefficients are chosen within the
 244 range of observed and previously optimized estimates Nguyen et al. (2011).

245 The three-dimensional parametric horizontal stirring fields for temperature and salin-
 246 ity are based on typical values used in the literature (Pradal & Gnanadesikan, 2014), Campin,
 247 2014 (*pers. comm.*) with consideration for where the ASTE grid resolves the baroclinic
 248 deformation radius as follows. The vertical background diffusivity \mathcal{K}_d was set based on
 249 typical values at latitudes below 79°N of $\sim 10^{-5}$ m²/s and limited observed and mod-
 250 elled ranges of 10^{-7} to 10^{-6} m²/s at high latitudes (Padman & Dillon, 1988; Zhang &
 251 Steele, 2007; Nguyen et al., 2011; Fer, 2014; Sirevaag & Fer, 2012; Cole et al., 2014). Ver-
 252 tical diffusivities are enhanced by factor of 10 near the sea floor to mimic lee wave-driven
 253 mixing (Toole, 2007; Mashayek et al., 2017). Horizontal dissipation is applied as a com-
 254 bination of biharmonic Leith and Laplacian viscosity (Griffies, 2004; Fox-Kemper & Men-
 255 emenlis, 2008). At lower latitudes, where eddy effects are better resolved, we follow the
 256 formulation of Leith (1996) to represent the direct enstrophy cascade at mesoscales. Within
 257 the attached Gulf Stream, a higher Laplacian viscosity is initially required to reduce the
 258 Reynolds number and prevent premature separation (Dengg, 1993; Chassignet & Gar-
 259 rraffo, 2001; Chassignet & Marshall, 2013). In the Arctic Mediterranean, where the de-
 260 formation radius is 4–10 km, an ad-hoc combination of biharmonic Leith and Laplacian
 261 viscosity is used to ensure consistency of inflow velocity at the Fram Strait and an ap-
 262 proximate cyclonic circumpolar AW circulation inside the Arctic (Jochum et al., 2008,
 263 see Table. 1). The model is spun up for 6 years using repeated year 2002 atmospheric
 264 forcing and open boundary conditions (Table 1). The ocean, sea ice and snow states at
 265 the end of this 6 year spin up became the initial condition for the unconstrained *it0* in
 266 the optimization procedure described next.

267 2.2 State Estimation Framework

268 ASTE is formally fit to observations through a gradient-based iterative least-square
 269 minimization of the model-data misfit function that takes into account data and model
 270 parameter uncertainties (Nguyen et al., 2017). The gradient with respect to a high-dimensional
 271 space of uncertain input variables, the “controls”, is obtained via the adjoint of the model,
 272 derived by means of algorithmic differentiation (AD; Giering et al., 2005; Heimbach et
 273 al., 2005). The model-data misfit (or “cost”) function is defined as:

$$\begin{aligned}
 J = & [\mathbf{y}(t) - \mathbf{E}(t)\mathbf{x}(t)]^T \mathbf{R}(t)^{-1} [\mathbf{y}(t) - \mathbf{E}(t)\mathbf{x}(t)] \\
 & + [\mathbf{x}_0 - \mathbf{x}(0)]^T \mathbf{B}(0)^{-1} [\mathbf{x}_0 - \mathbf{x}(0)] \\
 & + \sum_{t=0}^{t_f-1} \mathbf{u}(t)^T \mathbf{Q}(t)^{-1} \mathbf{u}(t)
 \end{aligned} \tag{1}$$

274 where $\mathbf{y}(t)$ is the observation vector and $\mathbf{x}(t)$ the combined ocean and sea ice state vec-
 275 tor. The combined initial model state \mathbf{x}_0 and input parameters $\mathbf{u}(t)$ collectively com-
 276 prise the control vector $\mathbf{\Omega} \ni \{\mathbf{x}_0, \mathbf{u}(t)\}$. \mathbf{E} is the operator mapping the state variables
 277 to the observations. The model-data misfit $\mathbf{y}(t) - \mathbf{E}(t)\mathbf{x}(t)$ is weighted by the inverse
 278 error covariance matrix $\mathbf{R}(t)$. This accounts for both observational uncertainty and model
 279 representation error, where the latter considers the extent to which real variability can-
 280 not be represented at the chosen model resolution (Nguyen, Heimbach, et al., 2020). $\mathbf{B}(0)$
 281 and $\mathbf{Q}(t)$ are error covariances of \mathbf{x}_0 and $\mathbf{u}(t)$, respectively. Full knowledge of \mathbf{R} , \mathbf{B} , and
 282 \mathbf{Q} is often unattainable (Wunsch & Heimbach, 2007). As a result, the misfit $\mathbf{y}(t) - \mathbf{E}(t)\mathbf{x}(t)$
 283 and variables $\delta\mathbf{x}_0 = \mathbf{x}_0 - \mathbf{x}(0)$ and $\mathbf{u}(t)$ are often assumed Gaussian, with zero means
 284 and standard deviations whose squares fill the diagonal entries of their respective covari-
 285 ance matrices (Wunsch & Heimbach, 2007).

286 There are three distinct contributions to the misfit cost function, eqn. (1). The first
 287 term describes the normalized model-data squared misfit to be minimized. This term
 288 sums weighted contributions from all observational data considered. The second term

Field	Value	Reference	Note
Unconstrained run (<i>it0</i>)			
Ocean-sea ice state for Jan/2002 obtained after 6-yr spin up from:			
θ_0	WOA09	Locarnini et al. (2010)	Temperature
S_0	WOA09	Antonov et al. (2010)	Salinity
\mathbf{u}_0	0.0	–	Ocean velocity
A_{SI_0}	PIOMAS	Zhang and Rothrock (2003)	Sea ice concentration
h_{SI_0}	PIOMAS	Zhang and Rothrock (2003)	Sea ice thickness
\mathbf{u}_{SI_0}	0.0	–	Sea ice velocity
Sea ice parameters:			
$\alpha_{SI_{wet,dry}}$	0.7, 0.68	Johnson et al. (2007)	sea ice albedo
$\alpha_{sn_{wet,dry}}$	0.84, 0.77	Johnson et al. (2007)	snow albedo
$C_{da,dw}$	0.00114, 0.0054	Nguyen et al. (2011)	sea ice-[air,ocean] drag
Mixing and dissipation parameters:			
		Nguyen et al. (2011)	Below 50 m in
	–6.5 to –6.0	Zhang and Steele (2007)	eastern Arctic &
		Padman and Dillon (1988)	below 75 m
$\log_{10}(\mathcal{K}_z)$		Sirevaag and Fer (2012); Fer (2014)	in western Arctic
	–5	Munk (1966)	Outside the Arctic & near
	value plus 1	Mashayek et al. (2017)	Grid points next to land
\mathcal{K}_σ	50	Pradal and Gnanadesikan (2014)	South of 60°N
	17		North of 60°N
\mathcal{K}_{gm}	50	Pradal and Gnanadesikan (2014)	South of 60°N
	50		North of 60°N
ν	Leith	Leith (1968)	Ocean interior
	Ah=0.0005	Forget, Campin, et al. (2015)	Coastal south of 40.5°N
	Ah=0.003		Coastal north of 40.5°N
Optimized run (<i>ASTE_R1</i>)			
$\theta_0, S_0, \mathcal{K}_\sigma, \mathcal{K}_{gm}, \log_{10}(\mathcal{K}_z)$: optimized.			
$\alpha_{SI_{wet,dry}}, \alpha_{sn_{wet,dry}}, C_{da,dw}, \mathbf{u}_0, A_{SI_0}, h_{SI_0}, \mathbf{u}_{SI_0}$: same as <i>it0</i>			
ν	Leith	Leith (1968)	South of [70,73]°N in [Pacific, Atlantic] sector
	Ah=0.0054	Griffies (2004)	North of [70,73]°N in [Pacific, Atlantic] sector

Table 1. Values of initial ocean and sea ice state, sea ice parameters, and ocean mixing and dissipation for the unconstrained run *it0* and optimized *ASTE_R1* solution. ν is either the biharmonic (m^4/s) or harmonic (m^2/s) viscosity, and Ah is the harmonic viscosity coefficient (Griffies, 2004). Units for the mixing coefficients $\mathcal{K}_{[\sigma, gm, z]}$ are m^2/s

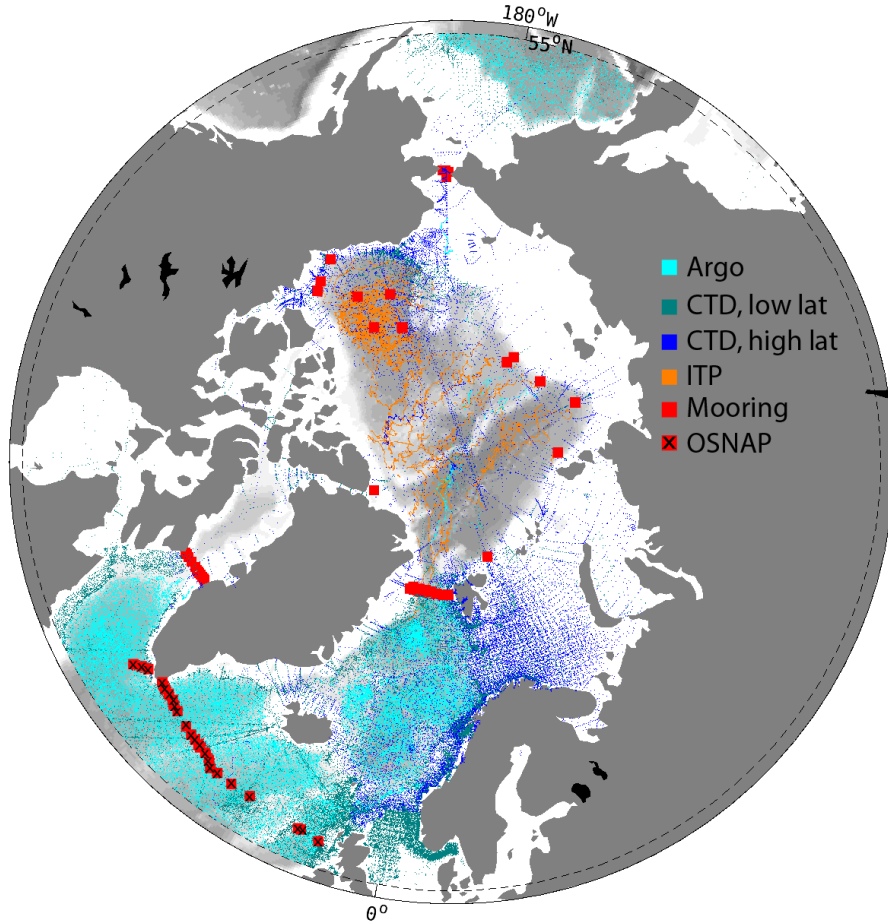


Figure 4. In situ observations used to constrain ASTE. Red squares with “x” are additional OSNAP mooring data, used for independent evaluation but not part of the cost function.

289 penalizes deviation of the initial state $\mathbf{x}(0)$ from the initial guess \mathbf{x}_0 (Table. 1). Similarly,
 290 the third term describes moderation of input parameter adjustments $\mathbf{u}(t)$ so that the ad-
 291 justment amplitude does not far exceed the uncertainties. The adjoint (or Lagrange multi-
 292 plier) method consists of augmenting the the cost function (eqn. (1)) with an additional
 293 term that enforces the strict adherence of the model to the underlying physics along the
 294 model full trajectory. Once the cost function J is defined, beneficial control adjustments
 295 that reduce the misfit are informed by the gradient $\nabla_{\Omega} J$. This gradient can be efficiently
 296 computed for very high-dimensional control spaces using the adjoint model (Wunsch &
 297 Heimbach, 2007). Control vector adjustments are determined iteratively using a quasi-
 298 Newton method. Control variable updates are used in a consecutive iteration, in which
 299 model, model-data misfit, and gradient are recomputed. This iteration is continued un-
 300 til little further misfit reduction is achieved between successive iterations. This is expected
 301 when $J \approx 1$, i.e., when the state estimate is in agreement with the observations to within
 302 the error $\mathbf{R}(t)$.

303 The ASTE control space $\{\mathbf{x}_0, \mathbf{u}\} \in \Omega$ comprises the 3D hydrographic initial condi-
 304 tions, potential temperature and salinity (θ_0, S_0) , the time-varying 2D surface atmo-
 305 spheric state variables, spatially-varying but temporally invariant model coefficients of
 306 vertical diffusivity (\mathcal{K}_z) and parameterized eddy activity $(\mathcal{K}_{\sigma}, \mathcal{K}_{gm})$, denoting the strength
 307 of eddy-induced isopycnal diffusivity and potential energy transfer, respectively (Forget,
 308 Ferreira, & Liang, 2015). The atmospheric state control variables are 2m air tempera-

309 ture, T_{air} , specific humidity, q_{air} , downward short- and long-wave radiation, R_{sw} , R_{lw} ,
 310 precipitation, P , and 10 m winds u_w, v_w . Although runoff and evaporation are not part
 311 of the control space, in practice they project onto the precipitation sensitivities, inter-
 312 preted as linear combination of net freshwater fluxes (evaporation minus precipitation
 313 minus runoff, E-P-R). To ensure the adjustments are physically reasonable, *a-priori* un-
 314 certainties (i.e. the square-roots of the diagonal terms of \mathbf{B} and \mathbf{Q}) are estimated fol-
 315 lowing Forget and Wunsch (2007) and Fenty and Heimbach (2013a) for oceanic hydrog-
 316 raphy and Chaudhuri et al. (2013, 2014) for atmospheric forcing.

317 The vector $\mathbf{y}(t)$ contains as many available ocean and sea ice observations as prac-
 318 tical. They include the standard suite of in-situ and remotely-sensed ocean and sea-ice
 319 data used in ECCOv4r3 (Fukumori et al., 2018), augmented by updated high latitude
 320 in-situ data at important Arctic gateways and in the Arctic interior. The estimation pe-
 321 riod chosen for ASTE, 2002–2017, leverages the increase in satellite (GRACE, ICESat-
 322 1/2, CryoSat-2) and in situ (ITP) observations in the Arctic. In total, approximately 1.2×10^9
 323 observations were employed to constrain distinct aspects of the modeled ocean and sea-
 324 ice state, culminating in the optimized *ASTE_R1* solution. Distinct datasets are sum-
 325 marized in Table 2. Key among these are satellite-based observations of sea level anoma-
 326 lies (SLA) to aid removal of the precipitation bias in JRA-55, Argo and lower latitude
 327 CTD to improve surface and sub-surface hydrography in the North Atlantic and Nordic
 328 Seas, and a suite of moorings in the Arctic. This suite includes the Fram Strait moor-
 329 ing array to constrain the boundary current strength and heat flux from the Nordic-Seas
 330 into the Arctic, and the combined ITP and Beaufort Gyre moorings to constrain the Canada
 331 Basin hydrography. Finally, OSSISaf daily sea ice concentration was essential for con-
 332 straining the ice edge and upper ocean hydrography in the Arctic and its surrounding
 333 marginal seas.

334 The practical implementation of eqn. (1) follows that described in Forget, Campin,
 335 et al. (2015). Several approximations to parameterization in the adjoint model were made
 336 to ensure stable behaviour. Maximum isopycnal slopes are limited in the GM/Redi pa-
 337 rameterization, the vertical mixing scheme (K-Profile Parameterization, Large et al., 1994)
 338 is omitted in the adjoint, and increased horizontal and vertical momentum dissipation
 339 are employed in the adjoint to suppress fast growth of unstable sensitivity.

340 The full sea ice adjoint, as described in Fenty and Heimbach (2013a); Fenty et al.
 341 (2015), was not used in this study (nor in ECCOv4), due to persistent instability issues.
 342 In its place, the sea ice concentration model-data misfit is used to relate air-sea fluxes
 343 to the enthalpy of the integrated surface ocean-sea ice system as follows. Where the model
 344 has an *excess/deficiency* of sea ice, extra heat is added to/removed from the system to
 345 bring the sea surface to above/below the freezing temperature. In these two cases, the
 346 pseudo-sea ice cost function contributions $J_{\text{seaice_conc.}[ex,de]}$ are in enthalpy units rather
 347 than normalized model-data misfits. Normalization is chosen to obtain amplitudes com-
 348 parable to other model-data misfits J_i contributing to the total cost function J , so that
 349 these terms play an active role in the optimization. Lastly, convergence – if achievable
 350 for these two pseudo-sea ice costs – is when they approach zero and not unity.

351 After 62 iterations, adjustments are obtained for the initial conditions, 3D inter-
 352 nal mixing fields, and surface atmospheric state. The initial conditions of the optimized
 353 state, ASTE Release 1 (*ASTE_R1*), are derived by adding the adjustments $[\Delta\theta, \Delta S]_{i62}$
 354 to the first guess fields $[\theta, S]_{i0}$. The same holds for the optimized mixing fields and sur-
 355 face atmospheric state (see Table 1).

356 The full monthly mean state of *ASTE_R1* is distributed via the ECCO & ASTE
 357 data portal at the Texas Advanced Computing Center (TACC). In addition, the model
 358 configuration, required input fields and code are distributed to enable reruns (see Ap-
 359 pendix A). Since the focus of ASTE is on the North Atlantic and the Arctic Ocean, we
 360 restrict both the discussion presented below and the distributed *ASTE_R1* fields to lat-

itudes above 10°N . As for ECCOv4r3, the mass, salt, and heat budgets in *ASTE_R1* are fully closed when computed using the distributed standard ECCO diagnostics that we provide. In Appendix B, we show how lateral transports may be accurately computed and provide estimates for the errors incurred in offline calculations using the *ASTE_R1* monthly mean diagnostics.

2.3 Making Meaningful Model-Observation Comparisons

A meaningful assessment of *ASTE_R1* through comparison with observations is non-trivial and requires careful consideration. One of the biggest challenges is properly accounting for the sparse spatio-temporal sampling and the potential for aliasing. For example, measurements might only be taken at a discrete location (e.g. a mooring) or along-track (i.e., with high along-track coverage and drastically lower resolution in the cross-track direction) or only during summer months (e.g., ship-based CTD). “Averages” of these measurements (e.g., average Argo or ITP data over 1 month or 1 year) incurs aliasing in both space and time as well as potential spatial or seasonal biases. “Averages” of *ASTE_R1* outputs at the smallest spatial scale (grid cell size), on the other hand, are over a spatial area of $\sim 200 \text{ km}^2$. Unless observations are well sampled over this grid-area, a direct comparison between observations and *ASTE_R1* can be problematic. Furthermore, *ASTE_R1* does not resolve eddies in the Arctic and GIN Seas. As a result, we should neither expect nor demand a perfect fit to discrete (in space/time) measurements. The ECCO framework utilizes “representation errors” in the weighting of the model-data misfits, eqn. (1), to safeguard against over-fitting and facilitate more meaningful model-data comparison (Wunsch & Heimbach, 2007). However, these representation errors are themselves highly unconstrained often relying on unconstrained high-resolution model runs for their derivation (see Nguyen, Heimbach, et al., 2020, for a more detail discussion).

In Section 3 we present both normalized misfit reductions as well as comparisons of dimensional transports and heat/freshwater contents. For the dimensional quantities, several potential challenges can emerge related to resolution and bias issues, which we briefly discuss in the following. A serious challenge stems from the need to compare watermasses in the presence of hydrographic biases. From observations, watermasses are often defined in temperature, salinity, and density (T, S, σ) space with tight thresholds/bounds reflecting the measurement precision (e.g. to the first or second decimal place). These definitions can be problematic to adopt in *ASTE_R1*, where we are averaging over grid-cell areas of $\sim 200 \text{ km}^2$ and thicknesses of 10–500 m. Furthermore, in some regions the model representation errors may be up to an order of magnitude larger than measurement precision. In these regions, the normalized misfit can be within acceptable range but *ASTE_R1* can still possess notable absolute (T, S, σ) biases if the representation errors are large. For this reason, a watermass is likely to exist in *ASTE_R1* but with modified thresholds/bounds. Where appropriate, we analyzed *ASTE_R1* carefully in (T, S, σ) space to identify suitable classifications for calculation of watermass transports. Details on the modified bounds are provided in Appendix C.

A second challenge is related to the region over which derived quantities are computed. In cases where these regions are defined with geographic bounds based on availability of observations rather than dynamical regimes, the equivalent derived quantities in *ASTE_R1* can be highly sensitive to small shifts in bounding region, especially when the grid resolution and uncertainties in the control input parameters (e.g., forcing, internal mixing) are taken into account. For this reason, we also explore the sensitivity of area/volume integrals to choice of geographical bounds in Appendix C.

Lastly, comparison of (dimensional) integrated transports can be problematic due to spatial sampling issues and representation error, preventing precise estimation of narrow boundary currents in *ASTE_R1*. An example is at the Fram Strait, where the *ASTE_R1* grid cannot resolve the e-folding scale of the West Spitsbergen Current (Beszczynska-

Data Type	Spatial coverage	Temporal coverage	Description	Source	
Sea ice					
Velocity ¹	N.Hemis	2002–2012	passive microwave & AVHRR & IABP	rkwok.jpl.nasa.gov/radarsat/3dayGr.table.html nsidc.org/data/docs/daac/nsidc0116.icemotion.gd.html Kwok and Cunningham (2008), Fowler et al. (2013)	
	N.Hemis	2012–2015	ASCAT & SSMI	ftp.ifremer.fr/ifremer/cersat/products/gridded/psi-drift	
Thickness ¹	N.Hemis	2011–2017	CryoSat-2	www.meereisportal.de/datenportal.html & Ricker et al. (2017)	
	N.Hemis	2010–2017	SMOS	icdc.zmaw.de/l3c-smos_sit.html & Tian-Kunze et al. (2014)	
	N.Hemis	2003–2008	ICESat	rkwok.jpl.nasa.gov/icesat/index.html & Kwok and Cunningham (2008); Kwok et al. (2009)	
Concentration	N.Hemis	2002–2017	SSMI & OSISaf	osisaf.met.no/p/ice/index.html & Lavergne et al. (2019)	
Ocean					
ITP (T,S)	Arctic	2004–2017	Profilers	www.whoi.edu/itp/data/ Krishfield et al. (2008), Toole et al. (2011); Krishfield (2020),	
Hydrographic Survey (T,S)	GINs	2002–2006	ASOF	www.pangaea.de/	
	Beaufort Sea	2003–2017	BGOS	www.whoi.edu/beaufortgyre/home/ doi.pangaea.de/10.1594/PANGAEA.761766 & Bauch et al. (2009)	
	Laptev Sea	2002–2003		doi.pangaea.de/10.1594/PANGAEA.763451 & Bauch et al. (2011)	
	East Arctic	2007		doi.pangaea.de/10.1594/PANGAEA.763451 & Bauch et al. (2011)	
Mooring (T,S,currents)	GINs	2002–2013		Våge et al. (2015)	
	Fram Strait	2002–2017	ASOF	Fahrback et al. (2001), Beszczynska-Möller et al. (2012)	
	East Arctic	2002–2015	NABOS	nabos.iarc.uaf.edu/ , Pnyushkov et al. (2013) and	
	West Arctic	2002–2015	CABOS	Polyakov et al. (2012)	
	Beaufort Gyre	2004–2017	BGOS	www.whoi.edu/website/beaufortgyre/data psc.apl.washington.edu/HLD/Bstrait/Data/ & Woodgate (2018)	
Transports ¹ of Vol & Heat & Freshwater	Bering Strait	2002–2017		iop.apl.washington.edu/data.html , Curry et al. (2011)	
	Davis Strait	2004–2015			
T,S	Fram Strait	2002–2017	ASOF	Schauer and Fahrback (2004) & Beszczynska-Möller et al. (2012)	
	Bering Strait	2002–2017	mooring	Woodgate (2018)	
	High Latitude		2002–2015	IARC	oregon.iarc.uaf.edu/dbaccess.html
				IARC	climate.iarc.uaf.edu/geonetwork/srv/en/main.home
				ICES	ocean.ices.dk/HydChem/HydChem.aspx?plot=yes
CAA	2002–2015	SBI	www.eol.ucar.edu/projects/sbi/		
Arctic	2002–2015	BIO	www.bio.gc.ca/science/data-donnees/base/run-courir-en.php		
Arctic	2002–2015	ACADIS	www.aoncadis.org/home.htm		
	Arctic	2002–2015	WHOI	(Krishfield, 2020)	

Table 2. Satellite and *in situ* data currently used to constrain or assess ASTE in addition to the standard ECCOv4r3 set. ¹datasets that are used only for assessment and not part of the cost function.

413 Möller et al., 2012). Enforcing fit to the observed mooring velocity would likely result
 414 in an overestimation of the net inflow volume transport here. In *ASTE_R1*, velocities
 415 at gateways were not employed as active constraints but were used for offline assessment
 416 of the derived transports. Ultimately, however, the spacing between discrete moorings
 417 offers incomplete information on the total volume transports across a given gateway, and
 418 existing observation-based estimates generally require various assumptions on spatial/temporal
 419 correlations in order to interpolate between the mooring measurements. As a result, our
 420 direct comparisons of *ASTE_R1* and observation-based transports presented below seeks
 421 consistency in terms of sign and order of magnitude rather than exact agreement of am-
 422 plitude. This is especially true for assessment of *ASTE_R1* heat/freshwater transports,
 423 computed relative to the wide range of reference values used in the literature.

424 3 Model-data misfit reduction and residuals

425 We begin by assessing the *ASTE_R1* solution in context of existing observation-
 426 based estimates of the circulation and hydrography in the Arctic. We summarize the re-
 427 duction in the integrated model-data misfits and costs achieved in the production of *ASTE_R1*
 428 . We then expand this discussion, considering the *ASTE_R1* fit to constraints in the Ar-
 429 ctic, GIN Seas, and Subpolar North Atlantic in turn (sections 3.1-3.3). Note that assim-
 430 ilation aids – but by no means guarantees – model-data consistency due to errors and/or
 431 deficiencies in the data, model, and/or state estimation framework. This point will be
 432 revisited in our discussion in section 5. We refer to “misfit” as the dimensional model
 433 minus data difference, “normalized misfit” as misfit scaled by the respective uncertainty
 434 (dimensionless), and “normalized cost” or “cost” as the square of the normalized mis-
 435 fit (dimensionless). The overall cost reductions in *ASTE_R1* have been grouped into sev-
 436 eral categories as shown in Fig. 5 and summarized in Table 3.

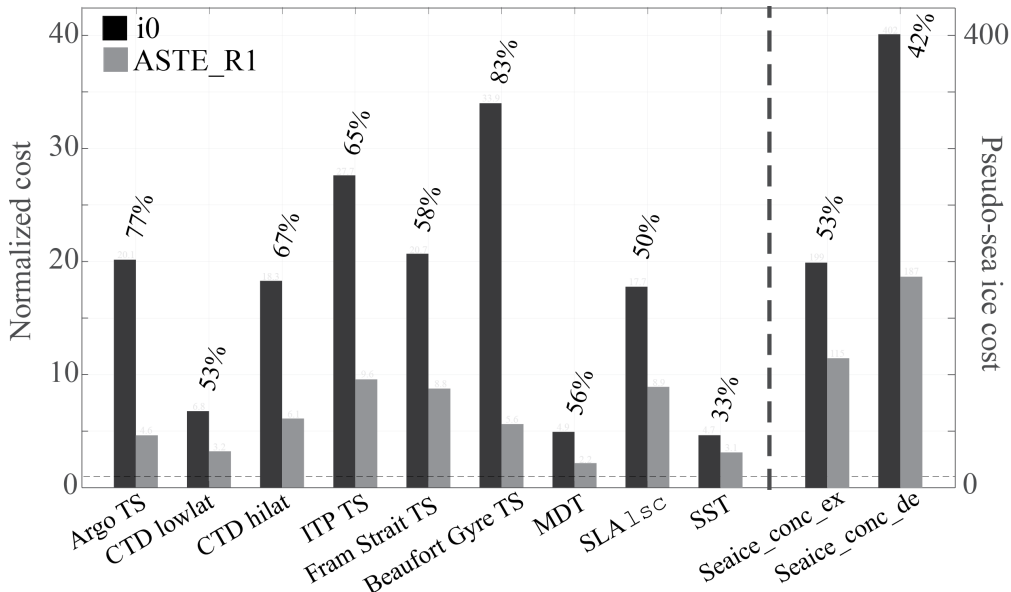


Figure 5. Individual costs calculated from key data sets that were used in the optimization. The numbers listed above each data set are the percentage of cost reduction in *ASTE_R1* compared to *it0*. The magnitudes of the two pseudo-sea ice costs are indicated on the right y-axis.

Cost name	Normalized cost		Percentage reduction (%)
	<i>it0</i>	<i>ASTER1</i>	
$J_{\text{Argo_TS}}$	20.1	4.6	77
$J_{\text{CTD_lowlat}}$	6.8	3.2	53
$J_{\text{CTD_hilat}}$	18.3	6.1	67
$J_{\text{ITP_TS}}$	27.7	9.6	65
$J_{\text{FramStrait_TS}}$	20.7	8.8	58
$J_{\text{BeaufortGyre_TS}}$	33.9	5.6	83
$J_{\text{BeringStrait_TS}}$	6.3	4.2	33
$J_{\text{DavisStrait_TS}}$	3.8	4.3	-11
$J_{\text{NABOS_TS}}$	43.1	25.3	41
$J_{\text{StAnnaTrough_TS}}$	22.9	7.2	69
$J_{\text{seaice_conc_ex}}$	402	187	53
$J_{\text{seaice_conc_de}}$	199	115	42
$J_{\text{SST_}[\text{Reynolds+TMI/AMSRE}]}$	4.7	3.1	33
J_{MDT}	4.9	2.2	56
$J_{\text{SLA_}[\text{gfo+ers+tp}]}$	2.7	1.4	49
$J_{\text{SLA_lsc}}$	17.7	8.9	50
<hr/> <hr/>			
$J_{\text{seaice_area15}}^{(o)}$	1.0	0.36	64
$J_{\text{seaice_extent15}}^{(o)}$	1.0	0.17	83
$J_{\text{seaice_thickness}}^{(o)}$	22.0	25.8	-17
$J_{\text{seaice_UV}}^{(o)}$	2.1	1.6	23
$J_{\text{FramStrait_vNorth}}^{(o)}$	1.3	1.0	26
$J_{\text{NABOS_mmpUV}}^{(o)}$	2.0	1.6	23
$J_{\text{OSNAP_TS}}^{(o)}$	6.3	3.5	44
$J_{\text{lineW_TS}}^{(o)}$	3.3	2.5	26

Table 3. Active and offline costs and reductions in *ASTER1* compared to *it0*. The quantities listed above the triple horizontal lines contribute directly to the total J in Eqn 1, while those listed below the triple horizontal lines ($J^{(o)}$) are used only for offline assessment and do not influence the optimization. The offline sea ice area and extent (both defined using the common 15% cutoff threshold) costs are normalized by the Arctic Mediterranean’s area.

3.1 Arctic

3.1.1 Sea ice

Improved representation of sea ice extent in *ASTE_R1* (compared to the unconstrained simulation) is indicated by a significant reduction of $J_{\text{seaiceconc[ex,dec]}}$ by 53% and 42%, respectively (Table 3, Fig. 5). Fenty and Heimbach (2013b) showed that these improvements can be effectively achieved through small adjustments of atmospheric controls, within their uncertainty range. These improvements are independently confirmed by the reduction in passive misfits for sea ice area ($J_{\text{seaice_area15}}$, 64%) and extent ($J_{\text{seaice_extent15}}$, 83%) (Table 3). The largest improvements occur in the seasonal ice zones e.g., Greenland and Barents Seas and Southern Beaufort Gyre (Fig. 6a) associated with a systematic decrease in total simulated area/extent without alteration of the seasonal cycle (Fig. 6b).

The improved sea ice edge representation in *ASTE_R1* (Fig. 6e,h) is accompanied by a reduction in the passive misfits for sea ice velocities ($J_{\text{seaice_vel}}$, Table 3), primarily in locations where nonzero ice velocities in *it0* were accompanied by observations of zero ice concentration and vice versa. Unlike velocity, however, the sea ice thickness costs $J_{\text{seaice_thickness}}$ did not decrease (Table 3), primarily because the pseudo-sea ice adjoint does not contain physics relating ice thickness to the atmospheric forcing or ocean interaction from below. We will return to this in section 6.

3.1.2 Fram Strait

The dynamics in the vicinity of the Fram Strait are highly complex, governed by strong air-ice-ocean interaction, vigorous generation of eddies associated with highly sheared boundary currents and their recirculations in the presence of significant topographic steering (Beszczynska-Möller et al., 2012; de Steur et al., 2014; von Appen, Schauer, Hattermann, & Beszczynska-Möller, 2015; von Appen, Schauer, Somavilla Cabrillo, et al., 2015; Hattermann et al., 2016). Due to this complexity, correct simulation of Atlantic Water inflow from the Nordic Seas is non-trivial (e.g., Nguyen et al., 2011; Ilicak et al., 2016; Docquier et al., 2019) and the local moorings provide an important constraint.

Daily-average moored velocity for the years 2002–2011 at various depths along the entire array (Beszczynska-Möller et al., 2011, 2012) were used to constrain the *ASTE_R1* velocity across the strait. The mooring temperature and salinity constrain the inflow and outflow of AW. Additional data available for the years 2012–2017 (von Appen, Schauer, Somavilla Cabrillo, et al., 2015) were withheld from the optimization and used instead for offline evaluation. We find that optimizing the circulation to the 2002–2011 data yields AW properties which are also consistent with the 2012–2017 data withheld.

Fig. 7 shows the unconstrained *it0* and *ASTE_R1* misfits to moored T , S , and northward velocity. The normalized misfit in temperature as a function of longitude is reduced by 71% compared to the unconstrained *it0* simulation (Fig. 7a). On the shelf west of 4°W , *ASTE_R1* has a warm bias compared to the observations, which resulted in higher misfits here (red bar between longitude 8.1°W and 4.1°W in Fig. 7a). The reduction in misfits for inflow of the AW, however, is more important for the large-scale Arctic hydrography, as AW passing through this important gateway propagates along the entire boundary of the Eastern Arctic and into the Canada Basin. Here its properties can be compared to ITP data, which serve as the main constraint on subsurface T/S over the entire pathway from the Fram Strait (see section 3.2.3). The misfit reduction can be seen for one example mooring at approximately 8°E (Fig. 7d–f) at multiple depths. The significant improvement in salinity at the surface (dashed blue in Fig. 7e) is related to the improved ice edge (see also Fig. 6c–e). Another significant improvement is in the AW core temperature at depth ~ 250 m (solid blue and red lines in Fig. 7d).

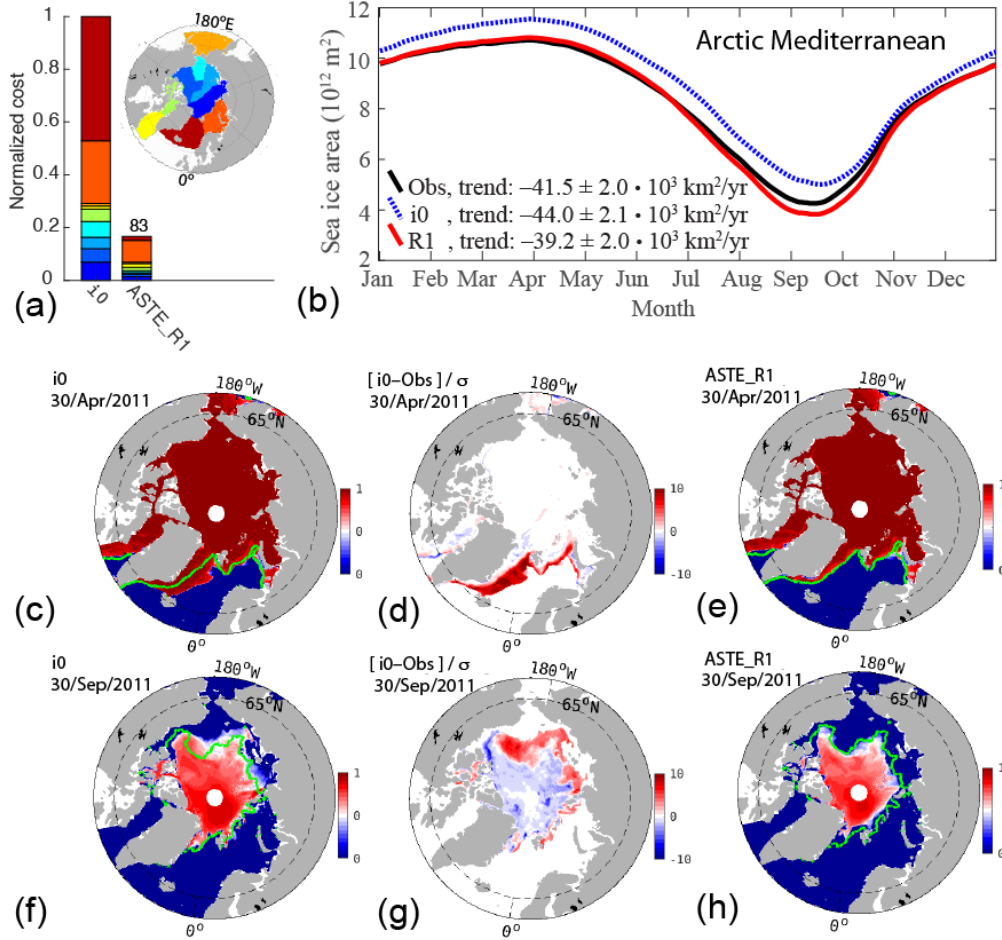


Figure 6. Comparison of sea ice misfits in the Arctic Mediterranean, for the unconstrained *it0* and fully optimized *ASTE_R1* solution, assuming the standard 15% cutoff threshold for both total ice area and extent. Comparison of (a) cost (misfit squared) to observed sea ice extent, $J_{\text{seaice_extent15}}^{(o)}$, showing contributions from individual basins. Comparison of (b) 12-month climatology of sea ice area, also showing observation-based climatology from OSSISaf (black). The climatology and the trends listed in the legend were derived from the 01/Jan/2002–31/Dec/2017 time-series. Comparison of daily sea ice concentration between (c,f) *it0* and (e,h) *ASTE_R1* for days selected at times of (c,e) maximum and (f,h) minimum ice extent. The green contour in panels (c,e,f,h) delineates the observed sea ice concentration from OSSISaf at the indicated dates. The optimization acts to reduce concentration at the ice margin where notable biases exist in *it0*. These biases are shown normalized by uncertainty in the OSSISaf observations for (d) 30/Apr/2011 and (g) 30/Sep/2011.

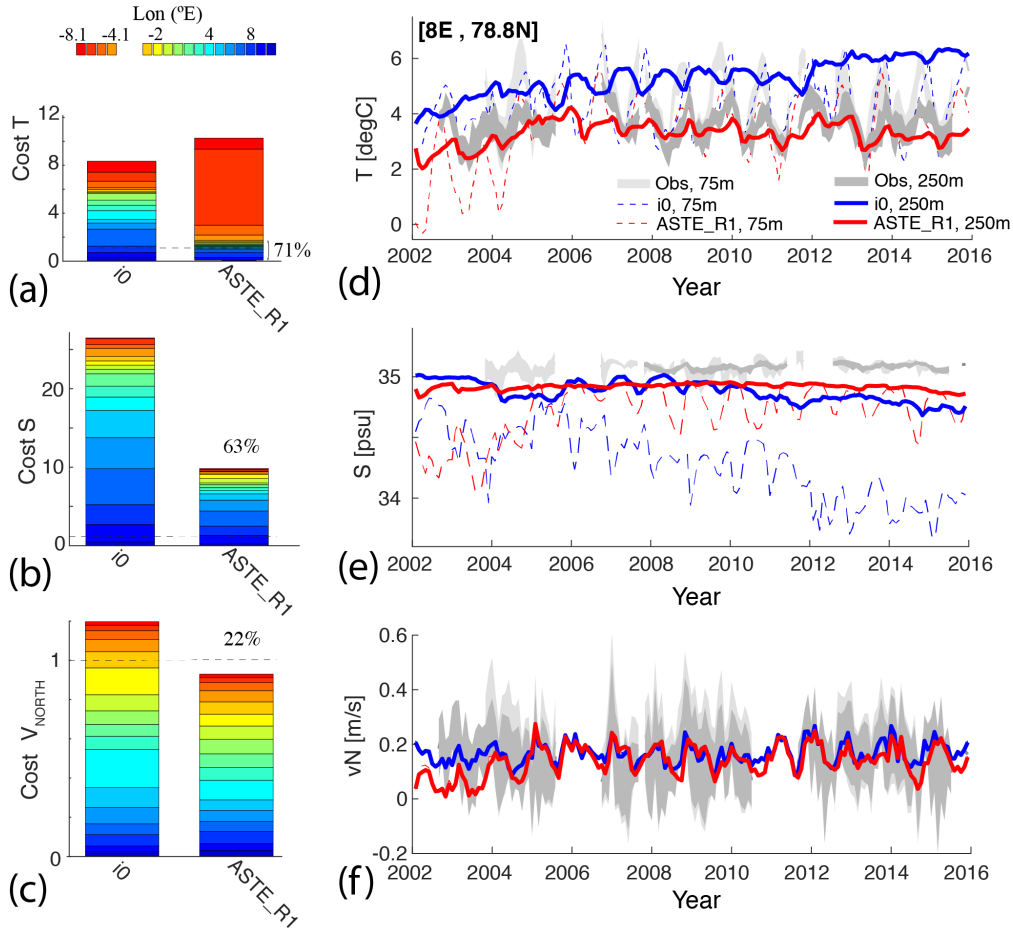


Figure 7. Normalized cost at Fram Strait for (a) temperature, (b) salinity, and (c) northward velocity between moored observations and unconstrained *it0* and *ASTE_R1* solutions, plotted as a function of longitude. Time series of (d) temperature, (e) salinity, and (f) northward velocity at one example mooring at [8°E,78.8°N] for depths 75 m and 250 m show that these properties are improved over the entire observed record. Grey envelopes in (d,e,f) show observed monthly-mean \pm monthly-std values, with monthly values derived from the daily-mean values for each observed variable.

485

3.1.3 Canada Basin hydrography

486

487

488

489

490

491

492

493

494

495

496

Once the AW, via the West Spitsbergen Current, crosses the Fram Strait and traverses the Eastern Arctic along the continental slope (Rudels, 2015; Pnyushkov et al., 2018; Polyakov et al., 2017), the watermass properties (e.g., current strength and direction, density, temperature) are not as well constrained due extreme data paucity in the Eastern Arctic. In particular, along the boundary current path (shore-ward of the red contour in Fig. 8a), only 1% of the total 2004–2016 ITP data are acquired within the Nansen Basin; only 4.5% are acquired in the combined Amundsen and Makarov Basins. The majority of the ITP data (71%) are from within the Canada Basin. It is important to note that any bias may be relatively well-sampled here, but may result from weak sub-surface constraint throughout the entire eastern Arctic. Fig. 9 shows the reduction of misfits between the unconstrained *it0* and *ASTE_R1* as a function of basins and depths. The reduction is throughout the upper 800 m of the water column. Seawater density in

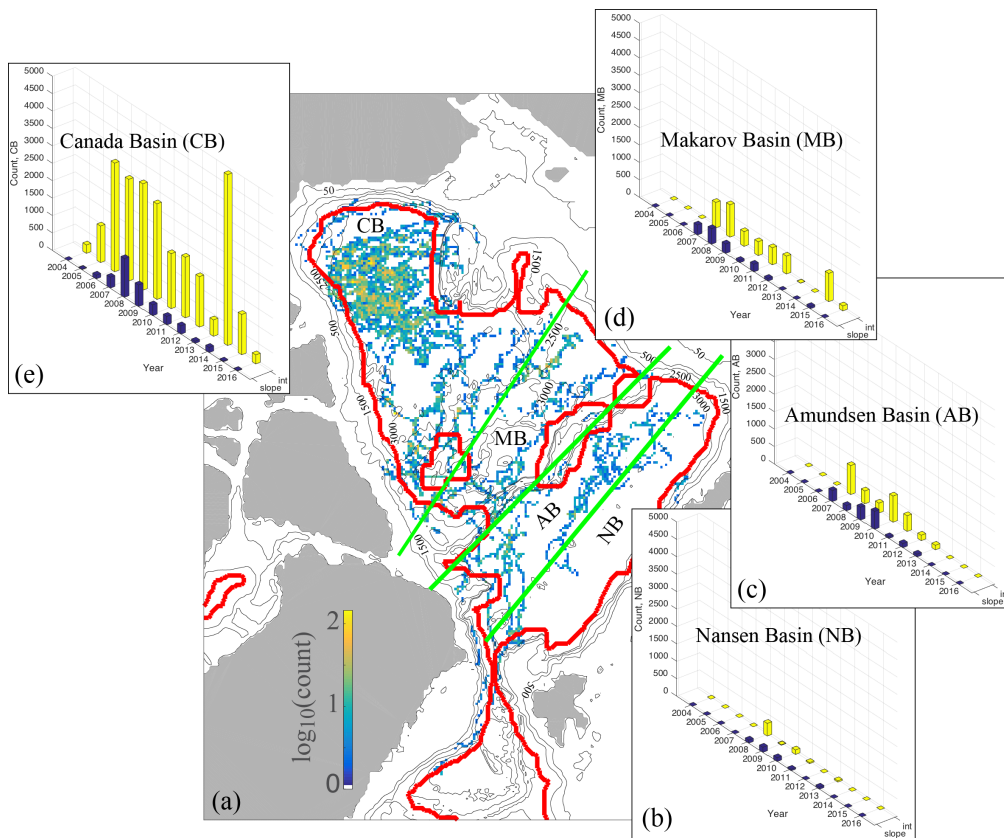


Figure 8. Distribution of ITP data as a function of year and geography. In (a), the red contour serves as a proxy for the separation between the continental shelf/slope (slope) and basin interior (int) regions. It is defined as ~ 100 km offshore of the 300 m depth contour. The thick green lines approximately separate the Nansen Basin (NB), Amundsen Basin (AB), Makarov Basin (MB) and Canada Basin (CB). In (b)–(e), histograms of the number of ITP profiles for the continental shelf/slope (dark blue) and Arctic interior (yellow) are normalized by the maximum number available for the Canada Basin (5000). There are a total of 39,904 ITP profiles.

497

498

499

500

the Arctic is primarily controlled by salinity, whereas temperature behaves more like a passive tracer and can be more flexibly impacted by the optimization procedure. As a result, the reduction in *ASTE_R1* temperature misfits greatly exceeds the reduction in

501 salinity misfits in the Arctic. For salinity, the highest remaining misfits in *ASTE_R1* are
 502 at depths occupied by the mixed layer and halocline (Fig. 9e–f).

503 Fig. 10 shows an example of how temperature misfits are reduced in the water column
 504 for ITP #55 whose trajectory began in the Canada Basin interior (red circle in Fig. 10a)
 505 and ended at the slopes of the Chukchi Plateau (green square). In the observations several
 506 watermasses can be seen, including the surface cold layer above ~ 30 m, warm Pacific
 507 Summer Water (PSW) at ~ 40 – 100 m, Cold Halocline Waters at ~ 110 – 250 m, and
 508 the Atlantic Water core at depths ~ 300 – 750 m (Fig. 10b). In the unconstrained *it0*, both
 509 the AW boundary current and the halocline are too warm, the AW layer is too thick,
 510 and the PSW is too cold. In *ASTE_R1*, closer consistency is obtained with tempera-
 511 ture observations for all watermasses. We emphasize that we have not applied direct ad-
 512 justments to the time-varying ocean hydrography to achieve this fit. Instead, it is through
 513 adjustments of the control variables, i.e., the initial hydrography in 2002, time-averaged
 514 internal mixing parameters, and surface atmospheric forcing. As a result, a “near-perfect”
 515 fit, such as that of the WOA18 hydrography to the mean ITP data seen in Fig. 1, is not
 516 possible for this under-determined problem. The fit is, nevertheless, within the speci-
 517 fied temperature and salinity uncertainties, with improved watermass representation for
 518 all ITP data (e.g., Fig. 10), Beaufort Gyre Moorings, NABOS moorings, and Fram Strait
 519 moorings.

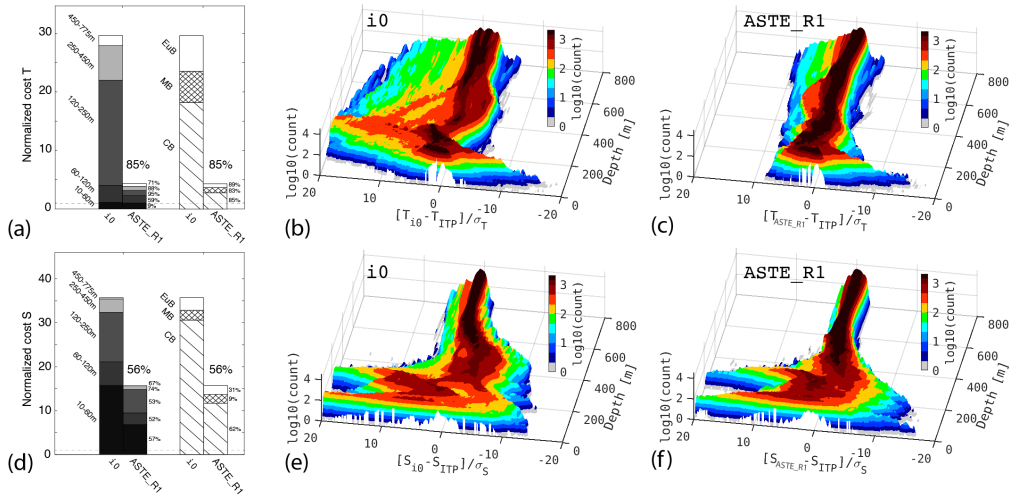


Figure 9. Normalized cost for ITP (a–c) temperature and (d–f) salinity. Costs to all ITP data are grouped by depth range and basin in (a) and (d). For the Canada Basin, histograms as a function of depths (b–c, e–f) show a narrowing of the misfit distributions for both temperature and salinity, especially in the AW layer below 250 m.

520

521 3.2 The Greenland Iceland Norwegian Seas

522 The Greenland-Iceland-Norwegian (GIN) Seas are defined here as bounded to the
 523 south by the the Greenland-Scotland Ridge (GSR) and to the north and north east by
 524 the Barents Sea Opening and the Fram Strait, respectively (see Fig. 11b). The sea ice
 525 near Fram Strait and along the East Greenland coast is seasonal and the largest mis-
 526 fits in *it0* were due to excessive ice here, including the Odden ice tongue (Wadhams et
 527 al., 1996) reaching further to the east during winter months (Fig. 6c–d and Fig. 11a).
 528 Surface winds and air temperature have been found to play an important role in con-

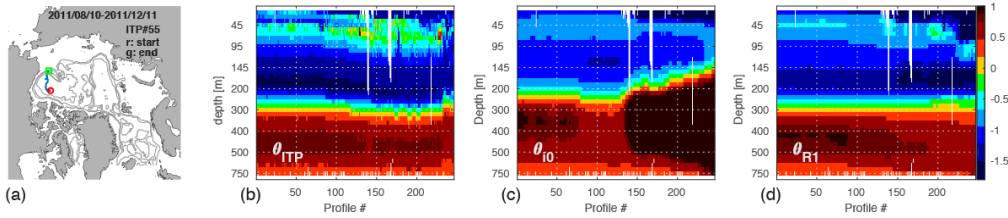


Figure 10. ITP #55 (a) trajectory, (b) potential temperature θ for all observed profiles along the trajectory, and the model equivalent for (c) *it0* and (d) *ASTE_R1*. In (a), the red circle and green square mark the first and last profile positions.

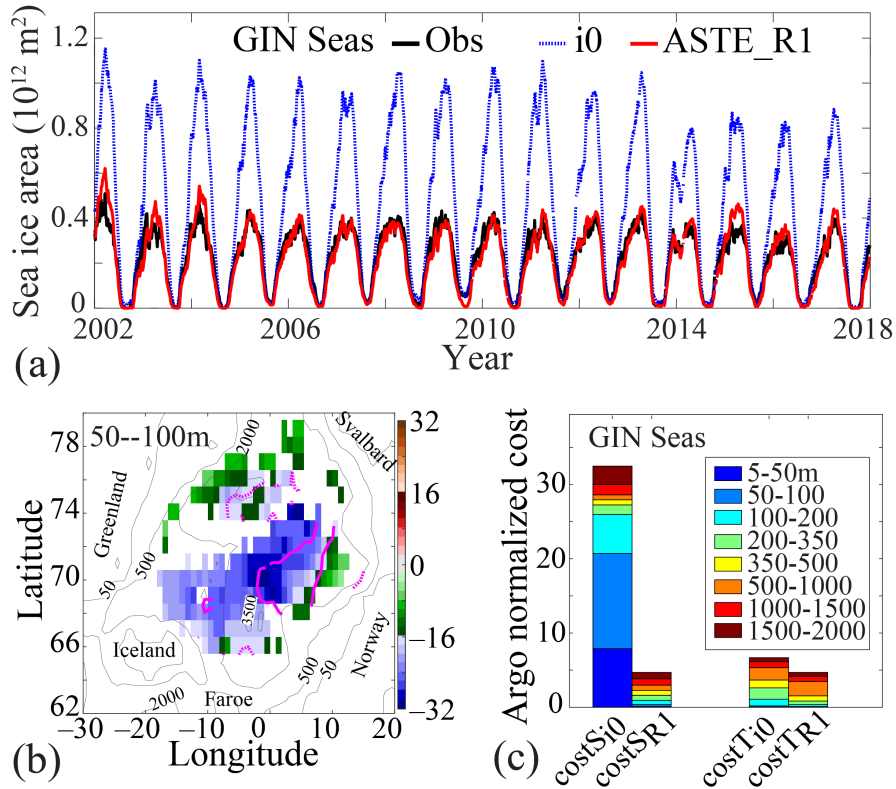


Figure 11. Improvements in GIN Seas sea ice and hydrography in *ASTE_R1* compared to *it0*. (a) Time-series of sea ice area for OSSISaf observations (black), *it0* (blue) and *ASTE_R1* (red). (b) Normalized misfits in salinity at depths 50–100m, defined as $(S_m - S_o)/\sigma_S$ where “m” and “o” are model and observed Argo, for *it0* in the GIN Seas (color scale, unitless). The magenta solid and dashed contours indicate *ASTE_R1* normalized misfits of magnitude ± 4 and ± 1 ; overlaying the contours on top of the colorscale thus show the misfits decrease from magnitudes 16–32 in *it0* to 1–4 in *ASTE_R1*. The breakdown of cost reductions for all other depth ranges are shown in (c) for the GIN Seas, with overall reductions of costs of 81% and 19% in salinity and temperature relative to Argo data.

529 trolling the eastern extent of the ice edge in this region (Germe et al., 2011; Moore et
 530 al., 2014). Adjustments of these atmospheric forcing variables during the optimization,
 531 within their specified uncertainties, drove a reduction in sea ice area (Fig. 11a) to im-
 532 prove the model-data fit.

533 The Nordic Seas host the interaction of several important watermasses. Warm and
 534 salty Atlantic water enters across the GSR along three major branches, meeting locally
 535 modified water recirculating in the Lofoten, Greenland and Iceland Basins, and the south-
 536 ward flowing cold, fresh East Greenland Coastal Current (Hansen & Østerhus, 2000).
 537 This region is characterized by very weak stratification, resulting in a very small defor-
 538 mation radius of 4–7 km throughout the region (Nurser & Bacon, 2014) which further
 539 challenges realistic representation of watermass distribution in models (Drange et al., 2005;
 540 Heuzé & Årthun, 2019) and *ASTE_R1*. Nevertheless, the improvements obtained in *ASTE_R1*
 541 are significant, with overall reductions of $\sim 85\%$ and 30% for salinity and temperature
 542 costs, respectively, through the 2000 m water column (Fig. 11c). The largest improve-
 543 ments are associated with reduction of a fresh bias in the upper 100 m (Fig. 11b–c), across
 544 the Lofoten, Iceland, and Greenland basins, which are important regions for deep wa-
 545 ter formation.

546 3.3 The Subpolar Gyre and North Atlantic

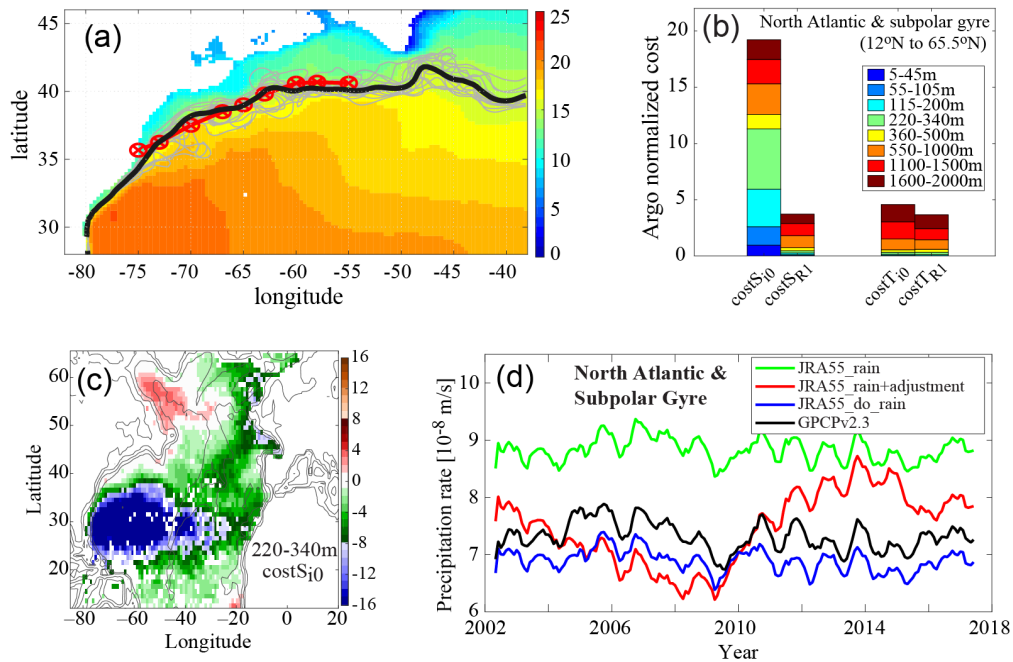


Figure 12. (a) The 2002–2017 mean proxy path of the Gulf Stream in *ASTE_R1* (black) and the World Ocean Atlas 2009 mean 15°C isotherm at 200 m depth (red, Wolfe et al. (2019)). The gray lines are the paths in *ASTE_R1* for all the years. (b) Normalized cost for salinity and temperature in the North Atlantic and subpolar gyre region (latitudes 12°N – 65.5°N) for *it0* and *ASTE_R1* as a function of depth range. (c) Normalized misfits in *it0* (relative to observed Argo salinity) in the water column at depth range 220–340 m. (d) Net precipitation into the North Atlantic and subpolar Gyre from JRA55 (Kobayashi et al., 2015), JRA55-do (Tsujino et al., 2018), observational based product GPCPv2.3 (Adler et al., 2018), and adjusted rain used to force *ASTE_R1*.

547 Although the primary focus of the study is on the assessment of *ASTE_R1* in the
 548 Arctic Mediterranean, the North Atlantic ocean serves as both the source of near sur-
 549 face heat and salt to the Arctic and the sink of dense deep water and surface freshwa-
 550 ter from the Arctic Mediterranean, and so will be briefly assessed here.

551 One of the greatest challenges in modeling the North Atlantic is to correctly simu-
 552 late the observed Gulf Stream pathway. Capturing a realistic Gulf Stream separation
 553 is non-trivial in z -level numerical models (Ezer, 2016; Chassignet & Xu, 2017). In *ASTE*,
 554 a combination of coastal biharmonic and off-shore Leith viscosity as described in Sec-
 555 tion 2.1 was used to achieve an observationally-consistent mean Florida Strait transport
 556 of $\approx 32 Sv$ (Baringer & Larsen, 2001; Johns et al., 2002) and a separation near Cape
 557 Hatteras. After separation, the Gulf Stream path can be approximately tracked using
 558 a proxy of the 15°C isotherm at 200 m depth (from the WOA13, Wolfe et al., 2019). Fig. 12a
 559 shows this proxy of the Gulf Stream path for the years 2002–2017 in *ASTE_R1* compared
 560 to that derived from WOA13.

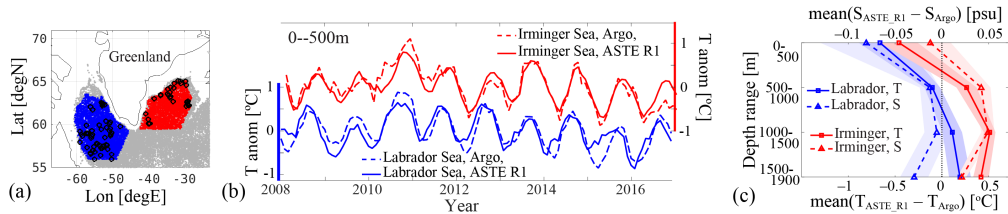


Figure 13. (a) Distribution of Argo data in the Irminger Sea (red dots) and Labrador Sea (blue dots) for the full period 2002–2017. To provide an impression of temporal coverage, black circles show data acquired within the month of January 2016. (b) Upper 500 m ocean mean temperature anomalies for the Labrador Sea (blue) and Irminger Sea (red) from Argo observations (dashed) and *ASTE_R1*. Anomalies are defined as the full time-series minus its respective mean, showing that *ASTE_R1* captures both the seasonal and interannual ocean temperature variability in both the Irminger and Labrador Seas. The biases are shown in (c) for temperature and salinity at various depth ranges sampled by Argo.

561 The dynamical mechanisms underlying the transports of warm AW from the Gulf
 562 Stream extension to the subpolar North Atlantic (SPNA) and into the GIN Seas across
 563 the GSR is poorly understood and its representation in state-of-the-art models remains
 564 a great challenge (Heuzé & Årthun, 2019). Compared with Argo data, the eastern SPNA
 565 hydrography (south of the GSR) contains large biases in $it0$ (Fig. 12b–c) but is signif-
 566 icantly improved in *ASTE_R1*, with a net reduction of misfit over the entire North At-
 567 lantic (north of 12°N) of $\sim 80\%$ and $\sim 21\%$ in salinity and temperature, respectively (Fig. 12b).
 568 Closer inspection reveals that, just south of the GSR, in the Irminger and Labrador Seas,
 569 *ASTE_R1* can reliably reproduce the observed hydrographic variability (Fig. 13a–b). How-
 570 ever, the solution exhibits a systematic warm (0.1 – 0.7°C) and salty (0.01 – 0.08 psu) bias
 571 throughout the upper 2000 m (Fig. 13c).

572 In the subtropical North Atlantic, a large fraction of the salinity misfit in $it0$ is due
 573 to excess freshwater flux from the atmosphere. Comparison to the Global Precipitation
 574 climatology Project version 2.3 product (GPCPv2.3, Adler et al., 2018) reveals an ex-
 575 cess precipitation bias in JRA-55, that is most pronounced in the North Atlantic and
 576 subpolar gyre region of the *ASTE* domain (Fig. 12d), and that resulted in a large fresh
 577 bias in the upper ~ 500 m of the unconstrained $it0$ solution (Fig. 12c). The adjoint-based
 578 optimization provided a systematic approach for removing this excess precipitation bias,

579 such that after approximately 12 iterations the misfits to Argo salinity in the upper ocean
 580 reduced to within the observed uncertainty (Fig. 12c).

581 4 Transports through Key Oceanic Gateways and Regional Storage

582 Here we summarize the volume, heat, and freshwater transports across important
 583 Arctic and GIN Seas gateways (Table 4, Fig. 14–16) and provide comparison to all known
 584 observation-based estimates (Skagseth et al., 2008; Schauer & Beszczynska-Möller, 2009;
 585 de Steur et al., 2009; Beszczynska-Möller et al., 2011; Curry et al., 2011, 2014; Hansen
 586 et al., 2015; Woodgate, 2018; Rosaby et al., 2018; Østerhus et al., 2019). Where avail-
 587 able, we also assess *ASTER1* transports against previously published estimates from
 588 coordinated modeling studies (Q. Wang et al., 2016b, 2016a; Ilicak et al., 2016; Heuzé
 589 & Årthun, 2019), ocean reanalyses (Uotila et al., 2019), and an independent inverse esti-
 590 mate (Tsubouchi et al., 2018).

591 The published literature offers notable differences in tracer reference values employed
 592 in the computation of reported heat, freshwater and volumetric watermass fluxes. These
 593 range from regional basin means (Smedsrud et al., 2010; Beszczynska-Möller et al., 2012;
 594 de Steur et al., 2018; Tesdal & Haine, 2020) to gateway and surface means (Tsubouchi
 595 et al., 2018) to freezing temperature in the Arctic (Beszczynska-Möller et al., 2012; Woodgate,
 596 2018). In some cases, transports were computed along a particular range of isopycnals
 597 (Tsubouchi et al., 2018). Heat transport computed in *ASTER1* assumes a reference tem-
 598 perature $\theta_r = 0^\circ\text{C}$ (most accurate numerically, see Appendix B). For the Bering Strait,
 599 we also compute heat transport referenced to the freezing temperature of seawater $\theta_r =$
 600 -1.9°C to facilitate comparison with published estimates. For the computation of fresh-
 601 water transports, we assume a reference salinity $S_r = 34.8$ psu and integrate from the
 602 surface down to the reference isohaline. We refer the reader to Appendix B for details
 603 on potential errors incurred when computing transports using non-zero reference values.
 604 Due to the difference in reference values employed here and in some of the studies listed
 605 above, we seek consistency in terms of comparable transport magnitudes as opposed to
 606 exact agreement.

607 To provide a useful comparison of *ASTER1* mean transports with those reported
 608 in the literature, it is important to note whether published estimates are based on his-
 609 toric data or more recent acquisitions, given how fast the high latitudes are observed to
 610 be changing. In the first four years of the *ASTER1* period, 2002–2005, transports in
 611 both the North Atlantic and the Arctic exhibit distinctly different characteristics com-
 612 pared to the period 2006–2017. This transition of hydrographic properties and circula-
 613 tion patterns around 2005–2006 has been extensively discussed, with studies noting a
 614 strong increase in volume and heat transports into the Barents Sea (Skagseth et al., 2008),
 615 increased salinity and density in the lower halocline in the Eastern Arctic (Dmitrenko
 616 et al., 2011), abrupt changes in North Atlantic heat (Piecuch et al., 2017; Foukal & Lozier,
 617 2018) and freshwater (Dukhovskoy et al., 2019) content, and rapid freshening of the Nordic
 618 Seas (Tesdal & Haine, 2020). To avoid averaging over these two apparently distinct regimes,
 619 we chose to report all mean transports for the most recent period, following the abrupt
 620 transition. Reported associated standard deviations to the 2006–2017 mean transports
 621 are computed based on the monthly values after the seasonal cycle has been removed.
 622 Details of the calculation of *ASTER1* transports are given in Appendix B, and water-
 623 mass definitions are given in Appendix C.

624 4.1 Volume Transports

625 Østerhus et al. (2019) summarized existing estimates of volume transports across
 626 all the important Arctic–Nordic Seas gateways including the Bering Strait (BS), Davis
 627 Strait (DaS), and the Greenland-Scotland Ridge (GSR). The latter comprises the Den-
 628 mark Strait (DS), Iceland-Faroe channel (IF) and Faroe-Shetland channel (FSh). Time-

<i>Transports</i>				
Gate	Volume [Sv]	Heat [TW]	FW [mSv]	
(1)Bering Strait	1.11 ± 0.35	4.70 ± 7.25	54.24 ± 20.62	
(2)CAA	-1.72 ± 0.39	7.95 ± 2.99	-94.19 ± 31.60	
(3)Fram Strait	-1.50 ± 0.66	54.15 ± 13.24	-84.83 ± 23.29	
(4)Svalbard-FJL ¹ -SZ ²	2.04 ± 0.64	-0.85 ± 8.03	45.23 ± 31.14	
(5)Barents Sea Opening	1.98 ± 0.66	62.33 ± 15.06	-3.25 ± 3.30	
(6)Davis Strait	-1.72 ± 0.39	25.40 ± 4.71	-103.32 ± 19.59	
(7)Denmark Strait	-2.00 ± 0.76	11.92 ± 7.81	-42.61 ± 12.21	
(8)Iceland-Faroe	2.26 ± 0.90	119.11 ± 24.09	-0.29 ± 0.69	
(9)Faroe-Shetland	0.71 ± 1.30	95.00 ± 38.12	6.25 ± 4.29	
(10)Newfoundland-Gr	-1.74 ± 0.38	67.30 ± 17.41	-110.67 ± 23.44	
(11)48.3°N	-1.39 ± 0.36	449.66 ± 75.75	-111.60 ± 22.80	

<i>Heat Budget [TW]</i>				
<i>Domain</i>	Lateral conv	Vertical conv	Tendency	Bounded Gates
Arctic	65.95 ± 13.57	-39.53 ± 39.48	26.39 ± 41.34	1,2,3,4
CAA	17.46 ± 5.84	-18.08 ± 12.55	-0.63 ± 15.60	2,6
Barents	63.18 ± 19.94	-63.63 ± 37.27	-0.45 ± 47.98	4,5
GINs	109.55 ± 34.28	-110.06 ± 60.55	2.19 ± 78.36	3,5,7,8,9
Labrador Sea	41.90 ± 16.81	-49.40 ± 39.83	-7.50 ± 47.30	6,10
East SPNA	156.33 ± 96.91	-146.97 ± 92.94	6.65 ± 165.61	7,8,9,10,11

<i>FW Budget [mSv]</i>				
<i>Domain</i>	Lateral conv	Vertical conv ^a	Tendency	Bounded Gates
Arctic	-79.55 ± 40.31	74.57 ± 10.28	-9.45 ± 35.83	1,2,3,4
CAA	-9.13 ± 26.29	5.78 ± 2.86	-0.51 ± 22.68	2,6
Barents	-48.48 ± 30.96	57.54 ± 7.89	-4.17 ± 30.29	4,5
GINs	51.43 ± 23.16	34.52 ± 17.74	1.20 ± 16.89	3,5,7,8,9
Labrador Sea	-7.35 ± 23.15	20.55 ± 9.58	4.56 ± 22.35	6,10
East SPNA	35.72 ± 16.92	93.94 ± 26.42	2.41 ± 20.32	7,8,9,10,11

Table 4. *ASTE_RI* budgets of volume, heat ($\theta_r = 0^\circ\text{C}$), and FW ($S_r = 34.8\text{psu}$) for the combined ocean and ice system for the period 2006–2017. Standard deviation are computed from monthly mean values after the seasonal cycle has been removed. FW transport is computed using Eqn B3.2 from Appendix B. ^aThe vertical convergence of FW, from air-ice-sea fluxes, is the same as that for volume and is exact. Lateral convergence and tendency of FW, however, are approximate. As a result, the budget for FW is not fully closed (see Appendix B). ¹ Franz Josef Land, ² Severnaya Zemlya.

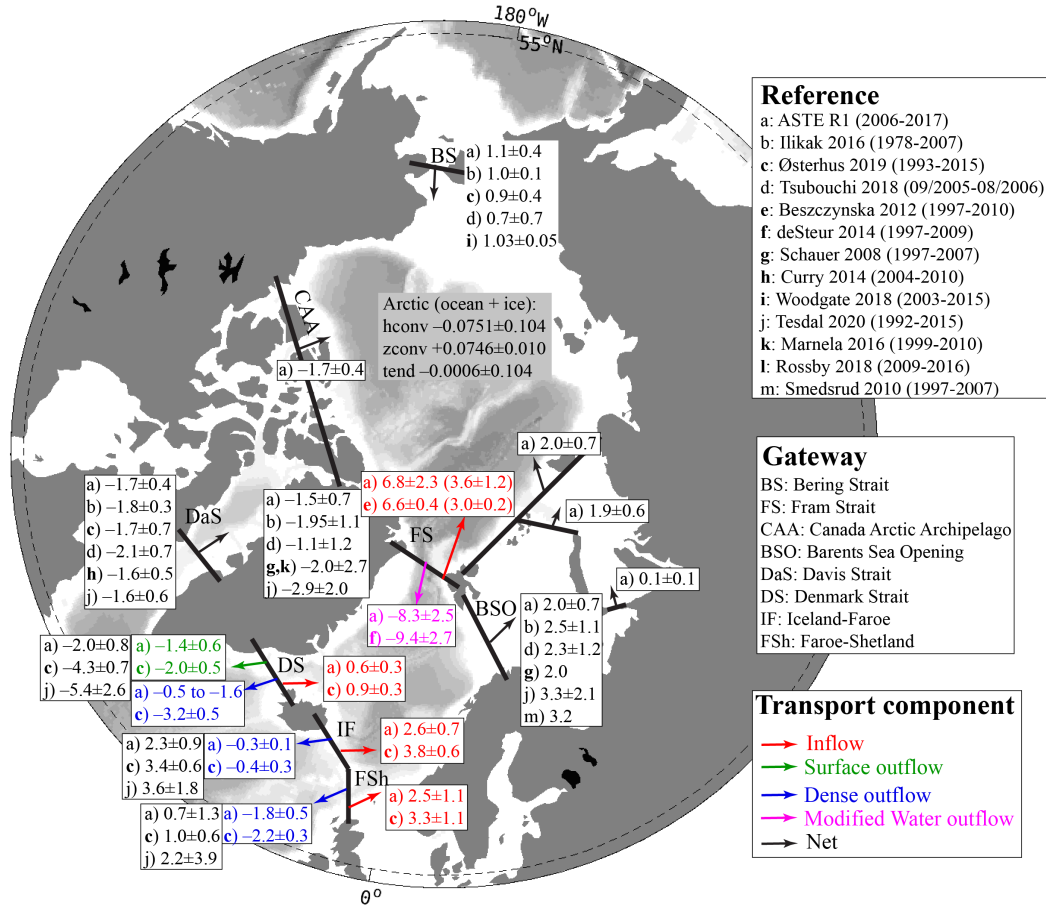


Figure 14. Volume transports across important Arctic and Nordic Seas gateways listed for (a) *ASTER1* and (b-m) published estimates referenced in the legend. Net transports across the full width and depth of each section are written in black; transport component contributions to this total are written in color for (red) total inflow, (green) surface outflow, (blue) dense outflow, and (magenta) modified water outflow, where arrows show the direction ascribed to in/outflow. Positive (negative) transport indicates Northward and Eastward (Southward and Westward). Quantities listed are 2006–2017 mean and standard deviation after the seasonal cycle has been removed. All net transports in *ASTER1* are diagnosed online, while separate transport components through FS, DS, IF, and FSh are diagnosed offline using archived monthly advection terms. See text and Appendix C for further discussion on watermass identification used in determining the in/outflow transport components. For the Fram Strait inflow, the two provided estimates are for the West Spitsbergen current only, and we give both the total current transport and, in parenthesis, the fraction above 2°C (Beszczynska-Möller et al., 2011). Numbers in parenthesis in Reference legend refer to the period covered by the respective studies.

629 mean values of these transports in *ASTER1* are given in Table 4 and Fig. 14, listed along-
 630 side previously published estimates from observations (Beszczynska-Möller et al., 2012;
 631 de Steur et al., 2014; Beszczynska-Möller et al., 2011; Woodgate, 2018; Curry et al., 2014;
 632 Skagseth et al., 2008; Hansen et al., 2015), and modeling studies (Tsubouchi et al., 2018;
 633 Heuzé & Årthun, 2019; Ilicak et al., 2016). In addition to net transports, we also pro-
 634 vide estimates of transports of important watermasses at Fram Strait (as defined in Beszczynska-
 635 Möller et al., 2011) and through the GSR (as defined in Hansen & Østerhus, 2000; Øster-
 636 hus et al., 2019). For the in/outflow transport estimates given in Fig. 14, we follow wa-
 637 termass definitions of Beszczynska-Möller et al. (2012) for the Fram Strait and Østerhus
 638 et al. (2019) for the GSR.

639 The net volume transport across the Bering Strait is northward into the Arctic and
 640 approximately 1.1 ± 0.4 Sv. Across the Davis Strait, there is a southward transport of
 641 freshwater near the surface and northward transport of warm water from the Irminger
 642 Current (Curry et al., 2014). At this gate, *ASTER1* estimates a net volume transport
 643 of 1.7 ± 0.4 Sv, consistent with observed values of 1.6 ± 0.5 and 1.7 ± 0.7 from Curry
 644 et al. (2014) and Østerhus et al. (2019). Across the GSR, there is a net near-surface north-
 645 ward transport of AW across the Denmark Strait (DS), Iceland-Faroe (IF) and Faroe-
 646 Shetland (FSh) channels (shown in red in Fig. 14), southward surface flow of freshwa-
 647 ter across DS and dense overflow across the entire ridge (green and blue color in Fig. 14).

648 Watermass definitions for surface outflow, dense outflow, modified water, and in-
 649 flow AW in *ASTER1* can differ from Østerhus et al. (2019) and Hansen and Østerhus
 650 (2000) for the reasons outlined in Section 2.3. Our choice for σ_θ is justified in Appendix
 651 C. For the overflow through DS, the range of $27.4 \leq \sigma_\theta \leq 27.8$ used in *ASTER1* is
 652 associated with southward transports of -1.6 ± 0.9 to -0.5 ± 0.3 Sv (shown in blue
 653 in Fig. 14), corresponding to 16%–50% of the observed estimate using $\sigma_\theta = 27.8$ from
 654 Østerhus et al. (2019). Similar considerations for σ_θ of dense overflow water across the
 655 IF and FSh ridges (Appendix C) yield -0.3 ± 0.1 Sv and -1.8 ± 0.5 Sv, respectively,
 656 in *ASTER1*, compared to -0.4 ± 0.3 Sv and -2.2 ± 0.3 Sv of water with $\sigma_\theta \geq 27.8$
 657 in Østerhus et al. (2019). For surface outflow, *ASTER1* underestimates the observed
 658 estimate at the DS by approximately 30%. In total, the net volume transport across DS
 659 in *ASTER1* is about 47% of that reported by Østerhus et al. (2019).

660 For the Arctic Ocean and GIN Seas heat and freshwater budgets, transports through
 661 the Fram Strait (FS) and the Barents Sea Opening (BSO) are also important. Across
 662 the FS, the inflow of warm AW along the West Spitsbergen Current (red color in Fig. 14)
 663 is 6 ± 1 Sv in *ASTER1*, with 3.4 ± 1.1 Sv carrying the core AW water warmer than
 664 2°C . This is consistent with corresponding estimates of 6.6 ± 0.4 and 3.0 ± 0.2 from
 665 Beszczynska-Möller et al. (2012) based on observations from an earlier period of 1997–
 666 2010. The outflow across FS includes freshwater carried by the East Greenland Current
 667 at the surface and return of modified AW at depth (magenta color in Fig. 14, Beszczynska-
 668 Möller et al., 2011). For the southward return of modified AW, *ASTER1* estimates a
 669 flux of of -8.3 ± 2.5 Sv over the period 2006–2017, consistent with -9.4 ± 2.7 Sv from
 670 de Steur et al. (2014) for the period 1997–2009. Across the BSO, volume transport is
 671 dominated by the eastward Norwegian Coastal Current and the Atlantic inflow which
 672 carries warm AW into the Barents Sea (Smedsrud et al., 2010). The net eastward vol-
 673 ume transport in *ASTER1* of 2.0 ± 0.7 Sv is consistent with observation-based esti-
 674 mate of ~ 2.0 Sv from Smedsrud et al. (2010).

675 4.2 Heat Transports

676 All *ASTER1* net heat transports are poleward from lower latitudes into the Arc-
 677 tic Mediterranean and further north into the Arctic Basin. We find that time-mean pole-
 678 ward transports across key gateways are consistent with observation-based estimates,

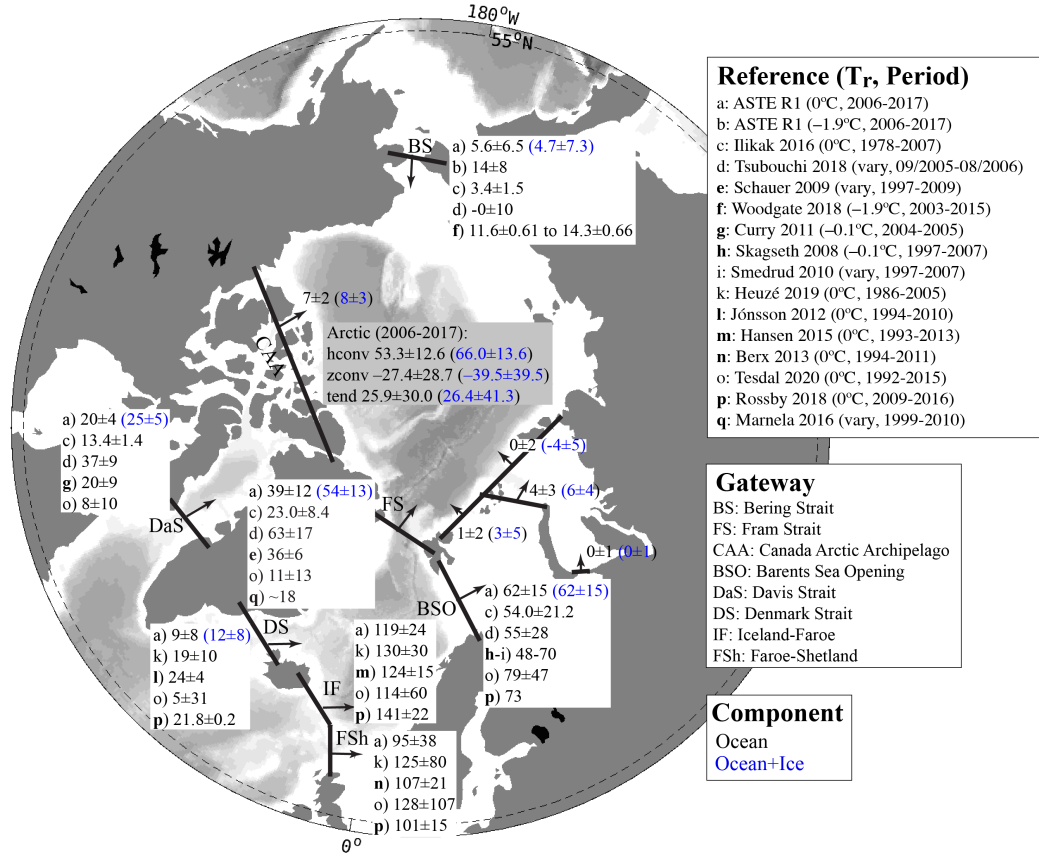


Figure 15. As for Fig. 14 but showing net ocean heat transport across important Arctic and Nordic Seas gateways. For select gateways the combined ocean+ice heat transport is also given (in blue). *ASTER1* transports (listed under (a)) are computed assuming a reference temperature $T_r=0^\circ\text{C}$. For the Bering Strait we also provide *ASTER1* transports computed using $T_r=-1.9^\circ\text{C}$ (listed under (b)). Since previously published estimates (c-q) vary in their choice of T_r (see main text) we assess agreement between estimates as consistency in order of magnitude. Positive (negative) transport indicates Northward and Eastward (Southward and Westward) flow. Quantities listed are 2006–2017 mean and standard deviation after the seasonal cycle has been removed. Numbers in parenthesis in Reference legend refer to the T_r used and the period covered by the respective studies.

679 a result that is aided – although by no means guaranteed – by constraining the state estimate using mooring T/S data (Table 4, Fig. 15).
680

681 At the Bering Strait *ASTER1* poleward heat transport is 14 ± 8 TW (referenced
682 to $T_r=-1.9^\circ\text{C}$), consistent with the 11.6 TW to 14.3 TW range determined by Woodgate
683 (2018). At Davis Strait, the *ASTER1* estimate of 20 ± 4 TW is consistent with $20 \pm$
684 9 TW obtained by Curry et al. (2011). Across the DSR, heat transports are in good agree-
685 ment with previous published estimates across the two eastern channels (IF and FS, Fig. 15),
686 but is underestimated across the Denmark Strait. Here, the total poleward diffusive heat
687 flux dominates and opposes the equatorward advective term in *ASTER1*. This diffu-
688 sive dominance has also been suggested using heat budget analyses in ECCOV4 (Buckley
689 et al., 2015). A more detailed discussion of the full time-series and contributions of ad-
690 vective and diffusive fluxes to the total transport is given in Appendix B.

691 Further north, at the Fram Strait, *ASTE_R1* poleward heat transport is 39 ± 12 TW
 692 (referenced to $T_r=0^\circ\text{C}$), consistent with 36 ± 6 TW from Schauer and Beszczynska-Möller
 693 (2009) and Beszczynska-Möller et al. (2011). The Fram Strait heat flux is increased by
 694 approximately one third (15 TW) on accounting for sea ice advection. Heat transport
 695 into the Barents Sea across BSO of 62 ± 15 TW is consistent with observation-based
 696 estimates of between 48 TW and 73 TW (Skagseth et al., 2008; Smedsrud et al., 2010;
 697 Rossby et al., 2018). Most of this heat is lost via air-sea exchange in the Barents and
 698 Kara Seas (Lind et al., 2018), yielding negligible heat transports from this shallow re-
 699 gion into the Arctic Basin (Fig. 15). Air-sea exchange also accounts for significant loss
 700 of heat in the Canadian Arctic Archipelago, such that only $\sim 35\%$ of the amount trans-
 701 ported across the Davis Strait reaches the Arctic Basin.

702 We note that there is a large spread amongst existing observation- and model-based
 703 studies with significant disagreements even after accounting for uncertainty (Fig. 15),
 704 due in part to the lack of common data period and reference temperature used in the
 705 calculations. Overall, nevertheless, the poleward heat transports in *ASTE_R1* are in good
 706 agreement with previous estimates (Fig. 15).

707 4.3 Freshwater Transports

708 The practice of reporting ocean freshwater (FW) transport/content in place of ab-
 709 solute salt transport/content is ubiquitous in the literature, but plagued by the need to
 710 specify a reference salinity, S_r and choose the vertical extent over which the integral is
 711 computed (i.e., full depth versus to the depth of the reference salinity z_{S_r}). No unique
 712 choice emerges from consideration of seawater physics. Instead, S_r is selected inconsis-
 713 tently between studies. As cautioned by Schauer and Losch (2019), this not only com-
 714 plicates comparisons but can give very different impressions of the changing ocean state,
 715 due to strong sensitivity to the choice of S_r . Acknowledging this issue, we neverthe-
 716 less elect to report FW transport below (as did (Tesdal & Haine, 2020) in their recent study
 717 focusing on the subpolar North Atlantic and Nordic Seas), in an attempt to continue our
 718 assessment of *ASTE_R1* hydrography in the context of existing estimates. To the best
 719 of our knowledge no published observational estimates report Arctic salt transports to
 720 provide a basis for comparison (the modeling study by Treguier et al., 2014 is one known
 721 exception). We proceed with caution and flag comparisons for which calculations differ.
 722 *ASTE_R1* FW fluxes are reported using a reference salinity of $S_r=34.8$ psu and integrated
 723 down to z_{S_r} . Our calculation uses monthly averages of both the Eulerian velocity and
 724 salinity. In Appendix B we provide a detailed discussion of the potential errors in FW
 725 calculations with these choices, along with errors incurred in omitting bolus and diffu-
 726 sive terms. Salt transport or salt content changes in *ASTE_R1* will be revisited in fu-
 727 ture work.

728 Similar to our assessment of volume and heat transports, we start by examining
 729 FW transports across the gates into the Arctic Mediterranean. At the Bering Strait, *ASTE_R1*
 730 combined liquid and solid FW import of 1711 ± 608 km³/yr is lower than the $2670 \pm$
 731 144 km³/yr estimated by Woodgate et al. (2015) and Woodgate (2018). At the Davis
 732 Strait, *ASTE_R1* liquid and solid FW exports of -2785 ± 530 km³/yr and -476 ± 182
 733 km³/yr are consistent with estimates of -2933 ± 189 km³/yr and -315 ± 32 km³/yr
 734 from Curry et al. (2014), on accounting for uncertainty/variability. There is negligible
 735 FW transports across the Iceland-Faroe and Faroe-Shetland channels. At the Denmark
 736 Strait, *ASTE_R1* estimate of -1112 ± 309 km³/yr is approximately half of the value
 737 reported by Marnela et al. (2016) of -2050 ± 347 km³/yr. This is consistent with the
 738 50% underestimation of both volume and heat transports in *ASTE_R1* across this gate
 739 compared to independent observations.

740 Further north at the Fram Strait, the liquid and solid FW exports of -1465 ± 463
 741 km³/yr and -1195 ± 394 km³/yr in *ASTE_R1* are lower than the -2050 ± 710 km³/yr

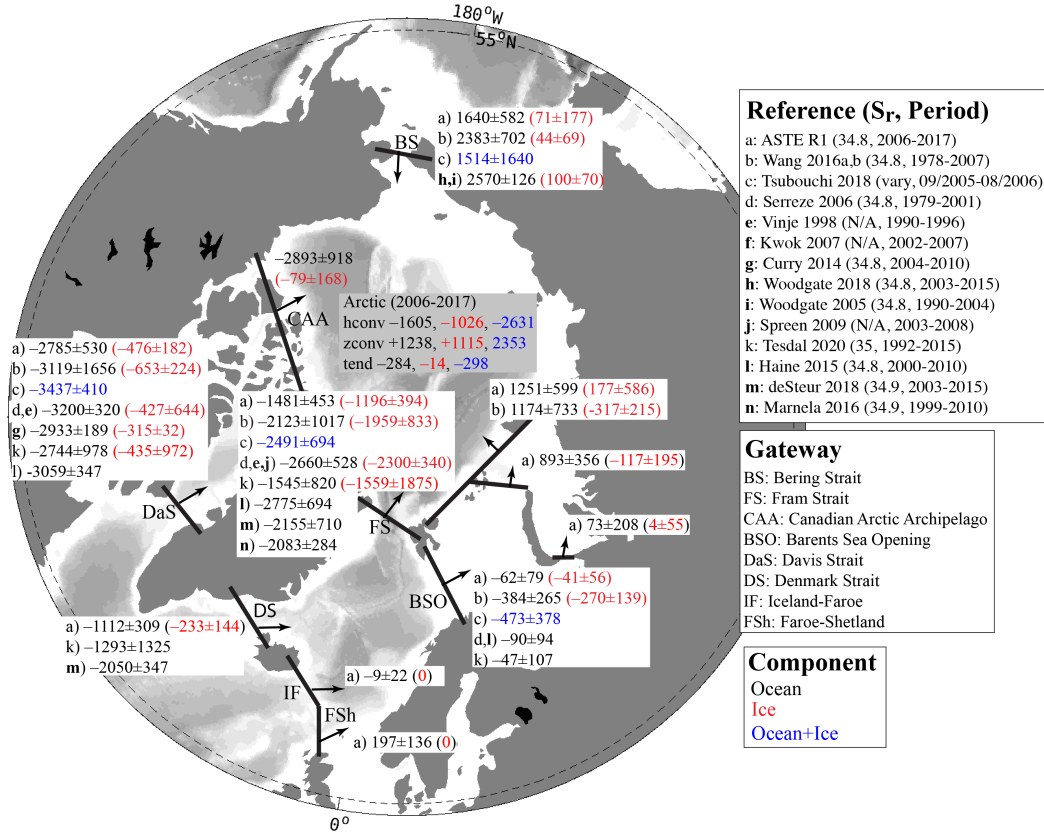


Figure 16. FW flux across important Arctic and Nordic Seas gateways from *ASTE_R1* and published estimates. Units are in $\text{km}^3 \text{ yr}^{-1}$. $S_r=34.8$ psu is used in *ASTE_R1* calculations for all FW transports and content/tendency terms for the ocean. A fixed salinity $S_i=4$ psu is used for sea ice transports and tendency terms. Positive (negative) values indicate Northward and Eastward (Southward and Westward) transports. Quantities listed are 2006–2017 mean and standard deviation after the seasonal cycle has been removed. Numbers in parenthesis in Reference legend refer to the S_r used and the period covered by the respective studies.

742 and $-2300 \pm 340 \text{ km}^3/\text{yr}$ estimated by de Steur et al. (2009) and Spreen et al. (2009).
 743 One main reason for the lower (by $\sim 1200 \text{ km}^3/\text{yr}$) liquid export in *ASTE_R1* across Fram
 744 Strait is the lower (by $\sim 960 \text{ km}^3/\text{yr}$) FW import through the Bering Strait relative to
 745 observations. An additional inconsistency is the use of a runoff climatology in *ASTE_R1*
 746 , which fails to account for Greenland solid/liquid discharge and its observed recent in-
 747 crease into the Arctic sector by approximately $105 \text{ km}^3/\text{yr}$ (Bamber et al., 2012), as well
 748 as increased river outputs (as reported in Bamber et al., 2012; Proshutinsky et al., 2020).
 749 With respect to the latter, *ASTE_R1* has a deficit of $\sim 220 \text{ km}^3/\text{yr}$. The climatology
 750 also does not account for Greenland solid and liquid discharge into the GIN Seas and
 751 Baffin Bay by nearly $150 \text{ km}^3/\text{yr}$ and $250 \text{ km}^3/\text{yr}$, respectively (Bamber et al., 2012).
 752 In the Canadian Arctic Archipelago, the product also has a FW flux deficit of $\sim 226 \text{ km}^3/\text{yr}$
 753 from land ice (Carmack et al., 2016). These omissions likely contribute to the underes-
 754 timation of southward FW transports across both the Denmark Strait (by $\sim 940 \text{ km}^3/\text{yr}$)
 755 and Davis Strait (by $\sim 150 \text{ km}^3/\text{yr}$).

756 The net lateral convergence of the combined liquid and solid freshwater flux in *ASTE_R1*
 757 of $-2510 \pm 1272 \text{ km}^3/\text{yr}$ is nearly balanced by the net vertical convergence of $2353 \pm$

758 324 km³/yr, yielding a net tendency of -298 ± 1131 km³/yr. For the liquid flux alone,
 759 the tendencies are -1484 ± 1123 , 1238 ± 2478 , and -284 ± 2169 km³/yr for lateral
 760 convergence, vertical convergence, and total tendency, respectively.

761 **4.4 Heat and Freshwater Storage**

762 The present assessment focuses on comparisons between *ASTE_R1* and existing es-
 763 timates. A full assessment of the mechanisms underlying Arctic Mediterranean and sub-
 764 polar North Atlantic heat and freshwater content change over the *ASTE_R1* period will
 765 be addressed in a separate study. As noted earlier, decisions made in our tracer trans-
 766 port/budget calculations facilitate these comparisons but are non-unique. For freshwa-
 767 ter transports/budgets this introduces ambiguity that is best resolved prior to detailed
 768 dynamical investigation. Here we summarize contributions to the time-mean heat and
 769 freshwater budgets and 2002–2017 trends.

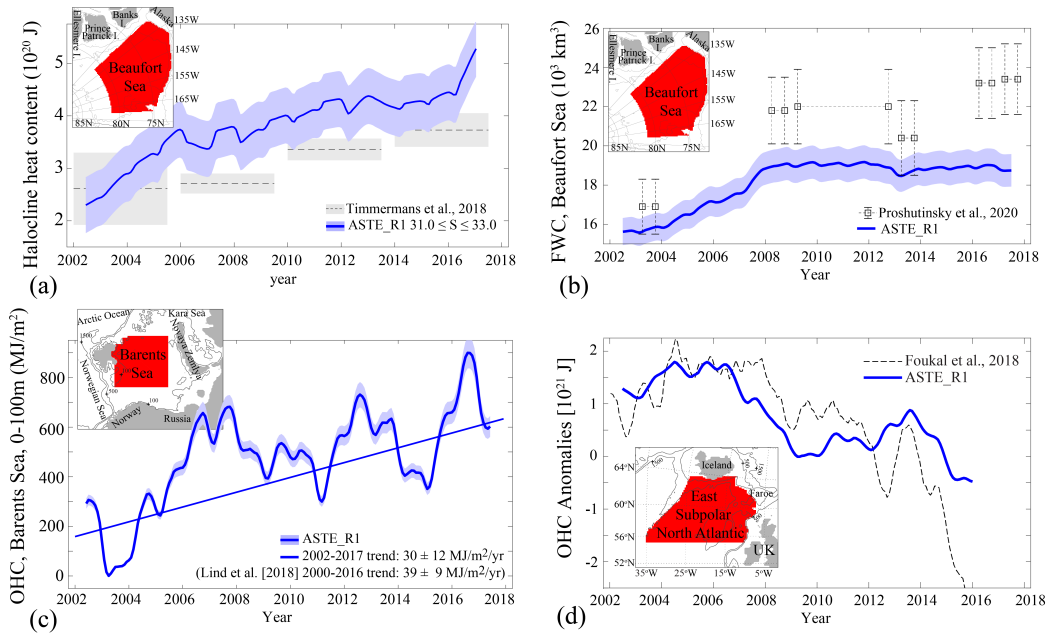


Figure 17. Comparison of *ASTE_R1* (a) Beaufort Sea halocline (defined as $31.0 \leq S \leq 33.0$) heat content, (b) Beaufort Sea freshwater content above the 34.8 psu isohaline, (c) Barents Sea 0–100m heat content and, (d) East Subpolar North Atlantic full-depth heat content with existing observational-based estimates, as given in the legend of each panel. Insets show the spatial mask defining each region. A 12-month running mean has been applied to filter the seasonal cycle from the *ASTE_R1* time-series, facilitating comparison with observed trends. Shading in *ASTE_R1* time-series indicate the sensitivity of the (a,c) heat content to a 5% change in (a) the northern and (c) eastern spatial mask, or the sensitivity of the (b) freshwater content to a 0.5 psu change in the lower limit employed in the halocline watermass definition (see Appendix C).

770 **4.4.1 Heat Content**

771 Considering the Arctic region of *ASTE_R1* in its entirety, the net heat input from
 772 convergence of horizontal (ocean plus ice) heat transports (53.3 ± 12.0 TW) exceeds
 773 the net heat loss due to local air-ice-sea fluxes (-27.4 ± 28.7 TW) by a factor ~ 2 , yield-
 774 ing a net heating rate of 25.9 ± 30.0 TW when averaged over the period 2006–2017 (Ta-

775 ble 4). Relative to horizontal convergence, vertical exchange at the air-ice-sea interface
 776 is significantly less well constrained due to large uncertainties in atmospheric reanaly-
 777 ses at high northern latitudes (Beesley et al., 2000; Chaudhuri et al., 2014; C. Wang et
 778 al., 2019). Partitioned by basins, similar enthalpy gains are estimated for both the west-
 779 ern (14.0 ± 24.3 TW) and eastern (12.5 ± 14.0 TW) Arctic region. In the water col-
 780 umn, heat gain is concentrated mainly in the AW layer (240–1000 m) in both the west-
 781 ern (9.3 ± 2.7 TW) and eastern (6.4 ± 4.6 TW) Arctic. In the upper 60 m of the wa-
 782 ter column, the tendency is negligible but with large variability (0.2 ± 25.3 TW) due
 783 to mixed layer processes and exchange with the atmosphere.

784 Warming since the early 2000s has been reported in the Arctic, documented along-
 785 side enhanced “Atlantification” in the Eastern Arctic (Polyakov et al., 2017, 2020) and
 786 a fivefold increase in solar absorption by near surface waters in the Western Arctic (Jackson
 787 et al., 2010; Timmermans et al., 2018). This warming proceeds at a sustained rate, with
 788 recent studies suggesting a doubling of OHC in the Beaufort Gyre halocline between 2003
 789 and 2013 (Timmermans et al., 2018).

790 Fig. 17a shows a comparison of the time-series of the halocline heat content in *ASTE_R1*
 791 and estimates based on ITP and mooring data in the Beaufort Sea. As discussed in Sec-
 792 tion 2.3, adopting exact watermass classifications from observational studies may be in-
 793 appropriate for model analysis, due to representation error of subgrid scales. Thus in ad-
 794 dition to the salinity limits used to identify the upper halocline layer of $31.0 \leq S \leq$
 795 33.0 in Timmermans et al. (2018), we also compute the heat content sensitivity to the
 796 salinity bounds. By changing the near-surface lower salinity bound within the range 31–
 797 31.5 psu, the mean halocline heat content changes by 2–3% per 0.1 psu increment, but
 798 the variability and trend remain unchanged. This confirms that despite the systematic
 799 warm bias, the positive trend in halocline heat content is well-captured in the *ASTE_R1*
 800 solution.

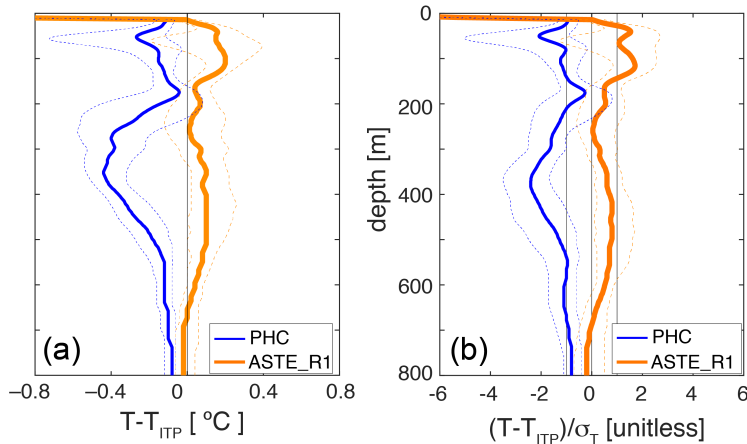


Figure 18. Comparison between all ITP-derived temperature profiles in the Canada Basin and PHC (blue) and *ASTE_R1* (orange). Panel (a) shows the normalized 50th percentile difference (dimensionless) and (b) the 50-percentile difference (°C). The two vertical black lines in (b) at ± 1 indicate the limits within which the difference is within the uncertainty σ_T . The dotted lines show the 30th and 70th percentile differences.

801 In the Canada Basin, *ASTE_R1* exhibits a warming rate of 9.3 ± 2.7 TW for the
 802 period 2006–2017 (Fig. 15). There are insufficient observations to validate this directly,
 803 but we can corroborate our estimate with a back of the envelope calculation as follows.

804 Recent ITP acquisitions report core AW temperatures in this region $\sim 0.5^\circ\text{C}$ warmer than
 805 the PHC climatology (Fig. 18a), where the latter is representative of the second half of
 806 the 20th century. Since ITPs only measure to ~ 800 m depth, we conservatively assume
 807 a depth-average warming of $0.20\text{--}0.25^\circ\text{C}$ over the $170\text{--}1000$ m range in the Western Arctic
 808 basin interior (area $4400 \times 10^3 \text{ km}^2$), yielding a warming rate of $\sim 5.7\text{--}7.2$ TW, about
 809 two thirds of the rate estimated in *ASTER1*. Compared to ITP data, *ASTER1* shows
 810 a positive bias of $\sim 0.15^\circ\text{C}$ in the core AW temperature in the Western Arctic basin, which
 811 accounts for the higher tendency here. However, we note that this *ASTER1* bias is within
 812 the combined data and representative error σ_T , which is not the case for the PHC bias
 813 (Fig. 18b).

814 The Eastern Arctic suffers from an even greater paucity of data, such that even back
 815 of the envelope estimates of basin-wide heat content (and its tendency) are not possi-
 816 ble. Instead, we turn to recent observations for evidence of warming in this basin. Pulsed
 817 injection of AW at the Fram Strait has been documented by Polyakov et al. (2011). A
 818 notable pulse generated a warm anomaly of $\sim 1^\circ\text{C}$, which entered the Arctic in 2004 and
 819 has subsequently been observed crossing the NABOS section at 126°E , and recorded fur-
 820 ther downstream at numerous sections along the eastern basin's rim (Polyakov et al., 2011).
 821 In addition, the seasonal amplitude within the halocline has been observed to increase
 822 by 0.75°C between 2004 and 2015 (Dmitrenko et al., 2009; Polyakov et al., 2017; Bau-
 823 mann et al., 2018). These observations provide evidence for a warming Eastern Arctic
 824 and a weakened halocline. The latter is accompanied by shoaling of the AW layer to-
 825 ward the bottom of the mixed layer and increasing heat ventilation (Polyakov et al., 2020).
 826 This is a mechanism by which heat along the AW pathway is removed instead of being
 827 sequestered at depth. To determine the relative importance of these two mechanisms (ven-
 828 tilation versus sequestration) in contributing to the positive heat content tendency at
 829 different depths and throughout the Arctic in *ASTER1*, a more detailed analysis of AW
 830 circulation and ventilation will be needed in future work.

831 In the Barents Sea, Lind et al. (2018) documented pronounced increases in decadal
 832 mean OHC in the upper 100 m of the water column, which they attributed to an increase
 833 in AW inflow through the Barents Sea Opening. In Fig. 17c we compare OHC trend (up-
 834 per 100 m) from Lind et al. (2018) with *ASTER1* illustrating that *ASTER1* captures
 835 the 2002–2016 positive trend. Further south, Piecuch et al. (2017) and Foukal and Lozier
 836 (2018) have quantified OHC trends in the SPNA (between 46°N and 65°N) using SST,
 837 ECCOv4r3 and OHC derived from the Hadley Centre EN4 gridded product. The compar-
 838 ison between Foukal and Lozier (2018) and *ASTER1* (Fig. 17d) shows good quan-
 839 titative agreement, with an increase in OHC between 2002–2005, a decrease in OHC be-
 840 tween 2005–2009, and a hiatus between 2009–2014, followed finally by a further decrease
 841 in OHC after 2014.

842 **4.4.2 Freshwater Content**

843 Based on observations, principally from satellite altimetry and ITPs in the Beau-
 844 fort Sea, the liquid freshwater content (FWC) in the Arctic has been increasing (Proshutinsky
 845 et al., 2019). Proshutinsky et al. (2020) summarized recent works attributing this FWC
 846 increase to several factors including shifts in atmospheric circulation, increased FW fluxes
 847 through the Bering Strait, and increased runoff from the MacKenzie river. A compar-
 848 ison between *ASTER1* and Proshutinsky et al. (2019) estimates for FWC in the Beau-
 849 fort Gyre shows that *ASTER1* captures the observed increase in FWC between the 2004
 850 to 2008. With the exception of a small decrease in 2015 – also seen in the observations
 851 – the Beaufort Gyre FWC in *ASTER1* remains relatively constant for the period 2008–
 852 2017 (Fig. 17b). Proshutinsky et al. (2019) report an increase from 2015–2017 which is
 853 likely missing from *ASTER1* due to the omission of both increased river runoff and land
 854 ice discharge in our forcing climatology and absence of the observed increase in FW im-
 855 port through the Bering Strait as previously discussed (Fig 16).

856 The connection between the Arctic FWC increase and circulation changes in the
 857 GIN Seas and North Atlantic has been the subject of several investigations (Dukhovskoy
 858 et al., 2016; Carmack et al., 2016; Tesdal & Haine, 2020). A recent review by Haine et
 859 al. (2015) summarized Arctic exchanges with the Canadian Arctic Archipelago (north
 860 of Davis Strait) and the Barents Sea (east of the Barents Sea Opening). These estimates
 861 heavily rely upon atmospheric reanalyses (for the provision of surface fluxes) and uncon-
 862 strained model output (for tracer content change). Further south, Dukhovskoy et al. (2019)
 863 investigated the redistribution of increased Greenland freshwater discharge (solid and
 864 liquid) in the Subpolar North Atlantic (SPNA) and the GIN Seas, highlighting large un-
 865 certainty due both to lack of constraint and acute dependency of transports on model
 866 resolution (see also Weijer et al., 2012).

867 **5 Discussion**

868 A preliminary discussion of the state estimate focuses on the question of which con-
 869 trol variables played a dominant role in achieving a reduction in misfit between obser-
 870 vations and the model (Section 5.1). A second point of discussion highlights known is-
 871 sues with this first release of ASTE and suggestions on how to improve future releases
 872 (Section 5.2).

873 **5.1 Identifying Key Control Adjustments**

Experiment 1		Experiment 2	
Ensemble Member	optimized control(s) <i>added</i>	Ensemble Member	optimized control(s) <i>withheld</i>
1	$[\theta_0^{R1}, S_0^{R1}]$	1	$[\theta_0^{i0}, S_0^{i0}]$
2	$[\mathcal{K}_\sigma^{R1}, \mathcal{K}_{gm}^{R1}]$	2	$[\mathcal{K}_\sigma^{i0}, \mathcal{K}_{gm}^{i0}]$
3	\mathcal{K}_z^{R1}	3	\mathcal{K}_z^{i0}
4	$[u_w^{R1}, v_w^{R1}]$	4	$[u_w^{i0}, v_w^{i0}]$
5	T_{air}^{R1}	5	T_{air}^{i0}
6	q_{air}^{R1}	6	q_{air}^{i0}
7	$[R_{sw}^{R1}, R_{lw}^{R1}]$	7	$[R_{sw}^{i0}, R_{lw}^{i0}]$
8	P^{R1}	8	P^{i0}

Table 5. Ensemble members for each of the two ensemble experiments. In experiment 1, the control variables listed in column #2 were *added* to *it0* ; in experiment 2, the control variables listed in column #4 were *withheld* from *ASTE_R1* .

874 Optimization of the *ASTE_R1* solution was achieved by iterative adjustment of a
 875 set of control variables, as described in Section 2.2. Our control space (Ω) comprises 3D
 876 fields of initial (i.e., 01/01/2002) temperature and salinity (θ_0, S_0), time-mean ocean mix-
 877 ing coefficients ($\mathcal{K}_\sigma, \mathcal{K}_{gm}$, and \mathcal{K}_z), and time-varying 2D fields of near-surface atmospheric
 878 state variables ($T_{air}, q_{air}, u_w, v_w, R_{sw}, R_{lw}$, and P). We now seek to identify which of these
 879 control variable adjustments were key for the reduced model-data misfits in *ASTE_R1*
 880 relative to the unoptimized *it0* .

881 To proceed, we performed two additional forward ensemble experiments, each con-
 882 sisting of eight members. In the first ensemble, optimized controls from *ASTE_R1* were
 883 substituted into *it0* , which was then re-run. Each ensemble member is characterized by
 884 containing one of the *ASTE_R1* optimized control variables/variable pairs listed in Ta-
 885 ble 5 (left two columns). Note that there are 4 pairs: the optimized initial conditions (θ_0^{R1}, S_0^{R1}),

886 the optimized diffusivities for the eddy mixing parameterization ($\mathcal{K}_\sigma^{R1}, \mathcal{K}_{gm}^{R1}$), the two com-
 887 ponents of the wind speed (u_w^{R1}, v_w^{R1}), and the net downward radiation (R_{sw}^{R1}, R_{lw}^{R1}) For
 888 any given ensemble member, large reductions in misfit indicate that the substituted op-
 889 timized control may play an important role in the *ASTER1* solution. This is further
 890 supported if misfits are not only reduced but brought close to their *ASTER1* value.

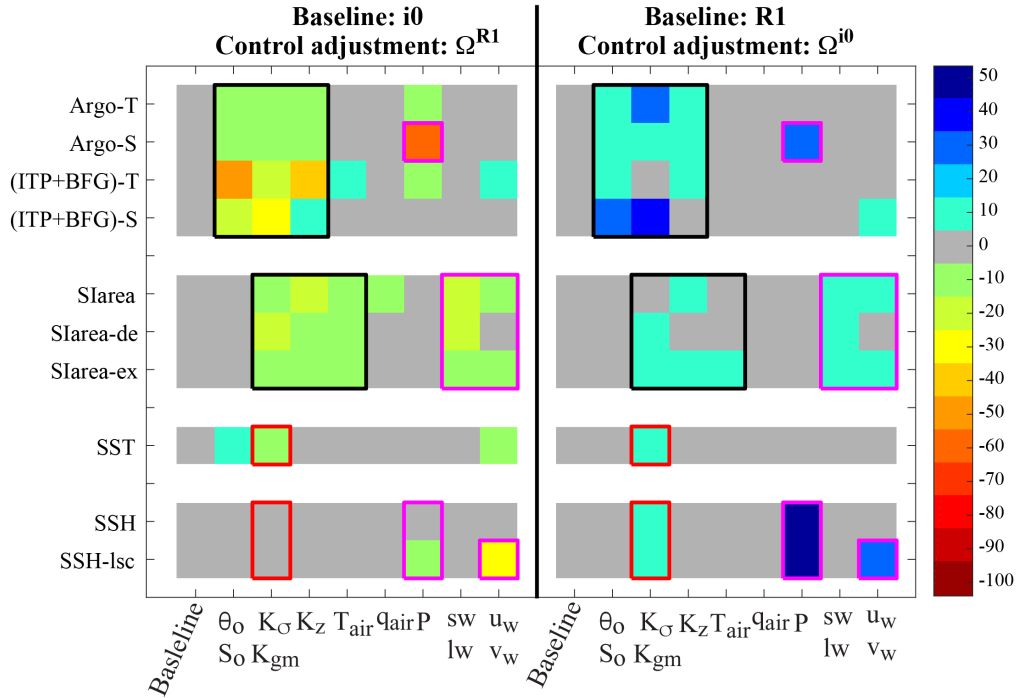


Figure 19. Percentage change (color) in cost with respect to the constraint listed on the ordinate, attributable to the control substitutions given on the abscissa. The left group are members of the first ensemble of perturbation experiments, for which optimized controls Ω^{R1} are substituted into the *it0* re-runs. The right group are members of the second ensemble, for which non-optimized controls Ω^{i0} are substituted into the *ASTER1* re-runs. On the left half of the plot, negative values indicate an improved solution i.e., a cost reduction with respect to *it0*. On the right half, positive values indicate deterioration of the solution i.e., a cost increase with respect to *ASTER1*. Colored rectangular outlines highlight patterns of most impactful control variables (e.g., precipitation is important for the reduction of costs to Argo salinity and SSH).

891 However, a note of caution is needed. Our controls are not fully independent (e.g.,
 892 some of the atmospheric state variable controls are related via bulk formulae) and as a
 893 result, it is not possible to determine their full impact in isolation. For this reason, we
 894 performed a second ensemble experiment, reversing the sense of the substitutions, so that
 895 the non-optimized controls from *it0* were substituted into *ASTER1*, which was then
 896 re-run. In this experiment, each member is characterized by containing one of the *it0* non-
 897 optimized control variables/variable pairs listed in Table 5 (right two columns). This sec-
 898 ond ensemble lends confidence to our assessment as follows: an optimized control is highly
 899 likely to be an important ingredient of the *ASTER1* solution if its incorporation notably
 900 improves the *it0* re-run (first ensemble) while its omission notably degrades the *ASTER1*
 901 re-run (second ensemble).

902 In Fig. 19 we examine the impact of the control substitutions on the costs in both
 903 ensemble experiments. We show only normalized costs with respect to the following data

sets: Argo, ITP, Beaufort Gyre moorings, and satellite-based observations of SST, SSH and sea ice concentration. This choice enables a more focused discussion whilst also informing the large-scale quality of the solution near the ocean surface (from SSS and SST data) and throughout the upper ocean in the North Atlantic, GIN Seas, and Labrador Sea interior (from Argo T and S data) and in the western Arctic (from ITP and Beaufort Gyre moorings). Lastly, costs for sea ice concentration indicate performance of modelled air-sea fluxes and mixed layer properties in marginal ice zones (see Fig. 6 and related discussion). Our analysis reveals the importance of precipitation (P) adjustments in obtaining realistic subsurface salinity distributions in the North Atlantic (Fig. 19) through the removal of the systematic excess rain bias discussed in Section 3.3 (Fig. 12d). Inclusion of the optimized precipitation P^{R1} in the *it0* re-run reduced the model cost with respect to Argo salinity by 56%. A 31% increase in this cost was seen on omission of the optimized precipitation in the *ASTE_R1* re-run. Large improvements in SSH can also be attributed in part to corrected precipitation, as well as surface winds. Amongst other atmospheric forcing variables, surface air temperature, downward radiative forcing, and winds all have important impact on the sea ice cover (collective average of 17% improvement to *it0* and 5% degradation to *ASTE_R1*).

Adjustments to the initial conditions, vertical diffusivity and eddy mixing are also found to be important for improving subsurface hydrography throughout the *ASTE_R1* domain. Optimized eddy mixing-related controls (\mathcal{K}_σ^{R1} , \mathcal{K}_{gm}^{R1}) alone result in a 14% improvement (and 14% degradation) of the Arctic hydrography misfit when included (omitted) from the *it0* (*ASTE_R1*) re-runs, respectively. These adjustments to the eddy mixing parameters also improve SST and SSH, and – in addition to the adjustments made to the vertical diffusivity and atmospheric conditions – are also seen to be critical for improved representation of sea ice cover.

5.2 Known Issues and Future Directions

During production of *ASTE_R1* we have striven to utilize all known constraints that the state estimation machinery could handle. This constraint comprises $O(10^9)$ observations from the diverse data sources (Table 2). Despite this effort, some systematic biases remain. Here we discuss notable issues in the *ASTE_R1* solution and possible future directions for developing the next ASTE release.

Eastern Arctic hydrography: One of the largest remaining systematic biases is found in the Eurasian Basin, where subsurface constraints comprise sparse ITP sampling of the basin interior alone. Although the inflow is constrained by moorings at the Fram Strait, downstream observation of the circulation, eddy-induced stirring and vertical mixing in the Eurasian Basin along the shelf-basin slope and interior are limited (Fig. 20a). The serious implications of this paucity of data are highlighted by considering that the AW inflow takes ~ 6 -10 years to transit this region without local constraint. As a result the inverse problem is highly under-determined. In practice, under-determination allows non-unique pathways to misfit minimization. For *ASTE_R1* , we find that the AW layer in the Eastern Arctic, though much improved from *it0* , thickens over time (Fig. 20), a problem common to many state-of-the-art Arctic Ocean models (Holloway et al., 2007; Illicak et al., 2016; Docquier et al., 2019; Uotila et al., 2019).

As it is unlikely that widespread observation of 3-D velocity and mixing will be made in the near future, we anticipate that AW watermass representation in the Eurasian basin will remain an issue for both the next generation of state-of-the-art Arctic Ocean models and the next ASTE release. Although we do not expect large gains from planned changes to the ocean observing system in the near future, we do anticipate improvements in sea ice state, mixed layer representation, and shelf-basin exchanges in the next ASTE release, due to recent improvements to the stability of the adjoint of the sea ice thermodynamics (Bigdeli et al., 2020). This will enable a more complete use of sea ice observations

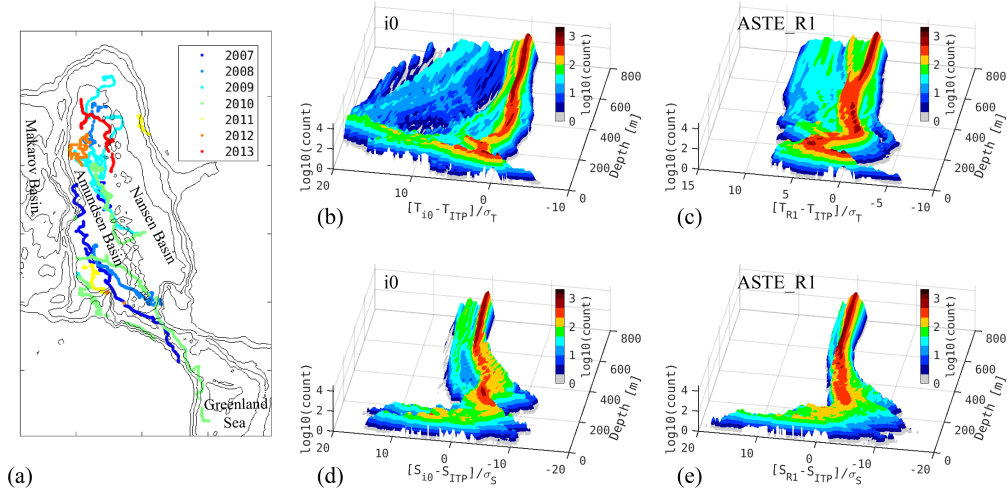


Figure 20. (a) Spatial distribution of ITP data used to constrain *ASTE_R1* in the Eurasian Basin ; colors distinguish acquisition year. Histograms of normalized misfit to ITP (b,c) temperature and (d,e) salinity as a function of depth in the Eurasian Basin for (b,d) *it0* and (c,e) *ASTE_R1* .

955 as active contributions to the cost function reduction J (eqn. (1)). The sensitivity of the
 956 associated model-data misfits to the control space can then be used to better adjust at-
 957 mospheric forcings. This will allow us to fully leverage the constraint from satellite-based
 958 observations of the sea-ice state, which could only be partly exploited in the pseudo sea
 959 ice adjoint employed for construction of *ASTE_R1* . Inclusion of the sea ice thermody-
 960 namics adjoint could potentially improve AW upward ventilation (Ivanov et al., 2012;
 961 Polyakov et al., 2020) and preserve a more stable AW layer thickness, both in the Eurasian
 962 Basin and further downstream in the Western Arctic.

963 *Arctic Circumpolar Current:* In the Laptev Sea it is thought that the circumpo-
 964 lar circulation of AW splits at $\sim 145^\circ\text{E}$, with a fraction returning to the Fram Strait along
 965 the Lomonosov Ridge (Rudels, 2015) and the remainder continuing along the basin’s rim
 966 into the Western Arctic although the exact partitioning is not well constrained. In the
 967 Western Arctic it is typically assumed that the AW continues to circulate cyclonically
 968 along the basin boundary, although both *ASTE_R1* (Grabon, 2020) and a modeling ef-
 969 fort informed by observed radionuclide distributions (Karcher et al., 2012) suggest a weak
 970 anticyclonic circulation during the last decade. Recent work analyzing all available cur-
 971 rent meters (updated from Baumann et al. (2018)) has yielded velocity probability dis-
 972 tributions for the Arctic region. This will be investigated as a novel approach to con-
 973 strain ocean velocities within the AW circulation in the next ASTE release. In addition,
 974 a more detail examination of the momentum and vorticity budgets along the circumpo-
 975 lar current will offer insights into the role of viscous dissipation and eddies in maintain-
 976 ing the cyclonic sense of circulation (Yang, 2005; Spall, 2020).

977 *Arctic river runoff and Greenland discharge:* FW transports and content in the
 978 late 2010s are low in *ASTE_R1* relative to independent observations (Section 4.3 and 4.4.2).
 979 Near the surface in the Arctic and along the Greenland coast, recent increases in river
 980 (A. Shiklomanov et al., 2020) and tundra runoff (Bamber et al., 2012), surface solid and
 981 subsurface glacial discharge (Bamber et al., 2012, 2018) have been observed. This increase
 982 was not included in the *ASTE_R1* forcing. Meaningful application of these FW fluxes
 983 as model forcings, especially in the Arctic marginal seas, requires careful consideration
 984 of the following factors. Sub-glacial discharge is observed to enter the outlet glacier fjord

at depths near the grounding line instead of at the surface of the fjord’s exit to the continental shelf (Straneo & Cenedese, 2015; Sciascia et al., 2013). Mixing and entrainment of this FW with the surroundings creates modified water whose property is prohibitively difficult to continuously track downstream from the source using observed T/S (Beaird et al., 2018). Consequently, the pathways of FW redistribution are highly uncertain. Numerical simulations with Greenland discharge distributed at the surface yield pathways from the source into the interior of SPNA and GIN seas that vary substantially with model resolution and representation of mean currents (Weijer et al., 2012; Dukhovskoy et al., 2016). The depth to which this FW is mixed down also varies highly with resolution (Dukhovskoy et al., 2016), causing near surface over-freshening in certain cases and a 30–50% decrease in the North Atlantic Meridional Overturning Circulation (AMOC) at time-scales varying between 3–50 years (Weijer et al., 2012). Similarly, preliminary sensitivity experiments in *ASTE_R1* with observed Greenland discharge applied at the surface show over-freshening of the upper ocean in the Greenland Sea and a decrease in the AMOC at 55°N by 40% within 5 years, inconsistent with observations (not shown). Prior to the next *ASTE* release, a dedicated study will be required to implement updated estimates of Greenland discharge as a subsurface freshwater forcing, consistent with observations (Straneo & Cenedese, 2015). This will entail incorporation of a melt water plume parameterization into the *ASTE* framework. Lastly, instead of being absorbed into net $E-P-R$, a new control variable for runoff will be introduced to isolate and fully interrogate sensitivity to subsurface forcing from subglacial discharge.

Subpolar North Atlantic hydrography: In the SPNA, a warm bias in *ASTE_R1* at 1000–2000 m depth (Fig. 13c) is associated with poor representation of transport across the GSR, a common problem in coarse to medium resolution ocean models (Gerdes et al., 2006; Heuzé & Årthun, 2019). Specifically, these models produce lower volume and heat transports across the GSR compared to observations (Heuzé & Årthun, 2019). Since the resolution of *ASTE_R1* is ~ 18 km in the subpolar gyre, we anticipate incomplete representation of both eddy/diffusive mechanisms – estimated to be important across the shallow Denmark Strait and Iceland-Faroe Ridge (Buckley et al., 2015) – and watermass transformations in the *ASTE_R1* solution. Thus, although *ASTE_R1* can capture the mean transports of volume and heat between Iceland and Scotland (Fig. 14–16), the remaining warm bias across Denmark Strait and south of the GSR likely impacts our estimate of heat content in both the eastern SPNA and Nordic Seas and alters the optimized air-sea heat flux in both regions. Recent data from the Overturning in the Subpolar North Atlantic Program (OSNAP) observing system (Lozier et al., 2017, 2019) mooring array (deployed in 2014) will provide important information in the subpolar region, and an especially valuable constraint on the boundary currents and overflow waters, not captured by Argo.

1023 6 Summary and Outlook

1024 We have presented the first release of the Arctic Subpolar gyre sTate Estimate, *ASTE_R1*
 1025 , a data-constrained and dynamically consistent ocean-sea ice synthesis spanning the pe-
 1026 riod 2002–2017. *ASTE_R1* is produced using the ECCO adjoint-based state estimation
 1027 framework, in which an ocean general circulation model, the MITgcm serves as a dynam-
 1028 ical interpolator, spreading the influence of $O(10^9)$ incorporated observations through
 1029 space and time by way of linearized adjustment processes encapsulated in an adjoint model.
 1030 Importantly, the model-data misfit is reduced via iterative adjustments to the initial hy-
 1031 drographic conditions, atmospheric forcing and model mixing parameters alone, ensur-
 1032 ing adherence to the governing equations throughout the entire estimation period. This
 1033 distinguishes our approach from ocean reanalysis, in which violation of conservation laws
 1034 complicates application for climate research (Stammer et al., 2016). The ability to as-
 1035 sess closed tracer and momentum budgets in *ASTE_R1* is a key strength of the prod-
 1036 uct. As all sources and sinks are accounted for, full heat, salt and momentum (or vor-

1037 ticity) budgets can be analyzed to identify dominant sources contributing to the observed
 1038 changes. These closed budget analyses can also be performed in T , S , σ space follow-
 1039 ing R. P. Abernathy et al. (2016), enabling diagnosis of watermass evolution and de-
 1040 struction in the *ASTER1* solution. In addition, the adjoint modeling infrastructure al-
 1041 lows for linear sensitivity studies using *ASTER1* for investigation of causal mechanisms
 1042 underlying variability in key quantities of climate interest (e.g., Bigdeli et al., 2020; Nguyen,
 1043 Woodgate, & Heimbach, 2020; Pillar et al., 2016).

1044 During production of *ASTER1* we have strived to utilize all known constraints that
 1045 the state estimation machinery can handle. *ASTER1* thus arguably represents the biggest
 1046 effort undertaken to date with the aim of producing a specialized Arctic ocean-ice es-
 1047 timate, freely available to the research community. This complements existing global ECCO
 1048 solutions (Forget, Campin, et al., 2015; Fukumori et al., 2018), the Southern Ocean State
 1049 Estimation (SOSE, (Mazloff et al., 2010)) and other global and regional ECCO deriva-
 1050 tives (e.g., Köhl & Stammer, 2008; Gopalakrishnan et al., 2013; Zaba et al., 2018).

1051 For this initial assessment of *ASTER1*, we have focused on comparison to avail-
 1052 able observational constraints. Many of these were actively employed in the optimiza-
 1053 tion procedure, but many others (e.g., all volume and tracer transport estimates) were
 1054 withheld, allowing independent verification. The optimized solution serves as a signif-
 1055 icant improvement from the unconstrained state, achieving consistency with the major-
 1056 ity of incorporated observations, including both the set used in the optimization and that
 1057 retained for post-validation (Table 3).

1058 The most substantial misfit reductions seen in *ASTER1* are sea ice cover in the
 1059 marginal ice zone, western Arctic hydrography, and subtropical North Atlantic sea level
 1060 anomaly and subsurface salinity (Table 3, Fig. 5). In the Arctic Mediterranean, using
 1061 only a proxy sea ice adjoint, *ASTER1* achieves a 83% reduction in misfit to satellite-
 1062 derived sea ice concentration constraints, mainly via improved representation of the sea-
 1063 ice edge (Fig. 6). The solution faithfully reproduces both the observed seasonal cycle and
 1064 low frequency trend of sea-ice extent.

1065 At the Fram Strait, the mooring array is crucial to constraining the important AW
 1066 inflow and local hydrographic properties. At this important Arctic gateway, *ASTER1*
 1067 exhibits a 58% misfit reduction through the water column across the strait relative to
 1068 the unconstrained solution. In the Arctic interior, ITPs provide unique information on
 1069 the subsurface hydrography. Because 71% of the ITP profiles are located within the up-
 1070 per 5–800 m in the Canada Basin interior, the most significant misfit reduction was seen
 1071 here (85% in T and 62% in S , Fig. 9). In the remaining Arctic basin, low data coverage,
 1072 combined with large uncertainty in the mean circulation and mixing parameters, resulted
 1073 in less notable improvement (reductions of 89% in T and 31% in S), but biases persist,
 1074 especially at depth below the AW core (Fig. 20).

1075 Accompanying improved fit to hydrographic data used to constrain the solution,
 1076 we find improvements in basin-scale heat and freshwater content. Interannual variabil-
 1077 ity and low frequency trends in both heat and FW content are well represented in the
 1078 Arctic Mediterranean and SPNA of *ASTER1*. In the Beaufort Sea, *ASTER1* captures
 1079 the observed steady increase in upper halocline heat content from 2004–2017. Both the
 1080 observed heat content increase in the upper water column within the Barents Sea and
 1081 the heat content decrease in the east SPNA are also consistently captured (Fig. 17).

1082 We have been careful to clearly outline the notable biases remaining in the *ASTER1*
 1083 solution. These include a warm bias below the AW core in the eastern Arctic and in the
 1084 east SPNA. The cause is a combination of lack of constraint here for the hydrography,
 1085 mean circulation, and the adjustable initial condition and parametric controls. Additional
 1086 biases exist in FW transports and contents in the Arctic Mediterranean due to the omis-
 1087 sion of increased runoff from Arctic rivers and Greenland freshwater discharge.

1088 An advantage of our approach is that the use of a dynamical – as opposed to sta-
1089 tistical – interpolator can improve spectral representation of the estimated state com-
1090 pared to gridded products produced using statistical interpolations (e.g., Verdy et al.,
1091 2017). This has not been addressed here, but it is a useful avenue for future ASTE as-
1092 sessments and ongoing development.

1093 Looking toward the next *ASTE_R1* release, we expect the greatest progress will
1094 be made by incorporating new model physics. In particular, improving the stability of
1095 the sea ice thermodynamic adjoint (Bigdeli et al., 2020) will enable its use in ASTE, pro-
1096 viding stronger constraint of air-ice-sea exchanges and ocean ventilation. Future efforts
1097 will target hydrographic improvements along the Arctic shelf-basin slope in the eastern
1098 Arctic to reduce the *ASTE_R1* AW layer warm bias. Additionally, updated estimates
1099 of runoff and calving fluxes and inclusion of a parameterization of sub-glacial discharge
1100 will enable improved estimate of freshwater redistribution and interbasin exchange. New
1101 constraints, including datasets from the OSNAP mooring array (Lozier et al., 2017, 2019),
1102 sea surface salinity (Vinogradova & Ponte, 2012; Fournier et al., 2019), and sea ice thick-
1103 ness (Tian-Kunze et al., 2014; Ricker et al., 2017) will also be fully utilized in the pro-
1104 duction of a further improved next ASTE release.

1105 Appendix A *ASTE_R1* Product Distribution

1106 A1 Configuration set up

1107 The model configuration and all necessary inputs, including the optimized control
 1108 adjustments, required for *ASTE_R1* re-runs are available to the public, as discussed in
 1109 the next section. The code base employed for *ASTE_R1* production was MITgcm check-
 1110 point c65q. *ASTE_R1* was built using the full state estimation infrastructure, includ-
 1111 ing specialized packages for misfit and adjustment evaluation, developed for ECCOv4r1
 1112 (Forget, Campin, et al., 2015). In addition, two code developments specific to *ASTE* in-
 1113 clude the implementation of a vertical diffusivity power control ($\log_{10}\mathcal{K}_z$) and the ca-
 1114 pability to switch between daily and monthly SSH costs.

1115 To ensure numerical stability during *ASTE_R1* production, the following model choices
 1116 were important: (a) a staggered time-step for momentum advection and Coriolis terms;
 1117 (b) third-order advection for tracers (scheme code 30 in Table 2.2 in Adcroft et al., 2018),
 1118 (c) linear free surface approximation, and (d) application of freshwater forcing via a vir-
 1119 tual salt flux (i.e., no accompanying change in mass). These choices permitted a time-
 1120 step of 1200 s. After 62 iterations, better model choices were used for the final forward
 1121 run that produces more accurate physics in the distributed version of *ASTE_R1*. These
 1122 include (i) seventh order advection for tracers (scheme code 7 in Table 2.2 in Adcroft et
 1123 al., 2018); (ii) nonlinear free surface with scaled z^* coordinates (Adcroft & Campin, 2004),
 1124 and (iii) application of freshwater forcing via a real freshwater flux (i.e., with accompa-
 1125 nying change in mass, Campin et al., 2004). These choices required a shorter time-step
 1126 of 600 s. **The *ASTE_R1* solution described and assessed in this paper is from**
 1127 **the re-run of iteration 62 with the model choices (i)–(iii) described above.**

1128 In the distributed code, at compile and run-time, the user has the choice to use the
 1129 more stable set up with a time-step of 1200 s or employ the more accurate physics with
 1130 a time-step of 600 s as described above. We found that these small changes in the model
 1131 configuration for the final forward run did not have a significant impact on the solution.
 1132 The advantage of their application here is in enabling more accurate physical interpre-
 1133 tations of mass and freshwater budgets. However, since these options also require a shorter
 1134 timestep (for the nonlinear free surface) and a larger stencil (for the higher order advec-
 1135 tion), their use demands significantly more computational resources (twice the walltime).
 1136 For this reason, it was not feasible to employ these options until the final stages of *ASTE_R1*
 1137 development.

1138 A2 Distribution of the *ASTE_R1* solution

1139 The full *ASTE_R1* solution is publicly available through the UT-Austin ECCO por-
 1140 tal at: <https://web.corral.tacc.utexas.edu/OceanProjects/ASTE/>, provided by the
 1141 Texas Advanced Computing Center (TACC). Here we have made available:

- 1142 • time varying fields from *ASTE_R1* as monthly and climatological averages,
- 1143 • monthly snapshots of the time varying ocean state,
- 1144 • fields representing the underlying grid,
- 1145 • compile time and run time inputs necessary to reproduce these fields with the MIT-
 1146 gcm,
- 1147 • some MATLAB scripts to help analyze the *ASTE_R1* fields.

1148 All fields are available here as NetCDF files.

1149 The monthly mean fields are additionally stored in a compressed format on Ama-
 1150 zon Web Services (AWS) servers, provided by TACC at [http://aste-release1.s3-website](http://aste-release1.s3-website.us-east-2.amazonaws.com/)
 1151 [.us-east-2.amazonaws.com/](http://aste-release1.s3-website.us-east-2.amazonaws.com/). These files are meant to be accessed with the `llcreader`
 1152 module of the open source python package `xmitgcm` (R. Abernathey et al., 2019), which

1153 allows users to analyze the data without the need to actually download it. An interac-
 1154 tive demonstration of this capability, which shows some sample calculations enabled by
 1155 `xgcm` (R. Abernathey et al., 2020) and `ECCOV4-py` ([github.com/ECCO-GROUP/ECCOV4](https://github.com/ECCO-GROUP/ECCOV4-py)-
 1156 `-py`), is available through the Binder Project (Project Jupyter et al., 2018) at [github](https://github.com/crios-ut/aste)
 1157 `.com/crios-ut/aste` (T. Smith, 2020). This repository additionally contains environ-
 1158 ment files so that any user can reproduce the computing environment necessary to an-
 1159 alyze `ASTE_R1`, for instance on their own laptop.

1160 Appendix B Transport Calculation with Referenced θ/S

1161 Here we describe heat and freshwater transport calculations used in `ASTE_R1` with
 1162 respect to reference values of potential temperature (θ_r) and salinity (S_r), respectively.
 1163 This serves to (1) provide calculation details for comparison to those used by previously
 1164 published estimates (supplementing results presented in section 4), and (2) expose where
 1165 calculation differences may prevent meaningful comparisons (following discussion in sec-
 1166 tion 2.3). For budget calculations, we refer the readers to detailed descriptions provided
 1167 in Piecuch (2017) and Forget, Campin, et al. (2015).

1168 In the literature, transports are often computed with nonzero referenced values θ_r/S_r .
 1169 In section 4 we also provided online transport estimates for `ASTE_R1` made using non-
 1170 zero references (e.g., for the heat flux through the Bering Strait). We caution here, how-
 1171 ever, that all offline transport calculations made using available diagnostics from `ASTE_R1`
 1172 (and all standard configurations of the MITgcm) will be exact only with $\theta_r = 0$ and
 1173 $S_r = 0$, as these are the values used in all online tracer equations. To support users seek-
 1174 ing to compute `ASTE_R1` transports offline assuming nonzero references, we now exam-
 1175 ine the loss of accuracy that will be incurred. This loss of accuracy depends on the am-
 1176 plitude of various missing terms (e.g., bolus transports and diffusive fluxes) relative to
 1177 the contributions (e.g., Eulerian advection) contained in the available diagnostics. By
 1178 deriving these approximations here and comparing their magnitudes with the accurate
 1179 online values across important Arctic and GIN Seas gateways, we aim to identify which
 1180 transports reported in Fig. 15-16 are reliable and which ones require caution for inter-
 1181 pretation.

1182 B1 Accurate transport calculations

The horizontal transports of volume, heat, and freshwater (FW) across the Arctic
 Mediterranean gateways are calculated by summing the total horizontal convergence
 in the mass, heat, and salinity budgets, respectively, (Piecuch, 2017) as follows,

$$F_V = \int_L \int_{-D}^{\eta} \mathbf{u}_E \cdot \hat{\mathbf{n}} \, dz \, dl \quad (\text{B1.0})$$

$$\begin{aligned} F_H &= \rho_0 C_p \int_L \int_{-D}^{\eta} (\theta - \theta_r) (\mathbf{u}_E + \mathbf{u}_b) \cdot \hat{\mathbf{n}} \, dz \, dl + \rho_0 C_p F_{\theta, dif} + F_{H_i, adv} + F_{H_{sn}, adv} \\ &= F_{H_{\theta, adv}} + F_{H_{\theta, dif}} + F_{H_i, adv} + F_{H_{sn}, adv} \end{aligned} \quad (\text{B2.0})$$

$$\begin{aligned} F_{FW} &\approx \int_L \int_{-z_{S_r}}^{\eta} \frac{(S_r - S)}{S_r} (\mathbf{u}_E + \mathbf{u}_b) \cdot \hat{\mathbf{n}} \, dz \, dl + \left(1 + \frac{\eta}{D}\right) \frac{F_{S, dif}}{S_r} + \int_L \left(\frac{S_r - S_i}{S_r} \frac{\rho_i}{\rho_0} h_i \mathbf{u}_i + \frac{\rho_{sn}}{\rho_0} h_{sn} \mathbf{u}_{sn} \right) \cdot \hat{\mathbf{n}} \, dl \\ &= F_{FW_S, adv} + F_{FW_S, dif} + F_{FW_i, adv} + F_{FW_{sn}, adv} \end{aligned} \quad (\text{B3.0})$$

1183 where t is the time, \mathbf{u}_E , \mathbf{u}_b the (shaved-cell-weighted) ocean resolved Eulerian and un-
 1184 resolved bolus velocities, and \mathbf{u}_i , \mathbf{u}_{sn} the sea ice and snow Eulerian velocities. For each
 1185 gateway across which the transports are computed, $\hat{\mathbf{n}}$ is the normal direction at each model
 1186 grid point along the transport gate and L the section length along the gate. Vertical in-
 1187 tegration is between η the sea surface and $-D$ the ocean floor depth for volume and heat
 1188 transports. Constants $\rho_0 = 1029$, $\rho_i = 910$ and $\rho_{sn} = 330$ are the seawater, sea ice,
 1189 and snow densities in kg/m^3 . $C_p = 3996 \text{ J}^\circ\text{C}^{-1}\text{kg}^{-1}$ is the specific heat capacity of sea

1190 water, θ_r the reference temperature, $S_r = 34.8$ psu the reference salinity, and $S_i = 4$ psu
 1191 the constant sea ice salinity used in ASTE. θ and S are the ocean potential temperature
 1192 and salinity in $^{\circ}\text{C}$ and psu, respectively; h_i and h_{sn} are the thickness of sea ice and snow
 1193 in m. $F_{\theta,dif}$ and $F_{S,dif}$ are the parameterized diffusive flux of potential temperature and
 1194 salinity $\theta_r = 0$ and $S_r = 0$. For both advective and diffusive contributions to fresh-
 1195 water transports (Eqn B3.0), vertical integration is only down to the depth of the refer-
 1196 ence isohaline $-z_{S_r}$.

1197 Exact closure of heat budgets (see equations in Forget, Campin, et al. (2015) and
 1198 Piecuch (2017)) and exact (to within numerical precision) calculation of heat transports
 1199 (Eqn B2.0) can be achieved when $\theta_r = 0$ and all diagnostics terms are computed on-
 1200 line. Near exact freshwater budgets (see equations in Forget, Campin, et al. (2015) and
 1201 Tesdal and Haine (2020)) and transports (Eqn B3.0) can be achieved with $S_r = 0$. Ad-
 1202 ditionally the vertical integral must be computed every time step, continuously updat-
 1203 ing the time-evolving z_{S_r} .

1204 B2 Approximations for nonzero θ_r/S_r

1205 When using nonzero reference values (e.g., $\theta_r = -0.1^{\circ}\text{C}$ or $S_r = 34.8$ psu as in
 1206 Østerhus et al., 2019), neither heat nor freshwater diffusion terms are available in the
 1207 offline diagnostics. To gauge orders of magnitudes, however, we approximate the diffu-
 1208 sion term for FW using $F_{S,dif}$ scaled by the non-linear free-surface factor $(1 + \frac{T}{D})$ fol-
 1209 lowing Piecuch (2017), then further scale by $\frac{1}{S_r}$. For the advection terms, the long-term
 1210 mean transport can be derived exactly for heat and approximated for FW using a com-
 1211 bination of readily available offline diagnostics for volume and heat/salt budgets as fol-
 1212 lows:

$$\begin{aligned} \langle F_{H_{\theta},adv} \rangle &= \rho_0 C_p \left\langle \int_{-D}^{\eta} \int_L \left((\theta - \theta_r)(\mathbf{u}_E + \mathbf{u}_b) \right) \cdot \hat{\mathbf{n}} \, dz \, dl \right\rangle \\ &= \rho_0 C_p \left\langle \int_{-D}^{\eta} \int_L \theta(\mathbf{u}_E + \mathbf{u}_b) \cdot \hat{\mathbf{n}} \, dz \, dl \right\rangle - \rho_0 C_p \theta_r \left\langle \int_{-D}^{\eta} \int_L \mathbf{u}_E \cdot \hat{\mathbf{n}} \, dz \, dl \right\rangle \end{aligned} \quad (\text{B2.1})$$

$$\begin{aligned} \langle F_{FW_S,adv} \rangle &\approx \left\langle \int_{-z_{S_r}}^{\eta} \int_L \frac{(S_r - S)}{S_r} (\mathbf{u}_E + \mathbf{u}_b) \cdot \hat{\mathbf{n}} \, dz \, dl \right\rangle \\ &\approx \left\langle \int_{-z_{S_r}}^{\eta} \int_L \left(\frac{S_r}{S_r} (\mathbf{u}_E + \mathbf{u}_b) - \frac{S}{S_r} (\mathbf{u}_E + \mathbf{u}_b) \right) \cdot \hat{\mathbf{n}} \, dz \, dl \right\rangle \\ &\approx \left\langle \int_{-z_{S_r}}^{\eta} \int_L \mathbf{u}_E \cdot \hat{\mathbf{n}} \, dz \, dl \right\rangle - \frac{1}{S_r} \left\langle \int_{-z_{S_r}}^{\eta} \int_L S (\mathbf{u}_E + \mathbf{u}_b) \cdot \hat{\mathbf{n}} \, dz \, dl \right\rangle \end{aligned} \quad (\text{B3.1})$$

1213 where the $\langle \cdot \rangle$ is the multi-year mean which ensures $\langle \mathbf{u}_b \rangle \equiv 0$ by definition. The approx-
 1214 imation in $F_{FW_S,adv}$ is due, again, to the reliance in the offline average of $\langle S \rangle$ in deter-
 1215 mining $-z_{S_r}$.

1216 B3 Approximations using monthly mean θ , \mathbf{S} and \mathbf{u}_E ,

1217 Lastly, we note that due to disk space and I/O restrictions, it is typical for mod-
 1218 elling studies to save and subsequently provide only monthly-averaged Eulerian veloc-
 1219 ity $\langle \mathbf{u}_E \rangle$ and tracers $\langle \theta \rangle$ and $\langle S \rangle$ for offline calculations of heat/FW transports and con-
 1220 tents (e.g., Jahn et al., 2012; Kinney et al., 2014; Q. Wang et al., 2016b, 2016a; Ilicak
 1221 et al., 2016; Heuzé & Årthun, 2019). In this case, the calculation for the advective terms
 1222 in heat and FW transports are further approximated due to the cross-terms involving
 1223 the bolus velocity $\mathbf{S}\mathbf{u}_b$ and $\theta\mathbf{u}_b$ being excluded:

$$F_{H_{\theta},adv} \approx \rho_0 C_p \int_{-D}^{\eta} \int_L (\theta - \theta_r) \mathbf{u}_E \cdot \hat{\mathbf{n}} dz dl \quad (\text{B2.2})$$

$$F_{FW_S,adv} \approx \int_{-z_{S_r}}^{\eta} \int_L \frac{(S_r - S)}{S_r} \mathbf{u}_E \cdot \hat{\mathbf{n}} dz dl \quad (\text{B3.2})$$

1224 As before, inaccuracies will be incurred when z_{S_r} is determined using the monthly mean
 1225 $\langle S \rangle$. This is the case for all results shown for FW because no diagnostics pertinent to
 1226 FW, including those of $S - S_r$ or z_{S_r} , are available standard MITgcm diagnostic out-
 1227 puts.

1228 B4 Interpretation of Transports: Confidence and Caution

1229 Fig. B1-B2 show time-series of heat and FW transports for key gateways using both
 1230 the most accurate online method and approximated offline method described above. The
 1231 diffusion terms for both heat and FW are at least two orders of magnitude smaller than
 1232 the advection terms and can be ignored almost everywhere. The exception is at the Den-
 1233 mark Strait and Iceland-Faroe channels where omission of the diffusive contribution to
 1234 the total heat transport leads to large errors of 30% and 100%, respectively. This shows
 1235 that the estimates of tracer transports across these two gates should be interpreted with
 1236 caution when computed offline using only model monthly outputs of the Eulerian veloc-
 1237 ity and tracer averages.

1238 For FW, as all methods are approximated, with the largest error likely due to not
 1239 tracking the time-evolving depth of the reference isohaline z_{S_r} . Since there is no exact
 1240 calculation for comparison, it is not possible to conclude which method, “adv” using the
 1241 online advective term (Eqn B3.0) or “off” using the monthly mean Eulerian velocity and
 1242 tracers (Eqn B3.2), is “more” correct in Fig. B2 and Table B1. It is likely that for gates
 1243 where these two methods provide almost identical estimates (e.g., Bering, Davis and Fram
 1244 Straits) we have higher confidence in our estimated FW transport. Across the CAA and
 1245 the GSR the FW transport calculation depends strongly on the method employed and
 1246 caution should be used in confidently reporting FW fluxes and comparing between dif-
 1247 ferent studies.

Gate	FW Transports [mSv]	
(1) Bering Strait	^a 61.32 ± 23.82	^b 54.24 ± 20.62
(2) CAA	372.06 ± 109.98	-94.19 ± 31.60
(3) Fram Strait	-96.56 ± 34.85	-84.83 ± 23.29
(4) Svalbard-FJL ¹ -SZ ²	14.60 ± 43.37	45.23 ± 31.14
(5) Barents Sea Opening	-30.15 ± 38.18	-3.25 ± 3.30
(6) Davis Strait	-133.47 ± 26.66	-103.32 ± 19.59
(7) Denmark Strait	153.85 ± 106.71	-42.61 ± 12.21
(8) Iceland-Faroe	297.85 ± 178.35	-0.29 ± 0.69
(9) Faroe-Shetland	-53.61 ± 64.84	6.25 ± 4.29
(10) Newfoundland-Gr	-441.55 ± 242.66	-110.67 ± 23.44
(11) 48.3°N	-119.30 ± 38.67	-111.60 ± 22.80

Table B1. *ASTER1* Transports of freshwater ($S_r=34.8$ psu) for the combined ocean and ice system for the period 2006–2017. FW fluxes are estimated using ^aEqn B3.0 and ^bEqn B3.2. ¹ Franz Josef Land, ² Severnaya Zemlya.

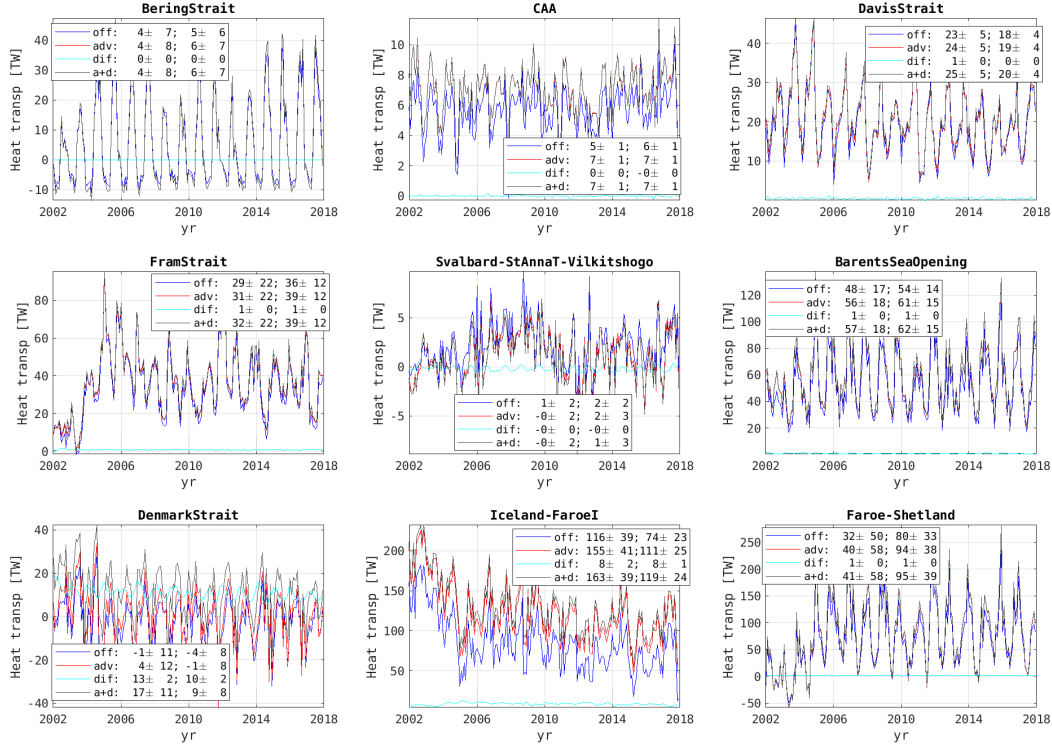


Figure B1. Time series of ocean heat transports (assuming a reference potential temperature $\theta_r=0$) across important Arctic Mediterranean gateways using online (Eqn B2.0) and offline methods (“off”, Eqn B2.2), with the latter using outputs of monthly-averaged Eulerian velocity $\langle \mathbf{u}_E \rangle$ and potential temperature $\langle \theta \rangle$. “adv” and “dif” are online calculations of the advective ($F_{H\theta,adv}$) and diffusive ($F_{H\theta,dif}$) terms for ocean transports on the RHS of Eqn B2.0, and their sum is given by “a+d”. The quantities listed in the legend are the 2002–2006 and 2007–2017 means and month-to-month variability. The variability is computed after the seasonal cycle has been removed. As explained in the main text, statistics are reported separately for these two periods due to large observed changes in the Arctic around 2006/2007.

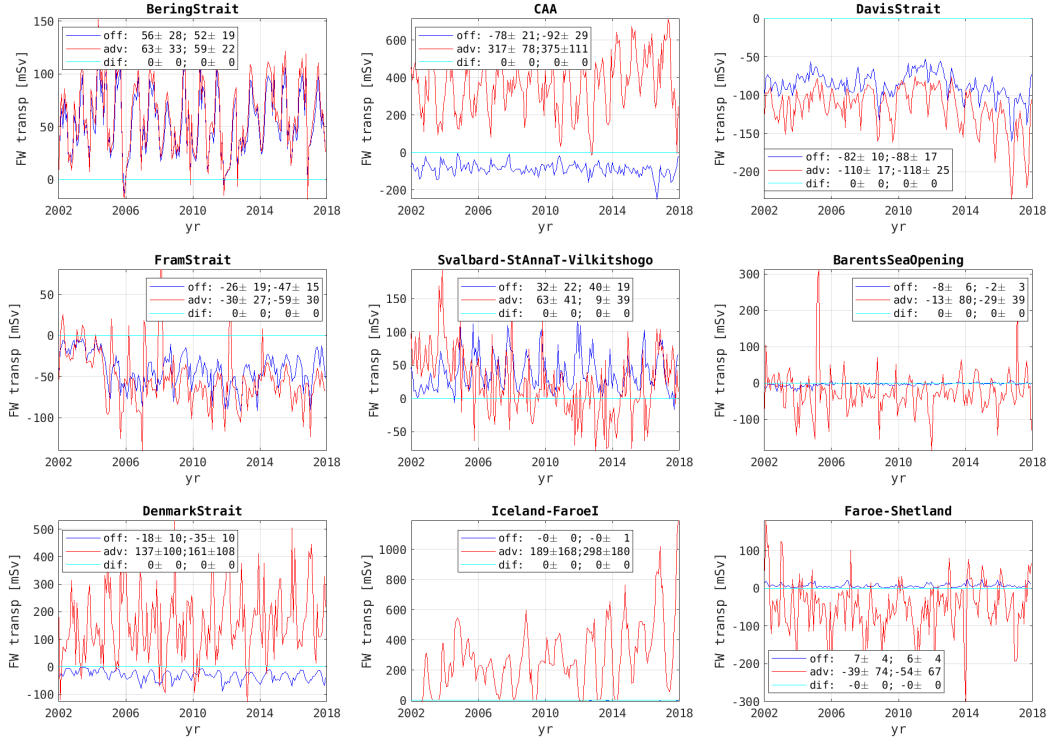


Figure B2. Time series of ocean freshwater transports (assuming a reference salinity $S_r = 34.8$) across important Arctic Mediterranean gateways using online (Eqn B3.0) and offline (Eqn B3.2) methods. Both methods incur errors due to reliance of the monthly $\langle S \rangle$ for determining the depth of the reference isohaline z_{S_r} serving as the integral limit. “off” refers to Eqn B3.2 which computes the transport offline using outputs of monthly-averaged Eulerian velocity $\langle \mathbf{u}_E \rangle$ and salinity $\langle S \rangle$. “adv” and “dif” are the approximated online calculations of advective ($FW_{S,adv}$) and diffusive ($FW_{S,dif}$) terms on the RHS of Eqn B3.0. The quantities listed in the legend are the 2002–2006 and 2007–2017 means and month-to-month variability. The variability is computed after the seasonal cycle has been removed. Note that “adv” is consistently larger than “off” (and with larger variability), but it is not possible to conclude that the online calculation is superior due to imperfect treatment of z_{S_r} . Instead, we assume higher confidence in both our FW flux estimation and our FW flux comparisons where “adv” and “off” converge.

Appendix C Watermass definition in *ASTE_R1*

Suitable specification of the characteristic salinity, potential temperature and density (S , θ , σ) defining known watermasses can differ between observations and models due to model biases, as shown in Fig. 13 in the main text for water properties in the Irminger and Labrador Seas. Watermasses can be clearly identified in *ASTE_R1* as large volumes with a common formation history and distinct properties from surrounding waters, consistent with their definition in the literature. However in regions of hydrographic bias, these watermasses will not be identified - or correctly quantified - as their observed counterparts if they are tracked following the observed values too strictly. In this appendix, we summarize the choices made in determining watermass and explore the sensitivity to these choices where appropriate.

C1 Volume transports of watermass

Table. C1 lists the watermass properties at Fram Strait (FS) and across the Greenland-Scotland Ridge (GSR) used to identify the transports reported in Fig. 14 in the main text. At the FS, the mean transports can be decomposed approximately into the West Spitsbergen Current (WSC, east of 5°E , Beszczynska-Möller et al., 2012), recirculated Atlantic Water (AW) (between 3.2°W and 5°E), and the East Greenland Current (EGC, west of 3.2°W , $S \leq 34$ psu, $T \leq 1^\circ\text{C}$). At the GSR definitions of watermasses such as the surface outflow, dense outflow, modified water, and inflow AW from Østerhus et al. (2019) and Hansen and Østerhus (2000) can be problematic when strictly applied to grid-scale average quantities. For example, the densewater in the outflow through Denmark Strait (DS) is defined in Østerhus et al. (2019) as having density anomaly $\sigma_\theta > 27.8$, but in *ASTE_R1* outflow at the lowest depths of the strait are characterized by a lower bound of σ_θ ranging between 27.28 and 27.81. For this range, the corresponding southward transports are -1.6 ± 0.9 to 0.5 ± 0.3 Sv (see Fig. 14, blue color text). Similarly, over the Iceland-Faroe (IF) ridge, the southward transports of densewater defined by $\sigma_\theta \geq 22.44$ or $\sigma_\theta \geq 27.55$ in *ASTE_R1* yield a range of -0.4 to -0.3 Sv, compared to -0.4 ± 0.3 Sv of water with $\sigma_\theta \geq 27.8$ in Østerhus et al. (2019). Similar considerations applied also to dense water properties at the Faroe-Shetland (FSh) ridge ($\sigma_\theta \geq 27.81$ in *ASTE_R1* compared to 27.8 in Østerhus et al., 2019). For the northward flow, in addition to salinity thresholds ($S \geq [34.8, 35, 35.25]$ psu), temperature thresholds of $\theta \geq [5, 4, 5]^\circ\text{C}$ are used in *ASTE_R1* to identify the warm AW across the DS, IF, and FSh channels.

C2 Heat content of upper halocline watermass

The upper halocline watermass, defined by Timmermans et al. (2018) as a layer within lower and upper salinity bounds of $S_l=31.0$ psu and $S_u=33.0$ psu, respectively, was identified based on subsurface in situ observations with fine vertical sampling resolution. In *ASTE_R1*, with vertical grid spacing of 15–20 m within the water column depths 50–160 m, average salinity in the water column changes more abruptly than in the observations. For more accurate estimation of halocline-integrated quantities one approach is to “interpolate” the salinity in the vertical to a finer grid to find the exact depths at which salinity fits within the given bounds. Though this is often done during model-data comparisons (e.g., Grabon, 2020), the interpolation introduces additional information that was not strictly solved for by the model. An alternate approach is to vary the salinity bounds to gauge the sensitivity of the heat content within this watermass to the vertical discretization in the model. As an example, Fig. C1 shows a vertical section in *ASTE_R1* through the Beaufort Gyre region as defined in Timmermans et al. (2018), with the watermass bounded between a temperature maximum at depths ~ 50 – 60 m (Pacific Summer Water, PSW, $S_l=31$ salinity contour) and a temperature minimum at depths ~ 150 m (Pacific Winter Water, PWW, $S_u=33$). In *ASTE_R1*, negligible sensitivity is found with changes to S_u , but the heat content within the upper halocline in this region

Gate	Watermass	Properties		Reference
		Obs	ASTE	
FS	WSC	$\text{lon} > 5^\circ\text{E}$, $T \geq 2^\circ\text{C}$, $\sigma_\theta \sim 27.97 \text{ kg/m}^3$	$\text{lon} \geq 4^\circ\text{E}$, $T \geq 2^\circ\text{C}$	Beszczynska-Möller et al. (2012), Schauer and Beszczynska-Möller (2009)
	Recirc AW	$-2.5^\circ\text{E} < \text{lon} < 5^\circ\text{E}$	$-3.2^\circ\text{E} < \text{lon} < 4^\circ\text{E}$, $T \geq 1^\circ\text{C}$, $S > 34 \text{ psu}$	Beszczynska-Möller et al. (2012)
	deep AW	$\text{lon} < -3^\circ\text{E}$	$-3.2^\circ\text{E} < \text{lon} < 4^\circ\text{E}$, $T < 1^\circ\text{C}$, $S > 34 \text{ psu}$	Beszczynska-Möller et al. (2012)
	return flow		$\text{lon} < -3.2^\circ\text{E}$	
	EGC	$\text{lon} < -1^\circ\text{E}$	$S < 34 \text{ psu}$, $T \leq 1^\circ\text{C}$	de Steur et al. (2014)
DS	inflow AW	–	$S > 34.8 \text{ psu}$, $T > 5$	
	dense outflow	$\sigma_\theta > 27.8 \text{ kg/m}^3$	$S > 34.5, 34.8 \text{ psu}$, $T < 3.5^\circ\text{C}$, $\sigma_\theta > 27.44, 27.81 \text{ kg/m}^3$	Østerhus et al. (2019)
	surface outflow	$\sigma_\theta < 27.8 \text{ kg/m}^3$	$S \leq 34.5 \text{ psu}$	
IF	inflow AW	–	$S > 35 \text{ psu}$, $T > 5^\circ\text{C}$	
	dense outflow	$\sigma_\theta > 27.8 \text{ kg/m}^3$	$35 \geq S > 34.5, 34.7 \text{ psu}$, $T \leq 4, 5^\circ\text{C}$, $\sigma_\theta > 27.44, 27.55 \text{ kg/m}^3$	Østerhus et al. (2019)
FSh	inflow AW	–	$S > 35.25 \text{ psu}$, $T > 5^\circ\text{C}$, $\sigma_\theta > 27.87 \text{ kg/m}^3$	Østerhus et al. (2019)
	dense outflow	$\sigma_\theta > 27.8 \text{ kg/m}^3$	$35 \geq S > 34.8 \text{ psu}$, $T \leq 2^\circ\text{C}$, $\sigma_\theta > 27.81, 27.97 \text{ kg/m}^3$	

Table C1. Watermass at important Arctic Mediterranean gateway defined based on observations and in *ASTE_R1*.

1299
1300
1301

changes by approximately 1–2.5% per 0.1 psu change in S_l . A change in S_l of ~ 0.5 psu corresponds approximately to one depth level in *ASTE_R1*, and the heat content change associated with this is shown in shade in Fig. 17 in the main text.

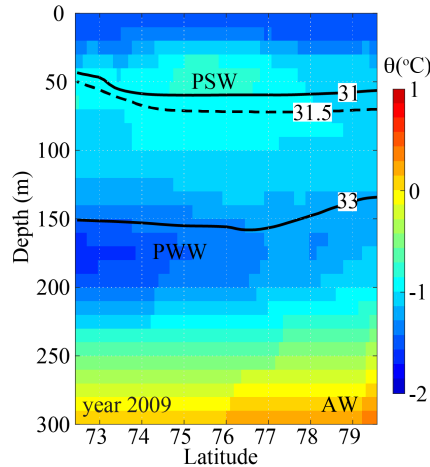


Figure C1. Vertical mean temperature for the year 2009 in a section across the Beaufort Gyre. Salinity contours are shown in black with white label, with the upper halocline watermass defined based on Timmermans et al. (2018) as bounded by $S_l=31$ psu (through the temperature maximum associated with the Pacific Summer Water PSW) and $S_u=33$ psu (through the temperature minimum associated with the Pacific Winter Water PWW). A change of S_l by 0.5 psu corresponds approximately to 1 vertical depth level change in *ASTE_R1*.

Acknowledgments

1302

1303

1304

1305

1306

1307

1308

1309

1310

1311

1312

1313

1314

1315

This work was supported by NSF-OPP-1603903, NSF-OPP-1708289, and NSF-OCE-1924546. Additional funding was provided from the ECCO project through a JPL/Caltech subcontract. Computing resources were provided by the University of Texas at Austin Texas Advanced Computing Center (TACC) and NASA Advanced Supercomputing Division at the Ames Research Center. Adjoint code was generated using the TAF software tool, created and maintained by FastOpt GmbH (<http://www.fastopt.com/>). The *ASTE_R1* model configuration, inputs, and monthly outputs are available at <https://web.corral.tacc.utexas.edu/OceanProjects/ASTE/> and Amazon Web Services provided by TACC at <http://aste-release1.s3-website.us-east-2.amazonaws.com/>. Author ATN thanks M.-L. Timmermans and N. Foukal for providing heat content time-series for the Arctic halocline and eastern SPNA, and W. von Appen for the 2012–2017 processed Fram Strait mooring data used for *ASTE* post validation.

References

1316

1317

1318

1319

1320

1321

1322

1323

1324

1325

1326

1327

1328

- Abernathey, R., Busecke, J., Smith, T., Bot, S., Banihirwe, A., Zhang, C., . . . Rath, W. (2020, October). *xgcm/xgcm: v0.5.1*. Zenodo. Retrieved from <https://doi.org/10.5281/zenodo.4097223> doi: 10.5281/zenodo.4097223
- Abernathey, R., raphael dussin, Smith, T., Bot, S., Cimatoribus, A., Doddridge, E., . . . Leskis, A. (2019, July). *xgcm/xmitgcm: v0.4.1*. Zenodo. Retrieved from <https://doi.org/10.5281/zenodo.3332699> doi: 10.5281/zenodo.3332699
- Abernathey, R. P., Cerovecki, I., Holland, P. R., Newsom, E., Mazloff, M., & Talley, L. D. (2016). Water-mass transformation by sea ice in the upper branch of the Southern Ocean overturning. *Nature Geoscience*. doi: 10.1038/NGEO2749
- Adcroft, A., & Campin, J.-M. (2004). Rescaled height coordinates for accurate representation of free-surface flows in ocean circulation models. *Ocean Modelling*, 7(2004), 269–284. doi: 10.1016/j.ocemod.2003.09.003

- 1329 Adcroft, A., Campin, J.-M., Dutkiewicz, S., Evangelinos, C., Ferreira, D., Forget, G.,
1330 ... Molod, A. (2018). *MITgcm user manual*. doi: 1721.1/117188
- 1331 Adcroft, A., Campin, J.-M., Hill, C., & Marshall, J. (2004). Implementation of an
1332 atmosphere-ocean general circulation model on the expanded spherical cube.
1333 *Mon. Wea. Rev.*, *132*(12), 2845–2863.
- 1334 Adcroft, A., Hill, C., & Marshall, J. (1997). Representation of topography by shaved
1335 cells in a height coordinate ocean model. *Mon. Wea. Rev.*, *125*, 2293–2315.
- 1336 Adler, R., Sapiano, M. R. P., Huffman, G. J., Wang, J.-J., Gu, G., Bolvin, D., ...
1337 Shin, D.-B. (2018). The Global Precipitation Climatology Project (GPCP)
1338 Monthly Analysis (New Version 2.3) and a Review of 2017 Global Precipita-
1339 tion. *Atmosphere*, *9*(138). doi: <https://doi.org/10.3390/atmos9040138>
- 1340 Antonov, J. I., Seidov, D., Boyer, T. P., Locarnini, R. A., Mishonov, A. V., Garcia,
1341 H. E., ... Johnson, D. R. (2010). Volume 2: Salinity. In S. Levitus (Ed.), .
1342 NOAA Atlas NESDIS 68, U.S. Government Printing Office, Washington, D.C.
- 1343 Årthun, M., & Eldevik, T. (2016). On anomalous ocean heat transport toward the
1344 Arctic and associated climate predictability. *J. Clim.*, *29*, 689–704. doi: 10
1345 .1175/JCLI-D-15-0448.1
- 1346 Asbjørnsen, H., Årthun, M., Skagseth, Ø., & Eldevik, T. (2019). Mechanisms of
1347 ocean heat anomalies in the norwegian sea. *Journal of Geophysical Research:*
1348 *Oceans*, *124*(4), 2908-2923. Retrieved from <https://agupubs.onlinelibrary>
1349 [.wiley.com/doi/abs/10.1029/2018JC014649](https://doi.org/10.1029/2018JC014649) doi: 10.1029/2018JC014649
- 1350 Bamber, J. L., Tedstone, A. J., King, M. D., Howat, I. M., Enderlin, E. M., van den
1351 Broeke, M. R., & Noel, B. (2018). Land ice freshwater budget of the Arc-
1352 tic and North Atlantic Oceans: 1. Data, methods, and results. *Journal of*
1353 *Geophysical Research*, *123*, 1827–1837. doi: 10.1002/2017JC013605
- 1354 Bamber, J. L., van den Broeke, M., Ettema, J., Lenaerts, J., & Rignot, E. (2012).
1355 Recent large increases in freshwater fluxes from greenland into the North At-
1356 lantic. *Geophys. Res. Lett.*, *39*. doi: 10.1029/2012GL052552
- 1357 Baringer, M. O., & Larsen, J. C. (2001). Sixteen years of Florida Current transport
1358 at 27°N. *Geophys. Res. Lett.*, *28*(16), 3179–3182. doi: 10.1029/2001GL013246
- 1359 Bauch, D., Dmitrenko, I. A., Wegner, C., Hölemann, J., Kirillov, S. A., Timokhov,
1360 L. A., & Kassens, H. (2009). Exchange of laptev sea and arctic ocean halocline
1361 waters in response to atmospheric forcing. *J. Geophys. Res.*, *114*(C05008).
1362 (doi:10.1029/2008JC005062)
- 1363 Bauch, D., van der Loeff, M. R., Andersen, N., Torres-Valdes, S., Bakker, K., &
1364 Abrahamsen, E. (2011). Origin of freshwater and polynya water in the arctic
1365 ocean halocline in summer 2007. *Progress in Oceanography*, *91*, 482–495.
1366 (doi:10.1016/j.pocean.2011.07.017)
- 1367 Baumann, T. M., Polyakov, I. V., Pnyushkov, A. V., Rember, R., Ivanov, V. V.,
1368 Alkire, M. B., ... Carmack, E. C. (2018, 06). On the seasonal cycles observed
1369 at the continental slope of the eastern Eurasian Basin of the Arctic Ocean.
1370 *Journal of Physical Oceanography*, *48*(7), 1451-1470. Retrieved from <https://>
1371 doi.org/10.1175/JPO-D-17-0163.1 doi: 10.1175/JPO-D-17-0163.1
- 1372 Beard, N. L., Straneo, F., & Jenkins, W. (2018). Export of strongly diluted Green-
1373 land meltwater from a major glacial fjord. *Geophysical Research Letters*, *45*,
1374 4163–4170. doi: 10.1029/2018GL077000
- 1375 Bebieva, Y., & Timmermans, M.-L. (2016). An examination of double-diffusive
1376 processes in a mesoscale eddy in the Arctic Ocean. *Journal of Geophysical Re-*
1377 *search*, *121*, 457–475. doi: 10.1002/2015JC011105
- 1378 Beesley, J. A., Bretherton, C. S., Jakob, C., Andreas, E. L., Intrieri, J. M., & Ut-
1379 tal, T. A. (2000). A comparison of cloud and boundary layer variables in
1380 the ECMWF forecast model with observations at Surface Heat Budget of the
1381 Arctic Ocean (SHEBA) ice camp. *J. Geophys. Res.*, *105*(D10), 12337–12349.
- 1382 Beszczynska-Möller, A., Fahrbach, E., Schauer, U., & Hansen, E. (2012). Vari-
1383 ability in Atlantic water temperature and transport at the entrance to

- 1384 the Arctic Ocean, 1997–2010. *ICES Journal of Marine Science*. doi:
1385 10.1093/icesjms/fss056
- 1386 Beszczynska-Möller, A., Woodgate, R. A., Lee, C., Melling, H., & Karcher, M.
1387 (2011). A synthesis of exchanges through the main oceanic gateways to the
1388 Arctic Ocean. *Oceanography*, *24*(3), 82–99. doi: [http://dx.doi.org/10.5670/](http://dx.doi.org/10.5670/oceanog.2011.59)
1389 [oceanog.2011.59](http://dx.doi.org/10.5670/oceanog.2011.59)
- 1390 Bigdeli, A., Nguyen, A. T., Pillar, H. R., Ocana, V., & Heimbach, P. (2020). Atmo-
1391 spheric warming drives growth in Arctic sea-ice: A key role for snow. *Geophys-*
1392 *ical Research Letters*. (submitted)
- 1393 Buckley, M. W., Ponte, R. M., Forget, G., & Heimbach, P. (2014). Low-frequency
1394 SST and upper-ocean heat content variability in the North Atlantic. *J. Cli-*
1395 *mate*, *27*(13), 4996–5018. doi: 10.1175/JCLI-D-13-00316.1
- 1396 Buckley, M. W., Ponte, R. M., Forget, G., & Heimbach, P. (2015). Determining
1397 the origins of advective heat transport convergence variability in the North
1398 Atlantic. *J. Climate*, *28*, 3943–3956. doi: 10.1175/JCLI-D-14-00579.1
- 1399 Campin, J.-M., Adcroft, A., Hill, C., & Marshall, J. (2004). Conservation of proper-
1400 ties in a free-surface model. *Ocean Modelling*, *6*, 221–244. doi: 10.1016/S1463
1401 -5003(03)00009-X
- 1402 Carmack, E. C., Yamamoto-Kawai, M., Haine, T. W. N., Bacon, S., Bluhm, B. A.,
1403 Lique, C., . . . Williams, W. J. (2016). Freshwater and its role in the Arctic
1404 marine system: Sources, disposition, storage, export, and physical and biogeo-
1405 chemical consequences in the Arctic and global oceans. *Journal of Geophysical*
1406 *Research: Biogeosciences*, *121*(3), 675–717. doi: 10.1002/2015JG003140
- 1407 Carton, J. A., Penny, S. G., & Kalnay, E. (2019, 04). Temperature and salinity
1408 variability in the SODA3, ECCO4r3, and ORAS5 ocean reanalyses, 1993–2015.
1409 *Journal of Climate*, *32*(8), 2277–2293. Retrieved from [https://doi.org/](https://doi.org/10.1175/JCLI-D-18-0605.1)
1410 [10.1175/JCLI-D-18-0605.1](https://doi.org/10.1175/JCLI-D-18-0605.1) doi: 10.1175/JCLI-D-18-0605.1
- 1411 Chassignet, E. P., & Garraffo, Z. D. (2001). Viscosity parameterization and the Gulf
1412 Stream separation. In P. Muller & D. Henderson (Eds.), *From stirring to mix-*
1413 *ing in a stratified ocean* (pp. 37–41).
- 1414 Chassignet, E. P., & Marshall, D. P. (2013). Gulf stream separation in numerical
1415 ocean models. In *Ocean modeling in an eddying regime* (p. 39-61). American
1416 Geophysical Union (AGU). doi: 10.1029/177GM05
- 1417 Chassignet, E. P., & Xu, X. (2017). Impact of horizontal resolution ($1/12^\circ$ to $1/50^\circ$)
1418 on Gulf Stream separation, penetration, and variability. *Journal of Physical*
1419 *Oceanography*, *47*, 1999–2021. doi: 10.1175/JPO-D-17-0031.1
- 1420 Chaudhuri, A. H., Ponte, R. M., Forget, G., & Heimbach, P. (2013). A Comparison
1421 of Atmospheric Reanalysis Surface Products over the Ocean and Implications
1422 for Uncertainties in Air–Sea Boundary Forcing. *J. Climate*, *26*(1), 153–170.
1423 doi: 10.1175/JCLI-D-12-00090.1
- 1424 Chaudhuri, A. H., Ponte, R. M., & Nguyen, A. T. (2014). A comparison of
1425 atmospheric reanalysis products for the Arctic Ocean and implications
1426 for uncertainties in air–sea fluxes. *J. Climate*, *27*(14), 5411–5421. doi:
1427 [10.1175/JCLI-D-13-00424.1](https://doi.org/10.1175/JCLI-D-13-00424.1)
- 1428 Cole, S. T., Timmermanns, M.-L., Toole, J. M., Krishfield, R. A., & Thwaites, F. T.
1429 (2014). Ekman veering, internal waves, and turbulence observed under Arctic
1430 sea ice. *J. Phys. Oceanogr.*, *44*, 1306–1328.
- 1431 Curry, B., Lee, C., & Petrie, B. (2011). Volume, freshwater, and heat fluxes through
1432 Davis Strait, 2004–05. *Journal of Physical Oceanography*, *41*, 429–436. doi: 10
1433 .1175/2010JPO4536.1
- 1434 Curry, B., Lee, C., Petrie, B., Moritz, R. E., & Kwok, R. (2014). Multiyear volume,
1435 liquid freshwater, and sea ice transports through Davis Strait, 2004–10. *Jour-*
1436 *nal of Physical Oceanography*, *44*, 1244–1266. doi: 10.1175/JPO-D-13-0177.1
- 1437 Dee, D. P., Uppala, S. M., Simmons, A. J., Berrisford, P., Poli, P., Kobayashi, S., . . .
1438 Vitart, F. (2011). The ERA-Interim reanalysis: configuration and performance

- of the data assimilation system. *Q. J. R. Meteorol. Soc.*, *137*(656), 553–597.
- 1440 Dengg, J. (1993). The problem of Gulf Stream separation: A barotropic ap-
 1441 proach. *Journal of Physical Oceanography*, *23*(10), 2182–2200. doi:
 1442 10.1175/1520-0485(1993)023<2182:TPOGSS>2.0.CO;2
- 1443 de Steur, L., Hansen, E., Gerdes, R., Karcher, M., Fahrbach, E., & Holfort, J.
 1444 (2009). Freshwater fluxes in the East Greenland current: A decade of ob-
 1445 servations. *Geophys. Res. Lett.*, *36*(L23611). doi: 10.1029/2009GL041278
- 1446 de Steur, L., Hansen, E., Mauritzen, C., Beszczynska-Möller, A., & Fahrbach, E.
 1447 (2014). Impact of recirculation on the East Greenland Current in Fram Strait:
 1448 Results from moored current meter measurements between 1997 and 2009.
 1449 *Deep Sea Res.*, *92*, 26–40. doi: 10.1016/j.dsr.2014.05.018
- 1450 de Steur, L., Peralta Ferriz, C., & Pavlova, O. (2018). Freshwater export in the East
 1451 Greenland Current freshens the North Atlantic. *Geophysical Research Letters*,
 1452 *45*(24), 13359–13366. doi: 10.1029/2018GL080207
- 1453 Dmitrenko, I. A., Ivanov, V. V., Kirillov, S. A., Vinogradova, E. L., Torres-Valdes,
 1454 S., & Bauch, D. (2011). Properties of the Atlantic derived halocline waters
 1455 over the Laptev Sea continental margin: Evidence from 2002 to 2009. *J. Geo-
 1456 phys. Res.*, *116*(C10024). doi: 10.1029/2011JC007269
- 1457 Dmitrenko, I. A., Kirillov, S. A., Ivanov, V. V., Woodgate, R. A., Polyakov, I. V.,
 1458 Koldunov, N., ... Timokhov, L. A. (2009). Seasonal modification of the
 1459 Arctic Ocean intermediate water layer off the eastern Laptev Sea continental
 1460 shelf break. *Journal of Geophysical Research: Oceans*, *114*(C6). Retrieved
 1461 from [https://agupubs.onlinelibrary.wiley.com/doi/abs/10.1029/
 1462 2008JC005229](https://agupubs.onlinelibrary.wiley.com/doi/abs/10.1029/2008JC005229) doi: 10.1029/2008JC005229
- 1463 Docquier, D., Grist, J. P., Roberts, M. J., Roberts, C. D., Semmler, T., Ponsoni,
 1464 L., ... Fichet, T. (2019). Impact of model resolution on Arctic sea ice and
 1465 North Atlantic Ocean heat transport. *Climate Dynamics*, *53*, 4989–5017. doi:
 1466 10.1007/s00382-019-04840-y
- 1467 Drange, H., Gerdes, R., Gao, Y., Karcher, M., Kauker, F., & Bentsen, M. (2005).
 1468 Ocean general circulation modelling of the Nordic Seas. In H. Drange,
 1469 T. Dokken, T. Furevik, R. Gerdes, & W. Berger (Eds.), *From the Nordic
 1470 Seas: An integrated perspective* (Vol. 158, pp. 199–220). American Geophysical
 1471 Union, Washington DC: AGU Monograph.
- 1472 Dukhovskoy, D. S., Myers, P. G., Platov, G., Timmermans, M.-L., Curry, B.,
 1473 Proshutinsky, A., ... Somavilla, R. (2016). Greenland freshwater pathways in
 1474 the sub-Arctic seas from model experiments with passive tracers. *Journal of
 1475 Geophysical Research: Oceans*, *121*(1), 877–907. doi: 10.1002/2015JC011290
- 1476 Dukhovskoy, D. S., Yashayaev, I., Proshutinsky, A., Bamber, J. L., Bashmach-
 1477 nikov, I. L., Chassignet, E. P., ... Tedstone, A. J. (2019). Role of Green-
 1478 land freshwater anomaly in the recent freshening of the subpolar North At-
 1479 lantic. *Journal of Geophysical Research: Oceans*, *124*(5), 3333–3360. doi:
 1480 10.1029/2018JC014686
- 1481 Ezer, T. (2016). Revisiting the problem of the Gulf Stream separation: on the repre-
 1482 sentation of topography in ocean models with different types of vertical grids.
 1483 *Ocean Modelling*, *104*, 15–27. doi: 10.1016/j.ocemod.2016.05.008
- 1484 Fahrbach, E., Meincke, J., Osterhus, S., Rohardt, G., Schauer, U., Tverberg, V., &
 1485 Verduin, J. (2001). Direct measurements of volume transports through Fram
 1486 Strait. *Polar Research*, *20*(2), 217–224.
- 1487 Fenty, I., & Heimbach, P. (2013a). Coupled Sea Ice–Ocean–State Estimation in the
 1488 Labrador Sea and Baffin Bay. *J. Phys. Oceanogr.*, *43*(5), 884–904. doi: 10
 1489 .1175/JPO-D-12-065.1
- 1490 Fenty, I., & Heimbach, P. (2013b). Hydrographic preconditioning for seasonal sea
 1491 ice anomalies in the Labrador sea. *J. Phys. Oceanogr.*, *43*(5), 863–883. doi: 10
 1492 .1175/JPO-D-12-064.1
- 1493 Fenty, I., Menemenlis, D., & Zhang, H. (2015). Global coupled sea ice-ocean state

- 1494 estimate. *Clim. Dyn.*. doi: 10.1007/s00382-015-2796-6
- 1495 Fer, I. (2014). Near-internal mixing in the central Arctic Ocean. *J. Phys. Oceanogr.*,
- 1496 *44*, 2031–2049. doi: 10.1175/JPO-D-13-0133.1
- 1497 Forget, G., Campin, J.-M., Heimbach, P., Hill, C. N., Ponte, R. M., & Wunsch, C.
- 1498 (2015). ECCO version 4: an integrated framework for non-linear inverse mod-
- 1499 eling and global ocean state estimation. *Geosci. Model Dev. Discuss.*, *8*(5),
- 1500 3653–3743.
- 1501 Forget, G., Ferreira, D., & Liang, X. (2015). On the observability of turbulent trans-
- 1502 port rates by argo: supporting evidence from an inversion experiment. *Ocean*
- 1503 *Sciences Diss.*, *12*(3), 1107–1143.
- 1504 Forget, G., & Wunsch, C. (2007). Global hydrographic variability and the data
- 1505 weights in ocean state estimates. *J. Phys. Oceanogr.*, *37*, 1997–2008.
- 1506 Foukal, N. P., & Lozier, M. S. (2018). Examining the origins of ocean heat content
- 1507 variability in the eastern North Atlantic subpolar gyre. *Geophysical Research*
- 1508 *Letters*, *45*, 11,275–11,283. doi: <https://doi.org/10.1029/2018GL079122>
- 1509 Fournier, S., Lee, T., Tang, W., Steele, M., & Omeldo, E. (2019). Evaluation and
- 1510 intercomparison of SMOS, Aquarius and SMAP sea surface salinity products
- 1511 in the Arctic Ocean. *Remote Sensing*, *11*(3043). doi: 10.3390/rs11243043
- 1512 Fowler, C., Emery, W., & Tschudi, M. (2013). *Polar pathfinder daily 25 km ease-grid*
- 1513 *sea ice motion vectors. version 2, northern hemisphere* (Tech. Rep.). Boulder,
- 1514 Colorado, USA: National Snow and Ice Data Center. (NSIDC Technical Re-
- 1515 port)
- 1516 Fox-Kemper, B., & Menemenlis, D. (2008). Can large eddy simulation techniques
- 1517 improve mesoscale rich ocean models? In M. W. Hecht & H. Hasumi (Eds.),
- 1518 *Ocean modeling in an eddying regime* (pp. 319–337). Washington, D. C.:
- 1519 American Geophysical Union.
- 1520 Freville, H., Brun, E., Picard, G., Tatarinova, N., Arnaud, L., Lanconelli, C., ...
- 1521 van den Broeke, M. (2014). Using MODIS land surface temperatures and
- 1522 the Crocus snow model to understand the warm bias of ERA-Interim re-
- 1523 analyses at the surface in Antarctica. *The Cryosphere*, *8*, 1361–1373. doi:
- 1524 10.5194/tc-8-1361-2014
- 1525 Fukumori, I., Heimbach, P., Ponte, R. M., & Wunsch, C. (2018). A dynamically con-
- 1526 sistent, multi-variable ocean climatology. *Bulletin of the American Meteorologi-*
- 1527 *cal Society*, *0*(0), null. (in press) doi: 10.1175/BAMS-D-17-0213.1
- 1528 Gent, P. R., & McWilliams, J. C. (1990). Isopycnal mixing in ocean circulation
- 1529 models. *J. Phys. Oceanogr.*, *20*, 150–155.
- 1530 Gerdes, R., Hurlin, W., & Griffies, S. M. (2006). Sensitivity of a global ocean model
- 1531 to increased run-off from Greenland. *Ocean Modelling*, *12*(3–4), 416–435. doi:
- 1532 10.1016/j.ocemod.2005.08.003
- 1533 Germe, A., Houssais, M., Herbaut, C., & Cassou, C. (2011). Greenland Sea sea ice
- 1534 variability over 1979–2007 and its link to the surface atmosphere. *J. Geophys.*
- 1535 *Res.*, *116*(C10034). doi: 10.1029/2011JC006960
- 1536 Giering, R., Kaminski, T., & Slawig, T. (2005, October). Generating efficient deriva-
- 1537 tive code with TAF. *Future Generation Computer Systems*, *21*(8), 1345–1355.
- 1538 Gopalakrishnan, G., Cornuelle, B. D., Hoteit, I., Rudnick, D. L., & Owens, W. B.
- 1539 (2013). State estimates and forecasts of the loop current in the Gulf of Mexico
- 1540 using the MITgcm and its adjoint. *Journal of Geophysical Research: Oceans*,
- 1541 *118*(7), 3292–3314. doi: 10.1002/jgrc.20239
- 1542 Grabon, J. S. (2020). *An analysis of Atlantic Water in the Arctic Ocean using the*
- 1543 *Arctic Subpolar gyre sTate Estimate and observations* (Unpublished master’s
- 1544 thesis). Massachusetts Institute of Technology, Cambridge, MA, USA. (90pp)
- 1545 Griffies, S. M. (2004). *Fundamentals of ocean climate models*. Princeton, NJ: Prince-
- 1546 ton University Press. (518pp)
- 1547 Haine, T. W. N., Curry, B., Gerdes, R., Hansen, E., Karcher, M., Lee, C., ...
- 1548 Woodgate, R. A. (2015). Arctic freshwater export: Status, mechanisms, and

- 1549 prospects. *Global Planet. Change*, *125*, 13–35. doi: [https://doi.org/10.1016/](https://doi.org/10.1016/j.gloplacha.2014.11.013)
 1550 [j.gloplacha.2014.11.013](https://doi.org/10.1016/j.gloplacha.2014.11.013)
- 1551 Hansen, B., Larsen, K. M. H., Hátún, H., Kristiansen, R., Mortensen, E., & Øster-
 1552 hus, S. (2015). Transport of volume, heat, and salt towards the Arctic in the
 1553 Faroe Current 1993–2013. *Ocean. Sci.*, *11*, 743. doi: [https://doi.org/10.5194/](https://doi.org/10.5194/os-11-743-2015)
 1554 [os-11-743-2015](https://doi.org/10.5194/os-11-743-2015)
- 1555 Hansen, B., & Østerhus, S. (2000). North Atlantic–Nordic Seas exchanges. *Progress*
 1556 *in Oceanography*, *45*(2), 198–208. doi: [https://doi.org/10.1016/S0079-6611\(99\)](https://doi.org/10.1016/S0079-6611(99)00052-X)
 1557 [00052-X](https://doi.org/10.1016/S0079-6611(99)00052-X)
- 1558 Hattermann, T., Isachsen, P. E., Appen, W.-J., Albretsen, J., & Sundfjord, A.
 1559 (2016, April). Eddy-driven recirculation of Atlantic Water in Fram Strait.
 1560 *Geophysical Research Letters*, *43*(7), 3406–3414.
- 1561 Heimbach, P., Fukumori, I., Hill, C. N., Ponte, R. M., Stammer, D., Wunsch, C., ...
 1562 Zhang, H. (2019, March). Putting It All Together: Adding Value to the Global
 1563 Ocean and Climate Observing Systems With Complete Self-Consistent Ocean
 1564 State and Parameter Estimates. *Frontiers in Marine Science*, *6*, 769–10.
- 1565 Heimbach, P., Hill, C., & Giering, R. (2005). An efficient exact adjoint of the
 1566 parallel MIT general circulation model, generated via automatic differen-
 1567 tiation. *Future Generation Computer Systems*, *21*(8), 1356–1371. doi:
 1568 [10.1016/j.future.2004.11.010](https://doi.org/10.1016/j.future.2004.11.010)
- 1569 Heimbach, P., Menemenlis, D., Losch, M., Campin, J.-M., & Hill, C. (2010). On
 1570 the formulation of sea-ice models. Part 2: Lessons from multi-year adjoint
 1571 sea-ice export sensitivities through the Canadian Arctic Archipelago. *Ocean*
 1572 *Modelling*, *33*(1-2), 145–158. doi: [10.1016/j.ocemod.2010.02.002](https://doi.org/10.1016/j.ocemod.2010.02.002)
- 1573 Heuzé, C., & Årthun, M. (2019). The Atlantic inflow across the Greenland-Scotland
 1574 ridge in global climate models (CMIP5). *Elem. Sci. Anth.*, *7*(16). doi: [https://](https://doi.org/10.1525/elementa.354)
 1575 doi.org/10.1525/elementa.354
- 1576 Holloway, G., Dupont, F., Golubeva, E., Hakkinen, S., Hunke, E., Jin, M., ...
 1577 Zhang, J. (2007). Water properties and circulation in arctic ocean models.
 1578 *J. Geophys. Res.*, *112*(C04S03). doi: [10.1029/2006JC003642](https://doi.org/10.1029/2006JC003642)
- 1579 Ilicak, M., Drange, H., Wang, Q., Gerdes, R., Aksenov, Y., Bailey, D., ... Yeager,
 1580 S. G. (2016). An assessment of the Arctic Ocean hydrography in a suite of
 1581 interannual CORE-II simulations. part III: Hydrography and fluxes. *Ocean*
 1582 *Modelling*, *100*, 141–161. doi: [10.1016/j.ocemod.2016.02.004](https://doi.org/10.1016/j.ocemod.2016.02.004)
- 1583 Ivanov, V. V., Alexeev, V. A., Repina, I., Koldunov, N. V., & Smirnov, A. (2012).
 1584 Tracing Atlantic water signature in the Arctic sea ice cover east of Svalbard.
 1585 *Advances in Meteorology*, *2012*. doi: [10.1155/2012/201818](https://doi.org/10.1155/2012/201818)
- 1586 Jackson, J. M., Carmack, E. C., McLaughlin, F. A., Allen, S. E., & Ingram, R. G.
 1587 (2010). Identification, characterization, and change of the near-surface
 1588 temperature maximum in the Canada Basin, 1993–2008. *J. Geophys. Res.*,
 1589 *115*(C05021). doi: [10.1029/2009JC005265](https://doi.org/10.1029/2009JC005265)
- 1590 Jahn, A., Aksenov, Y., de Cuevas, B. A., de Steur, L., Häkkinen, S., Hansen, E.,
 1591 ... Zhang, J. (2012). Arctic ocean freshwater: How robust are model
 1592 simulations? *Journal of Geophysical Research: Oceans*, *117*(C8). doi:
 1593 [10.1029/2012JC007907](https://doi.org/10.1029/2012JC007907)
- 1594 Jakobson, E., Vihma, T., Palo, T., Jakobson, L., Keemik, H., & Jaagus, J. (2012).
 1595 Validation of atmospheric reanalyses over the central Arctic Ocean. *Geophys.*
 1596 *Res. Lett.*, *39*(L10802). doi: [10.1029/2012GL051591](https://doi.org/10.1029/2012GL051591)
- 1597 Jakobsson, M., Mayer, L. A., Coakley, B., Dowdeswell, J. A., Forbes, S., Fridman,
 1598 B., ... Weatherall, P. (2012). The International Bathymetric Chart of the
 1599 Arctic Ocean (IBCAO) Version 3.0. *Geophysical Research Letters*. doi:
 1600 [10.1029/2012GL052219](https://doi.org/10.1029/2012GL052219)
- 1601 Jochum, M., Danabasoglu, G., Holland, M., Kwon, Y.-O., & Large, W. G. (2008).
 1602 Ocean viscosity and climate. *Journal of Geophysical Research*, *113*(C6). doi:
 1603 [10.1029/2007JC004515](https://doi.org/10.1029/2007JC004515)

- 1604 Johns, W. E., Townsend, T. L., Fratantoni, D. M., & Wilson, W. D. (2002). On the
 1605 Atlantic inflow to the Caribbean Sea. *Deep-Sea Research Part I: Oceanographic*
 1606 *Research Papers*, 49(2), 211–243. doi: 10.1016/S0967-0637(01)00041-3
- 1607 Johnson, M., Gaffigan, S., Hunke, E., & Gerdes, R. (2007). A comparison of Arctic
 1608 Ocean sea ice concentration among the coordinated AOMIP model experi-
 1609 ments. *J. Geophys. Res.*, 112(C04S11). doi: 10.1029/2006JC003690
- 1610 Karcher, M., Beszczynska-Möller, A., Kauker, F., Gerdes, R., Heyen, S., Rudels, B.,
 1611 & Schauer, U. (2011). Arctic Ocean warming and its consequences for the
 1612 Denmark Strait overflow. *Journal of Geophysical Research: Oceans*, 116(C2).
 1613 doi: 10.1029/2010JC006265
- 1614 Karcher, M., Smith, J. N., Kauker, F., Gerdes, R., & Jr., W. M. S. (2012). Recent
 1615 changes in Arctic Ocean circulation revealed by iodine-129 observations and
 1616 modeling. *J. Geophys. Res.*, 117(C08007). doi: 10.1029/2011JC007513
- 1617 Kinney, J. C., Maslowski, W., Aksenov, Y., de Cuevas, B., Nguyen, A. T., Osinski,
 1618 R., . . . Zhang, J. (2014). On the flow through Bering Strait: a synthesis of
 1619 model results and observations. In J. Grebmeier & W. Maslowski (Eds.), (pp.
 1620 167–198). Dordrecht: Springer Dordrecht.
- 1621 Kobayashi, S., Ota, Y., Harada, Y., Ebata, A., Moriya, M., Onoda, H., . . . Taka-
 1622 hashi, K. (2015). The JRA-55 Reanalysis: General Specifications and Basic
 1623 Characteristics. *Journal of the Meteorological Society of Japan*, 93(1), 5–48.
- 1624 Köhl, A., & Stammer, D. (2008, 05). Decadal Sea Level Changes in the 50-Year
 1625 GECCO Ocean Synthesis. *Journal of Climate*, 21(9), 1876–1890. doi: 10.1175/
 1626 2007JCLI2081.1
- 1627 Krishfield, R. A. (2020). pers. comm.
- 1628 Krishfield, R. A., Toole, J. M., Proshutinsky, A., & Timmermans, M.-L. (2008).
 1629 Automated ice-tethered profilers for seawater observations under pack
 1630 ice in all seasons. *J. Atmos. Oceanic Technol.*, 25(11), 2091–2105. doi:
 1631 10.1175/2008JTECHO587.1
- 1632 Kwok, R., & Cunningham, G. F. (2008). Icesat over arctic sea ice: Estima-
 1633 tion of snow depth and ice thickness. *J. Geophys. Res.*, 113(C08010).
 1634 (doi:10.1029/2008JC004753)
- 1635 Kwok, R., & Cunningham, G. F. (2015). Variability of Arctic sea ice thickness and
 1636 volume from CryoSat-2. *Phil. Trans. Royal Soc. A*, 373. doi: 10.1098/rsta.2014
 1637 .0157
- 1638 Kwok, R., Cunningham, G. F., Wensnahan, M., Rigor, I., Zwally, H. J., & Yi, D.
 1639 (2009). Thinning and volume loss of the arctic ocean sea ice cover: 2003–2008.
 1640 *J. Geophys. Res.*, 114(C07005). (10.1029/2009JC005312)
- 1641 Kwok, R., & Morison, J. (2016, January). Sea surface height and dynamic topogra-
 1642 phy of the ice-covered oceans from CryoSat-2: 2011–2014. *Journal of Geophysical*
 1643 *Research: Oceans*, 121(1), 674–692.
- 1644 Lammers, R. B., & Shiklomanov, A. I. (2001). Assessment of contemporary Arctic
 1645 river runoff based on observational discharge records. *J. Geophys. Res.*,
 1646 106(D4), 3321.
- 1647 Large, W. G., McWilliams, J., & Doney, S. (1994). Oceanic vertical mixing: A re-
 1648 view and a model with nonlocal boundary layer parameterization. *Rev. Geo-*
 1649 *phys.*, 32, 363–403.
- 1650 Large, W. G., & Yeager, S. G. (2008). The global climatology of an interannually
 1651 varying air–sea flux data set. *Clim. Dyn.*, 33(2–3), 341–364.
- 1652 Lavergne, T., Sørensen, A. M., Kern, S., Tonboe, R., Notz, D., Aaboe, S., . . . Ped-
 1653 ersen, L. T. (2019). Version 2 of the EUMETSAT OSI SAF and ESA CCI
 1654 sea-ice concentration climate data records. *The Cryosphere*, 13(1), 49–78. doi:
 1655 10.5194/tc-13-49-2019
- 1656 Leith, C. E. (1968). Diffusion approximation for two-dimensional turbulence. *Phys.*
 1657 *Fluids*, 10, 1409–1416.
- 1658 Leith, C. E. (1996). Stochastic models of chaotic systems. *Physica D*, 98, 481–491.

- 1659 Levitus, S. (Ed.). (2010). *World ocean atlas 2009*. NOAA Atlas NESDIS 68, U.S.
 1660 Government Printing Office, Washington, D.C.
- 1661 Liang, X., Piecuch, C. G., Ponte, R. M., Forget, G., Wunsch, C., & Heimbach, P.
 1662 (2017). Change of the global ocean vertical heat transport over 1993-2010.
 1663 *Journal of Climate*, *14*(30), 5319–5327. doi: 10.1175/jcli-d-16-0569.1
- 1664 Lind, S., Ingvaldsen, R. B., & Furevik, T. (2018). Arctic warming hotspot in
 1665 the northern Barents Sea linked to declining sea-ice import. *Nature climate*
 1666 *change*, *8*, 634–639. doi: <https://doi.org/10.1038/s41558-018-0205-y>
- 1667 Liu, C., Liang, X., Ponte, R. M., Vinogradova, N., & Wang, O. (2019). Vertical
 1668 redistribution of salt and layered changes in global ocean salinity. *Nat. Com-*
 1669 *munic.*, *10*(3445). doi: 10.1038/s41467-019-11436-x
- 1670 Locarnini, R. A., Mishonov, A. V., Antonov, J. I., Boyer, T. P., Garcia, H. E., Bara-
 1671 nova, O. K., . . . Johnson, D. R. (2010). Volume 1: Temperature. In S. Levitus
 1672 (Ed.), . NOAA Atlas NESDIS 68, U.S. Government Printing Office, Washing-
 1673 ton, D.C.
- 1674 Locarnini, R. A., Mishonov, A. V., Baranova, O. K., Boyer, T. P., Zweng, M. M.,
 1675 Garcia, H. E., . . . Smolyar, I. (2018). Volume 1: Temperature. In A. Mis-
 1676 honov (Ed.), . NOAA Atlas NESDIS 82, U.S. Government Printing Office,
 1677 Washington, D.C.
- 1678 Losch, M., Menemenlis, D., Campin, J.-M., Heimbach, P., & Hill, C. (2010). A
 1679 dynamic-thermodynamic sea ice model for ocean climate modeling on an
 1680 Arakawa C-grid: Part 1: Forward model sensitivities. *omod*, *33*(1-2), 129-144.
 1681 doi: 10.1016/j.ocemod.2009.12.008
- 1682 Lozier, M. S., Bacon, S., Bower, A. S., Cunningham, S. A., Femke de Jong, M., de
 1683 Steur, L., . . . Zika, J. D. (2017). Overturning in the Subpolar North Atlantic
 1684 Program: a new international ocean observing system. *Bull. Amer. Meteor.*
 1685 *Soc.*, *98*(4), 737–752.
- 1686 Lozier, M. S., Li, F., Bacon, S., Bahr, F., Bower, A. S., Cunningham, S. A., . . .
 1687 Zhao, J. (2019). A sea change in our view of overturning in the subpolar North
 1688 Atlantic. *Science*, *363*(6426), 516–521. doi: 10.1126/science.aau6592
- 1689 Lupkes, C., Vihma, T., Jakobson, E., König-Langlo, G., & Tetzlaff, A. (2010). Mete-
 1690 orological observations from ship cruises during summer to the central Arctic:
 1691 A comparison with reanalysis data. *Geophys. Res. Lett.*, *37*(L09810). doi:
 1692 10.1029/2010GL042724
- 1693 Manucharyan, G. E., & Isachsen, P. E. (2019). Critical role of continental slopes in
 1694 halocline and eddy dynamics of the Ekman-driven Beaufort Gyre. *Journal of*
 1695 *Geophysical Research*, *124*, 2679–2696. doi: 10.1029/2018JC014624
- 1696 Manucharyan, G. E., Spall, M. A., & Thompson, A. F. (2016). A theory of the
 1697 wind-driven Beaufort Gyre variability. *Journal of Physical Oceanography*,
 1698 *46*(11), 3263–3278. doi: 10.1175/JPO-D-16-0091.1
- 1699 Marnela, M., Rudels, B., Goszczko, I., Beszczynska-Möller, A., & Schauer, U.
 1700 (2016). Fram Strait and Greenland Sea transports, water masses, and wa-
 1701 ter mass transformations 1999–2010 (and beyond). *Journal of Geophysical*
 1702 *Research*, *121*(4), 2314–2346. doi: 10.1002/2015JC011312
- 1703 Marshall, J., Adcroft, A., Hill, C., Perelman, L., & Heisey, C. (1997). A finite-
 1704 volume, incompressible Navier stokes model for studies of the ocean on parallel
 1705 computers. *J. Geophys. Res.*, *102*, 5753–5766.
- 1706 Martin, T., Steele, M., & Zhang, J. (2014). Seasonality and long-term trend of Arc-
 1707 tic Ocean surface stress in a model. *J. Geophys. Res.*, *119*, 1723–1738. doi: 10
 1708 .1002/2013JC009425
- 1709 Mashayek, A., Ferrari, R., Merrifield, S., Ledwell, J. R., St Laurent, L., & Garabato,
 1710 A. N. (2017). Topographic enhancement of vertical turbulent mixing in the
 1711 Southern Ocean. *Nat. Commun.*, *8*(14197). doi: 10.1038/ncomms14197
- 1712 Mazloff, M. R., Heimbach, P., & Wunsch, C. (2010). An eddy-permitting Southern
 1713 Ocean State Estimate. *Journal of Physical Oceanography*, *40*(5), 880-899. doi:

- 1714 10.1175/2009JPO4236.1
- 1715 Meneghello, G., Marshall, J., Cole, S. T., & Timmermans, M.-L. (2017). Obser-
 1716 vational inferences of lateral eddy diffusivity in the halocline of the Beau-
 1717 fort Gyre. *Geophysical Research Letters*, *44*(24), 12,331–12,338. doi:
 1718 10.1002/2017GL075126
- 1719 Meneghello, G., Marshall, J., Timmermans, M.-L., & Scott, J. (2018, 04). Ob-
 1720 servations of seasonal upwelling and downwelling in the Beaufort Sea me-
 1721 diated by sea ice. *Journal of Physical Oceanography*, *48*(4), 795–805. doi:
 1722 10.1175/JPO-D-17-0188.1
- 1723 Menemenlis, D., Hill, C., Adcroft, A., Campin, J.-M., Cheng, B., Ciotti, B., ...
 1724 Zhang, J. (2005). Towards eddy permitting estimates of the global ocean and
 1725 sea-ice circulation. *EOS Transactions AGU*, *86*(9), 89.
- 1726 Mishonov, A. (Ed.). (2018). *World ocean atlas 2018*. NOAA Atlas NESDIS 82, U.S.
 1727 Government Printing Office, Washington, D.C.
- 1728 Moore, G. W. K., Straneo, F., & Oltmanns, M. (2014). Trend and inter-annual vari-
 1729 ability in southeast Greenland sea ice: Impacts on coastal Greenland climate
 1730 variability. *Geophys. Res. Lett.*, *41*, 8619–8626. doi: 10.1002/2014GL062107
- 1731 Mu, L., Losch, M., Yang, Q., Ricker, R., Losa, S. N., & Nerger, L. (2018). Arctic-
 1732 wide sea ice thickness estimates from combining satellite remote sensing data
 1733 and a dynamic ice-ocean model with data assimilation during the CryoSat-
 1734 2 period. *Journal of Geophysical Research: Oceans*, *123*, 7763–7780. doi:
 1735 10.1029/2018JC014316
- 1736 Muilwijk, M., Smedsrud, L. H., Ilicak, M., & Drange, H. (2018). Atlantic water heat
 1737 transport variability in the 20th century Arctic Ocean from a global ocean
 1738 model and observations. *Journal of Geophysical Research: Oceans*, *123*(11),
 1739 8159–8179.
- 1740 Munk, W. (1966). Abyssal recipes. *Deep Sea Research*, *13*, 707–730.
- 1741 Nguyen, A. T., Heimbach, P., Garg, V. V., Ocaña, V., Lee, C., & Rainville, R.
 1742 (2020). Impact of synthetic Arctic Argo-type floats in a coupled ocean-sea ice
 1743 state estimation framework. *J. Atmos. Ocean. Tech.*, *37*(8), 1477–1495. doi:
 1744 10.1175/JTECH-D-19-0159.1.
- 1745 Nguyen, A. T., Menemenlis, D., & Kwok, R. (2011). Arctic ice-ocean simulations
 1746 with optimized model parameters: approach and assessment. *J. Geophys. Res.*,
 1747 *116*(C4), C04025. doi: 10.1029/2010JC006573
- 1748 Nguyen, A. T., Ocaña, V., Garg, V. V., Heimbach, P., Toole, J. M., Krishfield,
 1749 R. A., ... Rainville, R. (2017). On the benefit of current and future ALPS
 1750 data for improving Arctic coupled ocean-sea ice state estimation. *Oceanogra-*
 1751 *phy*, *30*(2), 69–73. (ALPS II Special Issue) doi: 10.5670/oceanog.2017.223
- 1752 Nguyen, A. T., Woodgate, R. A., & Heimbach, P. (2020). Elucidating large-
 1753 scale atmospheric controls on Bering Strait throughflow variability using a
 1754 data-constrained ocean model and its adjoint. *J. Geophys. Res.*, *125*. doi:
 1755 10.1029/2020JC016213
- 1756 Nurser, A. J. G., & Bacon, S. (2014). The rossby radius in the Arctic Ocean. *Ocean.*
 1757 *Sci.*, *10*, 967–975. Retrieved from www.ocean-sci.net/10/967/2014 doi: 10
 1758 .5194/os-10-967-2014
- 1759 Østerhus, S., Woodgate, R. A., Valdimarsson, H., Turrell, B., de Steur, L., Quad-
 1760 fassel, D., ... Berx, B. (2019). Arctic Mediterranean exchanges: a consistent
 1761 volume budget and trends in transports from two decades of observations.
 1762 *Ocean. Sci.*, *15*, 379–399. doi: <https://doi.org/10.5194/os-15-379-2019>
- 1763 Padman, L., & Dillon, T. M. (1988). On the horizontal extent of thermohaline steps
 1764 in the Canada Basin. *J. Phys. Oceanogr.*, *18*, 1458–1462.
- 1765 Peralta-Ferriz, C., Morison, J. H., Wallace, J. M., Bonin, J. A., & Zhang, J. (2014).
 1766 Arctic Ocean circulation patterns revealed by GRACE. *J. Climate*, *27*(4),
 1767 1445–1468. doi: 10.1175/JCLI-D-13-00013.1
- 1768 Perovich, D. K., Richter-Menge, J., Jones, K., Light, B., Elder, B. C., Polashenski,

- 1769 C., ... Lindsay, R. (2011). Arctic sea-ice melt in 2008 and the role of solar
1770 heating. *Annals of Glaciology*, *52*(57), 355–359.
- 1771 Piecuch, C. G. (2017). *A note on practical evaluation of budgets in ecco version*
1772 *4 release 3* (Tech. Rep.). Retrieved from [http://hdl.handle.net/1721.1/](http://hdl.handle.net/1721.1/111094)
1773 [111094](http://hdl.handle.net/1721.1/111094)
- 1774 Piecuch, C. G., & Ponte, R. M. (2012). Importance of circulation changes to At-
1775 lantic heat storage rates on seasonal and interannual time scales. *J. Climate*,
1776 *25*(1), 350–362. doi: 10.1175/JCLI-D-11-00123.1
- 1777 Piecuch, C. G., & Ponte, R. M. (2013). Mechanisms of global-mean steric sea level
1778 change. *Journal of Climate*, *27*, 824–834. doi: 10.1175/JCLI-D-13-00373.1
- 1779 Piecuch, C. G., Ponte, R. M., Little, C. M., Buckley, M. W., & Fukumori, I.
1780 (2017). Mechanisms underlying recent decadal changes in subpolar North
1781 Atlantic ocean heat content. *J. Geophys. Res.*, *122*, 7181–7197. doi:
1782 [10.1002/2017JC012845](https://doi.org/10.1002/2017JC012845)
- 1783 Pillar, H. R., Heimbach, P., Johnson, H. L., & Marshall, D. P. (2016). Dynamical at-
1784 tribution of recent variability in Atlantic overturning. *J. Clim.*, *29*, 3339–3352.
1785 doi: 10.1175/JCLI-D-15-0727.1
- 1786 Pnyushkov, A. V., Polyakov, I. V., Ivanov, V. V., Aksenov, Y., Coward, A. C.,
1787 Janout, M., & Rabe, B. (2015). Structure and variability of the boundary
1788 current in the Eurasian Basin of the Arctic Ocean. *Deep Sea Research Part I:*
1789 *Oceanographic Research Papers*, *101*, 80–97. doi: 10.1016/j.dsr.2015.03.001
- 1790 Pnyushkov, A. V., Polyakov, I. V., Ivanov, V. V., & Kikuchi, T. (2013). Structure of
1791 the Fram Strait branch of the boundary current in the Eurasian Basin in the
1792 Arctic Ocean. *Polar Science*, *7*(2). (10.1016/j.polar.2013.02.001)
- 1793 Pnyushkov, A. V., Polyakov, I. V., Padman, L., & Nguyen, A. T. (2018). Structure
1794 and dynamics of mesoscale eddies over the Laptev Sea continental slope in
1795 the Arctic Ocean. *Ocean Sci.*, *14*, 1329–1347. doi: [https://doi.org/10.5194/](https://doi.org/10.5194/os-14-1329-2018)
1796 [os-14-1329-2018](https://doi.org/10.5194/os-14-1329-2018)
- 1797 Polyakov, I. V., Alexeev, V. A., Ashik, I. M., Bacon, S., Beszczynska-Möller, A.,
1798 Carmack, E. C., ... Woodgate, R. A. (2011). Fate of early 2000s Arct-
1799 ic warm water pulse. *Bull. Amer. Meteor. Soc.*, *92*(5), 561–566. doi:
1800 [10.1175/2010BAMS2921.1](https://doi.org/10.1175/2010BAMS2921.1)
- 1801 Polyakov, I. V., Pnyushkov, A. V., Alkire, M. B., Ashik, I. M., Baumann, T. M.,
1802 Carmack, E. C., ... Yulin, A. (2017). Greater role for Atlantic inflows on
1803 sea-ice loss in the Eurasian Basin of the Arctic Ocean. *Science*, *356*, 285–291.
1804 doi: 10.1126/science.aai8204
- 1805 Polyakov, I. V., Pnyushkov, A. V., & Timokhov, L. A. (2012). Warming of the in-
1806 termediate atlantic water of the arctic ocean in the 2000s. *J. Climate*, *25*(23),
1807 8362–8370. doi: 10.1175/JCLI-D-12-00266.1
- 1808 Polyakov, I. V., Rippeth, T. P., Fer, I., Alkire, M. B., Baumann, T. M., Carmack,
1809 E. C., ... Rember, R. (2020). Weakening of cold halocline layer exposes sea
1810 ice to oceanic heat in the eastern Arctic Ocean. *Journal of Climate*. (in press)
1811 doi: 10.1175/JCLI-D-19-0976.1
- 1812 Pradal, M.-A., & Gnanadesikan, A. (2014). How does the Redi parameter for
1813 mesoscale mixing impact global climate in an Earth System Model? *J. Adv.*
1814 *Model. Earth Syst.*, *6*, 586–601. doi: 10.1002/2013MS000273
- 1815 Project Jupyter, Matthias Bussonnier, Jessica Forde, Jeremy Freeman, Brian
1816 Granger, Tim Head, ... Carol Willing (2018). Binder 2.0 - Reproducible,
1817 interactive, sharable environments for science at scale. In Fatih Akici, David
1818 Lippa, Dillon Niederhut, & M. Pacer (Eds.), *Proceedings of the 17th Python in*
1819 *Science Conference* (p. 113 - 120). doi: 10.25080/Majora-4af1f417-011
- 1820 Proshutinsky, A., Krishfield, R. A., & Timmermans, M. L. (2020). Introduction
1821 to special collection on Arctic Ocean modeling and observational synthe-
1822 sis (FAMOS) 2: Beaufort Gyre phenomenon. *J. Geophys. Res.*, *125*. doi:
1823 <https://doi.org/10.1029/2019JC015400>

- 1824 Proshutinsky, A., Krishfield, R. A., Timmermans, M.-L., Toole, J. M., Carmack, E.,
1825 McLaughlin, F., . . . Shimada, K. (2009). Beaufort Gyre freshwater reservoir:
1826 State and variability from observations. *J. Geophys. Res.*, *114*(C1), C00A10.
1827 doi: 10.1029/2008JC005104
- 1828 Proshutinsky, A., Krishfield, R. A., Toole, J. M., Timmermans, M.-L., Williams,
1829 W., Zimmermann, S., . . . Zhao, J. (2019). Analysis of the Beaufort Gyre
1830 freshwater content in 2003–2018. *J. Geophys. Res.*, *124*, 9658–9689. doi:
1831 <https://doi.org/10.1029/2019JC015281>
- 1832 Rabe, B., Karcher, M., Kauker, F., Schauer, U., Toole, J. M., Krishfield, R. A., . . .
1833 Su, J. (2014). Arctic Ocean basin liquid freshwater storage trend 1992–2012.
1834 *Geophys. Res. Lett.*, *41*, 961–968. doi: 10.1002/2013GL058121
- 1835 Rainville, L., & Woodgate, R. A. (2009). Observations of internal wave generation in
1836 the seasonally ice-free Arctic. *Geophys. Res. Lett.*, *36*(23), L23604.
- 1837 Redi, M. H. (1982). Oceanic isopycnal mixing by coordinate rotation. *J. Phys.*
1838 *Oceanogr.*, *12*, 1154–1158.
- 1839 Richter-Menge, J., & Jeffries, M. (2011). The Arctic. *Bulletin American Meteorolog-*
1840 *ical Society*, *92*, S143–S160.
- 1841 Ricker, R., Tian-Kunze, S. H. L. K. X., King, J., & Haas, C. (2017). A weekly Arc-
1842 tic sea-ice thickness data record from merged CryoSat-2 and SMOS satellite
1843 data. *The Cryosphere*, *11*, 1607–1623. doi: 10.5194/tc-11-1607-2017
- 1844 Rossby, T., Flagg, C., Chafik, L., Harden, B., & Søiland, H. (2018). A direct
1845 estimate of volume, heat, and freshwater exchange across the Greenland-
1846 Iceland-Faroe-Scotland ridge. *J. Geophys. Res.*, *123*, 7139–7153. doi:
1847 <https://doi.org/10.1029/2018JC014250>
- 1848 Rudels, B. (2012). Arctic ocean circulation and variability - advection and external
1849 forcing encounter constraints and local processes. *Ocean Science*, *8*(2), 261–
1850 286. doi: 10.5194/os-8-261-2012
- 1851 Rudels, B. (2015). Arctic Ocean circulation, processes and water masses: A de-
1852 scription of observations and ideas with focus on the period prior to the Inter-
1853 national Polar Year 2007–2009. *Progress in Oceanography*, *132*, 22–67. doi:
1854 10.1016/j.pocean.2013.11.006
- 1855 Schauer, U., & Beszczynska-Möller, A. (2009). Problems with estimation and
1856 interpretation of oceanic heat transport—conceptual remarks for the case
1857 of Fram Strait in the Arctic Ocean. *Ocean Science*, *5*, 487–494. doi:
1858 <https://doi.org/10.5194/os-5-487-2009>
- 1859 Schauer, U., & Fahrback, E. (2004). Arctic warming through the Fram Strait:
1860 Oceanic heat transport from 3 years of measurements. *J. Geophys. Res.*,
1861 *109*(C06026). doi: 10.1029/2003JC001823
- 1862 Schauer, U., & Losch, M. (2019). “freshwater” in the ocean is not a useful parameter
1863 in climate research. *Journal of Physical Oceanography*, *49*(9), 2309–2321. doi:
1864 10.1175/JPO-D-19-0102.1
- 1865 Sciascia, R., Straneo, F., Cenedese, C., & Heimbach, P. (2013). Seasonal variability
1866 of submarine melt rate and circulation in an East Greenland fjord. *Journal of*
1867 *Geophysical Research*, *118*, 2492–2506. doi: 10.1002/jgrc.20142
- 1868 Shiklomanov, A., Déry, S., Tretiakov, M., Yang, D., Magritsky, D., Georgiadi, A.,
1869 & Tang, W. (2020, August). River Freshwater Flux to the Arctic Ocean. In
1870 *Arctic hydrology, permafrost and ecosystems* (pp. 703–738). Cham: Springer
1871 International Publishing.
- 1872 Shiklomanov, A. I., Yakovleva, T. I., Lammers, R. B., Karasev, I. P., Vörösmarty,
1873 C. J., & Linder, E. (2006). Cold region river discharge uncertainty—estimates
1874 from large Russian rivers. *Journal of Hydrology*, *326*(1-4), 231–256.
- 1875 Sirevaag, A., & Fer, I. (2012). Vertical heat transfer in the Arctic Ocean: the role
1876 of double-diffusive mixing. *J. Geophys. Res.*, *117*(C07010). doi: doi:10.1029/
1877 2012JC007910
- 1878 Skagseth, O., Furevik, T., Ingvaldsen, R., Loeng, H., Mork, K. A., Orvik, K. A.,

- 1879 & Ozhigin, V. (2008). Chapter: Volume and heat transports to the Arctic
 1880 Ocean via the Norwegian and Barents Seas. In R. R. Dickson, J. Meincke,
 1881 & P. Rhines (Eds.), *Arctic-subarctic ocean fluxes* (pp. 45–64). Netherlands:
 1882 Springer. doi: https://doi.org/10.1007/978-1-4020-6774-7_3
- 1883 Smedsrud, L. H., Ingvaldsen, R., Nilsen, J. E. O., & Skagseth, O. (2010). Heat in
 1884 the Barents Sea: Transport, storage and surface fluxes. *Ocean Sci.*, *6*(1), 219–
 1885 234. doi: <https://doi.org/10.5194/os-6-219-2010>
- 1886 Smith, T. (2020, October). *crios-ut/aste: Aste release 1*. Zenodo. Retrieved from
 1887 <https://doi.org/10.5281/zenodo.4132216> doi: 10.5281/zenodo.4132216
- 1888 Smith, W. H. F., & Sandwell, D. T. (1997). Global sea floor topography from satel-
 1889 lite altimetry and ship depth soundings. *Science*, *277*(5334), 1956–1962.
- 1890 Spall, M. A. (2020, 08). Potential vorticity dynamics of the Arctic halocline. *Journal*
 1891 *of Physical Oceanography*, *50*(9), 2491–2506. doi: 10.1175/JPO-D-20-0056.1
- 1892 Spreen, G., Kern, S., Stammer, D., & Hansen, E. (2009). Fram Strait sea ice volume
 1893 export estimated between 2003 and 2008 from satellite data. *Geophys. Res.*
 1894 *Lett.*, *36*(L19502). doi: 10.1029/2009GL039591
- 1895 Stammer, D., Balmaseda, M., Heimbach, P., Köhl, A., & Weaver, A. (2016). Ocean
 1896 data assimilation in support of climate applications: Status and perspectives.
 1897 *Annu. Rev. Mar. Sci.*, *8*(accepted). doi: 10.1146/annurev-marine-122414
 1898 -034113
- 1899 Stammer, D., Wunsch, C., Giering, R., Eckert, C., Heimbach, P., Marotzke, J., ...
 1900 Marshall, J. (2002). Global ocean circulation during 1992–1997, estimated
 1901 from ocean observations and a general circulation model. *Journal of Geophysic-*
 1902 *al Research*, *107*(C9), 3118–1–27.
- 1903 Steele, M., Morley, R., & Ermold, W. (2001). PHC: A global ocean hydrography
 1904 with a high-quality arctic ocean. *J. Clim.*, *14*, 2079–2087.
- 1905 Straneo, F., & Cenedese, C. (2015). The dynamics of Greenland’s glacial fjords and
 1906 their role in climate. *Annu. Rev. Mar. Sci.*, *7*, 89–112. doi: 10.1146/annurev
 1907 -marine-010213-135133
- 1908 Tesdal, J.-E., & Haine, T. W. N. (2020). Dominant terms in the freshwater and
 1909 heat budgets of the subpolar North Atlantic Ocean and Nordic Seas from
 1910 1992 to 2015. *J. Geophys. Res.*. (submitted) doi: [https://doi.org/10.1002/](https://doi.org/10.1002/essoar.10503232.1)
 1911 [essoar.10503232.1](https://doi.org/10.1002/essoar.10503232.1)
- 1912 Tian-Kunze, X., Kaleschke, L., Maass, N., Maekynen, M., Serra, N., Drusch, M., &
 1913 Krumpfen, T. (2014). SMOS-derived sea ice thickness: algorithm baseline,
 1914 product specifications and initial verification. *The Cryosphere*, *8*, 997–1018.
 1915 (doi:10.5194/tc-8-997-2014)
- 1916 Timmermans, M.-L., Cole, S., & Toole, J. M. (2012). Horizontal density struc-
 1917 ture and restratification of the Arctic Ocean surface layer. *J. Phys. Oceanogr.*,
 1918 *42*(4), 659–668. doi: 10.1175/JPO-D-11-0125.1
- 1919 Timmermans, M.-L., & Jayne, S. R. (2016). The Arctic Ocean spices up. *Journal of*
 1920 *Physical Oceanography*, *46*, 1277–1284. doi: 10.1175/JPO-D-16-0027.1
- 1921 Timmermans, M.-L., & Marshall, J. (2020). Understanding Arctic Ocean circulation:
 1922 A review of ocean dynamics in a changing climate. *Journal of Geophysical Re-*
 1923 *search*, *125*(4), e2018JC014378. doi: 10.1029/2018JC014378
- 1924 Timmermans, M.-L., Toole, J. M., & Krishfield, R. A. (2018). Warming of the in-
 1925 terior Arctic Ocean linked to sea ice losses at the basin margins. *Science Ad-*
 1926 *vances*, *4*(8). doi: 10.1126/sciadv.aat6773
- 1927 Toole, J. M. (2007). Temporal characteristics of abyssal finescale motions above
 1928 rough bathymetry. *Journal of Physical Oceanography*, *37*(3), 409–427. Re-
 1929 trieved from <https://doi.org/10.1175/JPO2988.1> doi: 10.1175/JPO2988
 1930 .1
- 1931 Toole, J. M., Krishfield, R. A., & Timmermans, M.-L. (2011). The ice-tethered pro-
 1932 filer: Argo of the Arctic. *Oceanography*, *24*(3), 126–135. doi: 10.5670/oceanog
 1933 .2011.64

- 1934 Treguier, A. M., Deshayes, J., Le Sommer, J., Lique, C., Madec, G., Penduff,
1935 T., ... Talandier, C. (2014). Meridional transport of salt in the global
1936 ocean from an eddy-resolving model. *Ocean Science*, *10*(2), 243–255. doi:
1937 10.5194/os-10-243-2014
- 1938 Tsubouchi, T., Bacon, S., Aksenov, Y., Garabato, A. C. N., Beszczynska-Möller, A.,
1939 Hansen, E., ... Lee, C. M. (2018). The Arctic Ocean seasonal cycles of heat
1940 and freshwater fluxes: Observation-based inverse estimates. *Journal of Physical
1941 Oceanography*, *48*(9), 2029–2055. doi: 10.1175/JPO-D-17-0239.1
- 1942 Tsujino, H., Urakawa, S., Nakano, H., Small, R. J., Kim, W. M., Yeager, S. G.,
1943 ... Yamazaki, D. (2018). JRA-55 based surface dataset for driving
1944 ocean–sea-ice models (JRA55-do). *Ocean Modelling*, *130*, 79–139. doi:
1945 <https://doi.org/10.1016/j.ocemod.2018.07.002>
- 1946 Uotila, P., Goosse, H., Haines, K., Chevallier, M., Barthélemy, A., Bricaud, C., ...
1947 Zhang, Z. (2019). An assessment of ten ocean reanalyses in the polar regions.
1948 *Clim Dyn*, *52*, 1613–1650. doi: 10.1007/s00382-018-4242-z
- 1949 Verdy, A., Cornuelle, B., Mazloff, M. R., & Rudnick, D. L. (2017). Estimation of the
1950 tropical Pacific Ocean state 2010–13. *J. Atm. Oceanic Tech.*, *34*, 1501–1517.
1951 doi: 10.1175/JTECH-D-16-0223.1
- 1952 Vinogradova, N. T., & Ponte, R. M. (2012). Assessing temporal aliasing in satellite-
1953 based salinity measurements. *J. Atmos. Ocean. Technol.*, *29*(9), 1391–1400.
1954 doi: 10.1175/JTECH-D-11-00055.1
- 1955 von Appen, W.-J., Schauer, U., Hattermann, T., & Beszczynska-Möller, A. (2015).
1956 Seasonal cycle of mesoscale instability of the West Spitsbergen Current. *Jour-
1957 nal of Physical Oceanography*, 1231–1254. doi: doi:10.1175/jpo-d-15-0184.1
- 1958 von Appen, W.-J., Schauer, U., Somavilla Cabrillo, R., Bauerfeind, E., &
1959 Beszczynska-Möller, A. (2015). Exchange of warming deep waters across
1960 Fram Strait. *Deep Sea Res.*, 86–100. doi: doi:10.1016/j.dsr.2015.06.003
- 1961 Våge, K., Moore, G. W. K., Jónsson, S., & Valdimarsson, H. (2015). Water
1962 mass transformation in the Iceland Sea. *Deep Sea Res. Part I*, *101*, 98–109.
1963 (doi:10.1016/j.dsr.2015.04.001)
- 1964 Wadhams, P., Comiso, J. C., Prussen, E., Wells, S., Brandon, M., Aldworth, E., ...
1965 Crane, D. R. (1996). The development of the Oden ice tongue in the Green-
1966 land Sea during winter 1993 from remote sensing and field observations. *J.
1967 Geophys. Res.*, *101*(C8), 18213–18235.
- 1968 Wang, C., Graham, R. M., Wang, K., Gerland, S., & Granskog, M. A. (2019).
1969 Comparison of ERA5 and ERA-Interim near-surface air temperature, snowfall
1970 and precipitation over Arctic sea ice: effects on sea ice thermodynamics and
1971 evolution. *The Cryosphere*, *13*(6), 1661–1679. doi: 10.5194/tc-13-1661-2019
- 1972 Wang, Q., Ilicak, M., Gerdes, R., Drange, H., Aksenov, Y., Bailey, D. A., ... Yeager,
1973 S. G. (2016a). An assessment of the Arctic Ocean in a suite of interannual
1974 CORE-II simulations. part ii: Liquid freshwater. *Ocean Modelling*, *99*, 86–109.
1975 Retrieved from [http://www.sciencedirect.com/science/article/pii/
1976 S1463500315002450](http://www.sciencedirect.com/science/article/pii/S1463500315002450) doi: <https://doi.org/10.1016/j.ocemod.2015.12.009>
- 1977 Wang, Q., Ilicak, M., Gerdes, R., Drange, H., Aksenov, Y., Bailey, D. A., ... Yeager,
1978 S. G. (2016b). An assessment of the Arctic Ocean in a suite of interannual
1979 CORE-II simulations. part i: Sea ice and solid freshwater. *Ocean Modelling*,
1980 *99*, 110–132. doi: <https://doi.org/10.1016/j.ocemod.2015.12.008>
- 1981 Wang, Q., Wekerle, C., Wang, X., Danilov, S., Koldunov, N., Sein, D., ... Jung,
1982 T. (2020). Intensification of the Atlantic Water supply to the Arctic Ocean
1983 through Fram Strait induced by Arctic sea ice decline. *Geophysical Research
1984 Letters*, *47*(3). doi: 10.1029/2019GL086682
- 1985 Weijer, W., Maltrud, M. E., Hecht, M. W., Dijkstra, H. A., & Kliphuis, M. A.
1986 (2012). Response of the Atlantic Ocean circulation to Greenland Ice Sheet
1987 melting in a strongly-eddying ocean model. *Geophys. Res. Lett.*, *39*(L09606).
1988 doi: 10.1029/2012GL051611

- 1989 Wolfe, C. L., Hameed, S., & Chi, L. (2019). On the drivers of decadal variability of
1990 the Gulf Stream North Wall. *J. Climate*, *32*, 1235–1249. doi: 10.1175/JCLI-D
1991 -18-0212.1
- 1992 Woodgate, R. A. (2018). Increases in the Pacific inflow to the Arctic from 1990
1993 to 2015, and insights into seasonal trends and driving mechanisms from year-
1994 round Bering Strait mooring data. *Progress in Oceanography*, *160*, 124–154.
1995 doi: <https://doi.org/10.1016/j.pocean.2017.12.007>
- 1996 Woodgate, R. A., Stafford, K. J., & Prahl, F. G. (2015). A synthesis of year-round
1997 interdisciplinary mooring measurements in the Bering Strait (1990–2014)
1998 and the RUSALCA years (2004–2011). *Oceanography*, *28*(3), 46–67. doi:
1999 10.5670/oceanog.2015.57
- 2000 Wunsch, C., & Heimbach, P. (2007). Practical global oceanic state estimation. *Phys-*
2001 *ica D: Nonlinear Phenomena*, *230*(1-2), 197–208. doi: 10.1016/j.physd.2006.09
2002 .040
- 2003 Wunsch, C., & Heimbach, P. (2013). Dynamically and Kinematically Consistent
2004 Global Ocean Circulation and Ice State Estimates. In *Ocean circulation and*
2005 *climate: A 21st century perspective* (pp. 553–579). Elsevier Ltd. doi: 10.1016/
2006 B978-0-12-391851-2.00021-0
- 2007 Yang, J. (2005). The Arctic and subarctic ocean flux of potential vorticity and the
2008 Arctic Ocean circulation. *J. Phys. Oceanogr.*, *35*, 2387–2407.
- 2009 Zaba, K. D., Rudnick, D. L., Cornuelle, B. D., Gopalakrishnan, G., & Mazloff, M. R.
2010 (2018). Annual and interannual variability in the California Current System:
2011 comparison of an ocean state estimate with a network of underwater gliders. *J.*
2012 *Phys. Oceanogr.*, *48*, 2965–2988. doi: 10.1175/JPO-D-18-0037.1
- 2013 Zhang, J., & Rothrock, D. A. (2003). Modeling global sea ice with a thickness
2014 and enthalpy distribution model in generalized curvilinear coordinates. *Mon.*
2015 *Weather Rev.*, *131*, 845–861.
- 2016 Zhang, J., & Steele, M. (2007). Effect of vertical mixing on the atlantic wa-
2017 ter layer circulation in the arctic ocean. *J. Geophys. Res.*, *112*(C04S04),
2018 doi:10.1029/2006JC003732.
- 2019 Zhao, M., Timmermans, M.-L., Cole, S., Krishfield, R. A., & Toole, J. M. (2016).
2020 Evolution of the eddy field in the Arctic Ocean’s Canada Basin, 2005–2015.
2021 *Geophys. Res. Lett.*, *43*, 8106–8114. doi: 10.1002/2016GL069671
- 2022 Zweng, M. M., Reagan, J. R., Seidov, D., Boyer, T. P., Locarnini, R. A., Garcia,
2023 H. E., ... Smolyar, I. (2018). Volume 2: Salinity. In A. Mishonov (Ed.), .
2024 NOAA Atlas NESDIS 82, U.S. Government Printing Office, Washington, D.C.